NASA Contractor Report 189587

JIN 02

81279

P- 216

A STUDY OF VISCOUS INTERACTION
EFFECTS ON HYPERSONIC WAVERIDERS

Jinhwa Chang

UNIVERSITY OF MARYLAND
College Park, Maryland

NASA

ABSTRACT

Title of Dissertation : A Study of Viscous Interaction Effects
on Hypersonic Waveriders

Jinhwa Chang, Doctor of Philosophy, 1991

Dissertation directed by: Dr. John D. Anderson, Jr.
Professor
Department of Aerospace Engineering

In a continuing effort to generate new and improved classes of viscous optimized hypersonic waveriders, the present work takes a step forward and examines the effects of viscous interaction in the waverider design and analysis process. Parametric runs are made to produce L/D, C_L, and C_D contour plots for Mach number 6.0 to 30.0 at an altitude 30.0 to 80.0 Km, for waverider designer's reference. This is the first work to examine the effects of viscous interactions on hypersonic waveriders, and to generate a new family of waveriders wherein viscous interaction effects are included within the optimization process.

Corda's computer program is used to generate viscous optimized hypersonic waveriders from conical flowfields without viscous interaction. Each waverider is optimized for maximum L/D , and comparison studies are made between the cases with and without viscous interaction. Other results of the investigation agreed with viscous interaction theory in showing an increase in the surface pressure near the leading edge of a waverider, and also the tendency for it to approach the freestream value further downstream. This change in the surface pressure distribution as well as increases in the skin friction, resulted a decrease in the maximum Lift/Drag for the waverider. The influence of viscous interactions on the surface pressure distribution and hence the maximum L/D were

found to result in noticeably different viscous optimized waveriders generated without considering viscous interactions.

Finally, the results show that aerodynamic performance of the viscous interaction waveriders are greatly reduced due mainly to a large increase in skin-friction drag associated with the viscous interaction phenomena that is increased with increasing the Mach number and altitude, but some of this loss can be recouped by including viscous interactions within the optimization procedure. When the waverider is optimized for viscous interaction, the shape can change dramatically.

The central conclusion of the present work delineates on a velocity–altitude map that region where viscous interaction effects are significant for modern hypersonic waveriders. In particular, viscous interaction effects become important at Mach numbers greater than sixteen and altitudes upwards of 140,000 feet.

Acknowledgement

Finally, I dedicate this dissertation to my family members, especially to my wife, Hea Sung and lovely two children, Soona, and Sunghwan who have been a source of inspiration to me. And also thanks to my Christian friends who prayed for me.

Contents

List of Tables

List of Figures

Nomenclature

a	Speed of sound
A	Area
b	Span of a waverider
C	Rho–mu ratio
$\overline{C}$	Centroid of simplex
C_f	Skin friction coefficient
C_D	Drag coefficient
C_L	Lift coefficient
C_M	Moment coefficient
C_p	Pressure coefficient
D	Drag force
e	Internal energy
F	Force or object function
h	Static enthalpy
l	Length
L	Lift force
L/D	Lift over drag ratio
m	Meters
$\dot{m}$	Mass flow rate
M	Mach number
N	Number of Panels

P	Pressure
P	Nondimensional pressure
P_r	Prandtl number
q	Dynamic pressure
r	Radial distance in spherical coordinates
r_b	Base radius
r_{sh}	Conical shock radius at end of cone
R	Specific gas constant for air
Re_x	Reynolds number based on x
s	semi-span length
S_{paln}	Planform area
S_{wet}	Total wetted surface area
T	Static temperature
V	Volume or total velocity
V_{eff}	Volumetric efficiency
w	Velocity component in z–direction
X	Vector of variables for vertex of simplex

Greek Symbols

α	Reflection coefficient
β	Contraction coefficient
γ	Ratio of specific heats or expansion coefficient

δ	Boundary layer thickness
δ^*	Displacment thickness
θ	Polar angle in spherical coordinate or angle of inclination of body
θ_c	Cone semi-apex angle
θ_{xz}	Angle in the (x–z) plane
θ_{yh}	Angle between an arbitrary vector and the (x–z) plane
Λ	Heat transfer function
μ	Coefficient of viscosity
ξ	Streched variable
ρ	Density
τ	Shear stress
ϕ	Azimuth angle in spherical coordinates
Ψ	Stream function

Subscripts

avg	Average value
aw	Adiabatic wall
$base$	Value at base
c	Panel centroid or contracted value
e	Edge condition

f	Due to skin-friction
i	Panel index
l	Lower
p	Due to pressure
r	Radial direction
sh	Shock
u	Upper
w	Condition at wall
θ	In direction of polar angle
o	Stagnation condition
∞	Free stream condition

Superscript

i	Trial value of shock wave angle

Chapter 1

Introduction

1.1 Viscous Interaction: What is it?

In recent years concepts such as the National Aero-Space Plane (NASP) and the German Sanger project have led to a renewed interest in the design of efficient hypersonic configurations. With the recent resurgence of interest in NASP, space shuttles, hypersonic missiles, and orbital transfer vehicles, waverider configurations are being proposed as effective hypersonic designs [1]. One of the most significant challenges facing the designer of a hypersonic vehicle is an accurate prediction of skin friction and heat transfer; these are viscous effects, caused by the dissipation of kinetic energy within the boundary layer. Viscous effects will be critical for the accurate assessment of the aerodynamic performance of hypersonic vehicles. Hypersonic waveriders, at high altitude, will fly at a high Mach number and a low Reynolds number; these conditions accentuate the effects of hypersonic viscous flow. In fact, under these conditions, viscous effects can dominate the flow field and drastically alter the pressure distribution on the waverider – this is called *hypersonic viscous interaction.*

Stollery [2] defines viscous interaction "as the mutual interaction between

the external flow field and the boundary layer growth around a body of a given shape." In the literature, several types of viscous interactions are addressed. Each is a consequence of the so-called "mutual interaction" — a highly viscous boundary layer changes the character of the outer inviscid flow, which in turn changes the structure of the boundary layer. Cox and Crabtree [3] uses the term "second order boundary layer effects" when describing viscous interaction; these are the effects neglected in classical boundary layer theory, used typically to analyze high Reynolds number flows.

The first viscous interaction, and the one germane to this research, is the so-called "pressure interaction" due to the presence of exceptionally thick boundary layers under certain hypersonic conditions. As pointed out in Ref. [4] , pressure interaction is frequently referred to as simply "viscous interaction" in today's literature. Compared to vorticity interaction, pressure interaction is generally "by far the most important" [5].

Talbot et al., [6] uses the term "viscous self-induced-pressure effect". He explains the phenomenon as follows (refer to Figure C.1, from Ref. [4]):

"At hypersonic speeds the boundary layers which develop on bodies are, because of the large temperature differences generated through them, many times thicker than those which are produced at low speeds. Since the density of the hot gas in a hypersonic boundary layer is very low, the mass flux within the boundary layer is small. Thus, the presence of a thick layer of hot gas adjacent to the surface of a body results in the

2

outward displacement of streamlines in the flow external to the layer; this outward displacement can be regarded as equivalent to an effective thickening of the body. It can easily be seen that this thickening will result in increases in pressure in the flow external to the boundary layer, and because the pressure in the external flow is transmitted essentially without change through the boundary layer, the pressures on the surface of the body will likewise be increased. The difference between the actual surface pressure and that calculated by inviscid theory neglecting self-induced pressure."

As stated above, a hypersonic boundary layer can be "many times thicker than those which are produced at low speeds." – "10-15 times thicker" according to a report by Lees [7] in 1956. The major consequence of this phenomenon is the "self-induced-pressure effect". Anderson uses the term "induced pressure change". The first mention of this in the literature was by Becker [8]. He was quick to make the following observation: "Two obvious practical effects of this phenomenon are to increase the pressure drag of hypersonic airfoils and to alter appreciably the characteristics of leading-edge control devices." Additionally, due to "displacement effects", Truitt [9] found the skin friction coefficient (hence drag) to be "several times greater" than that predicted by conventional boundary layer theory without including displacement effects. Bertram [10] confirmed this experimentally for hypersonic flow over a flat plate; Bertram found a 20 - 40% increase (above classical laminar skin friction results) in skin friction drag caused by "boundary layer induced pressure". Anderson [4] provide the following

3

physical argument to explain the above consequence of viscous interaction:

"The increased pressure (hence increased density) tends to make the boundary layer thinner than would be expected (although δ is still large on a relative scale), and hence the velocity and temperature gradients at the wall are increased. In turn, the skin friction and heat transfer is increased over their values that would exist if a constant pressure equal to P_∞ were assumed".

The second interaction effect([2], [3], and [4]) is the shock wave/boundary layer interaction; this refers to the interaction occurring when a shock wave impinges upon a boundary layer (refer to Figure C.2, from Ref. [4]). Because pressure increases across a shock wave, a region of adverse pressure gradient can be established in the vicinity of this interaction. A severe gradient can result in "pockets" of locally separated flow within the boundary layer. Additionally, secondary shocks can be formed as the flow field seeks to establish itself in some form of "equilibrium". Between the separation shock wave and reattachment shock, the curvature of the boundary layer turning back to the surface of the plate will create expansion waves. The pressure will increase and the boundary layer will become quite thin at the reattachment point. The net effect, of this rather complicated picture, can be regions of extremely high aerodynamic heating and heat transfer.

The third type of interaction associated with large boundary layer thicknesses occurs when the vorticity in the external inviscid flow is sufficiently large

4

that the boundary layer structure is affected not only by the external velocity distribution but also by the inviscid vorticity distribution. For sharp-nosed slender bodies, vorticity interaction results from the effective blunting of the nose due to the initial boundary layer growth [5]. In 1937, Crocco [11] used his theorem to show that entropy gradients, behind a curved shock wave, resulted in a rotational flow field. Vorticity interaction may be especially important in the boundary layer for the case of blunted slender bodies or blunt bodies at very low Reynolds numbers [5]. In the early analyses of viscous interactions (see, for example, Ref. [12]), using primarily "self-similar" and "matching" techniques, these regions of entropy gradients/rotational flows presented major difficulties in developing theories to adequately predict flow field structure.

For completeness, Cox and Crabtree [3] also classifies "body curvature" and "slip effects" as secondary interaction effects. Both influence boundary layer growth and hence interact with the external flow field.

The reader is reminded again that only the "pressure interaction" type of viscous interaction is considered in the present research.

1.2 A Brief Review of Waveriders

Over the 30 years since the waverider concept was first formulated by Nonweiler in 1959 [13], this concept has received sporadic attention, with majority of the research carried out in Europe. A waverider utilizes a known supersonic or hypersonic flow field to define the compression lifting surface with an attached leading edge shock. Since the shock wave is attached to the leading edge at the design Mach number and angle of attack, the wing appears to ride on its shock wave; therefore, it is called a "waverider". Lifting efficiency of the compression surface is obtained because there is no flow spillage from the lower surface to the upper surface.

Most early waverider concepts(1959-1968) were derived from two-dimensional planar flow fields. An excellent and authoritative survey of waverider research has been given by Townend [14] and a tutorial approach is also taken by Roe [15]. The basic design methodology was explained in detail by Townend [16] and is illustrated in Figure C.3. The intersection of an arbitrary capture flow tube surface with a two-dimensional oblique shock defines the leading edge of the waverider. The lower surface is defined by tracing the flow field streamlines from the leading edge to the desired base location of the waverider. The upper surface is defined by tracing streamlines parallel to the freestream flow from the leading edge to the base of the waverider. As shown in Figure C.3, the shape of the waverider is dependent on the shape of the capture flow tube and the shock angle, which defines both the upper surface contour and the planform. Because of the attach-

6

ment of the shock at the leading edge, a two dimensional planar compressed flow is contained on the lower surface, which provides for efficient lifting pressures.

Several waverider concepts derived from two-dimensional planar flow fields are illustrated in Figure C.4. Experimental studies of Nonweiler's caret waverider concept indicated lower aerodynamic performance (i.e., lower lift-to-drag ratio) than was predicted [17]. In addition, equivalent delta wings having the same volume and projected planform were found to have equal or better performance than the caret waverider [17]. These caret waverider deficiencies have been attributed to their large wetted area and hence higher skin friction drag. Nonweiler also proposed the W-delta waverider concept [18], which consists of two caret wings which have been rolled in opposite directions and joined in the center. Flower's T-delta waverider is similar to Nonweiler's W-delta, but has a flat upper surface [19]. Woods developed the concave waverider concept, which was found to have better performance than either the caret waverider or the equivalent delta wing [20]. Townend proposed that a two-dimensional isentropic compression derived waverider would have improved lifting efficiency relative to the planar derived waverider [16]. Flower introduced the concept of shaping an expansion upper surface to develop efficient upper-surface lift; this concept was incorporated in the Y-delta and X-delta waverider concepts [19].

In 1963, Jones [21] presented a method of constructing the waverider lower surface using the known flow field past axisymmetric bodies. The basic design methodology, which was first developed for conical flow field, is illustrated in Figure C.5. The intersection of an arbitrary capture flow tube with a conical

7

shock defines the leading edge of the waverider. The shape of the waverider leading edge is dependent on the capture flow-tube shape and the shock angle (as was the case for the two dimensional planar shock case) and also is dependent on the distance of the capture flow tube from the conical shock centerline. The lower surface and upper surface are defined in the same manner as the two-dimensional planar flow-derived waveriders. In search of optimum waverider shapes, Cole and Zien [22] used hypersonic small disturbance theory to obtain inviscid flow solutions of axisymmetric bodies with longitudinal curvature.

Shown in Figure C.6 are several waverider concepts derived primarily from axisymmetric flow fields. Jones' cone derived waveriders were experimentally shown to develop the predicted compression surface pressures [23]. Rasmussen([24] and [25]) and Kim et al.([26] and [27]) investigated a series of circular and elliptic cone flow field derived waverider concepts. A sufficient number of waveriders were derived to indicate which shapes were optimum for a given Mach number and volume. Experimental studies showed that the performance was always lower than predicted. As was the case with the two-dimensional planar flow field derived waveriders, the performance deficiencies were attributed to viscous skin friction effects, which were not included in the optimization considerations. In order to address these deficiencies, Bowcutt and Anderson developed a numerical procedure for optimizing cone-derived waveriders which included the effects of skin friction drag within the optimization process ([28] and [29]). Waverider geometries designed using this optimization method are predicted to have very high performance relative to previous concepts. It is important to note

8

that since 1986, several additional waverider developments have occurred. Corda [30] extended the work of Bowcutt to include waveriders derived from any axisymmetric flow field. For example, a waverider derived from the flow field of a minimum drag body would be expected to have a lower drag than its cone flow derived counterpart. Mclaughlin [31] further extended the optimization methods to account for chemical equilibrium flow as opposed to the perfect gas assumptions used in the previous methods. Finally, Sobieczky has developed methods to derive waveriders from arbitrary shock shapes [32]. Rescently Jones et. al., [33] compared hypersonic waverider aerodynamic performance with numerical and experimental results.

1.3   Present Study

The present work is part of the continuing study of waveriders in the Hypersonic Group at the University of Maryland. The purposes of this research are to examine the viscous interaction effects on existing hypersonic waverider designs and to generate a new family of hypersonic waveriders wherein viscous interaction effects are included within the optimization process. In the process, through numerical experiments, the results/discussions presented in this work will also serve to clarify the physical aspects of viscous interaction on hypersonic waveriders.

The model of hypersonic flow over a sharp flat plate, at zero incidence angle, is applied along each streamline on the waverider surface. The rational for this geometry is based on the following comments:

1. The sharp flat plate is a "particularly appropriate model to examine the ef-

fects of the flow field development due to viscosity, apart from complicating effects of body geometry." [34]

2. The "magnitude of the viscous interaction is more significant for thin bodies such as flat plates and slender cones than for thick bodies, since for thin bodies the changes in effective geometry due to boundary- layer growth will be proportionally larger" [6]).

3. The combined conditions of high Mach number and low Reynolds number(high altitude) accentuate viscous interaction.

4. Assume at each streamline on waverider acts like two-dimensional flow on the flat plate.

Laminar flow is assumed – a valid assumption for high Mach, and relatively low Reynolds number flow. A number of parametric runs at different altitudes, and Mach numbers were carried out to examine viscous interaction effects on existing waverider designs and to generate a new family of waveriders wherein viscous interaction effects are included within the optimization process. A major objective of this work is to construct velocity-altitude maps delineating those flight regimes where viscous interaction effects are important for hypersonic waverider design.

1.4 Contribution to the State-of-the Art

This dissertation represents the first time that calculations have been made on waveriders including viscous interaction effects on existing waverider designs, and

also the first to generate a new family of waveriders wherein viscous interaction effects are included within the optimization process. Velocity–altitude maps are constructed clearly delineating those flight regimes where viscous interaction effects are important for waveriders in hypersonic flight. It is understood that viscous interaction effects are important at high Mach number and high altitude flight. However, answers to the following questions have not been available until now.

1. At what altitude and Mach number ranges are these viscous interaction effects important for hypersonic flight vehicle design?

2. How much does aerodynamic performance, differ from cases with and without viscous interaction effects?

3. How much are the waverider shapes changed, and what is the optimum shape with viscous interaction effects?

Answers to these questions constitute the main focus and contributions of the present dissertation.

Chapter 2

Method of Calculation

2.1 Classical Viscous Interaction Solution

On slender bodies at subsonic or low supersonic speeds at low altitude (hence high Reynolds number), the total streamline deflection induced by the boundary layer is of the order of the reciprocal of the square root of the local Reynolds number [35].

$$\frac{\delta}{x} \propto \frac{1}{\sqrt{Re_x}} \tag{2.1}$$

In this case, the effect on the pressure distribution will be inversely proportional to the square root of the Reynolds number, and it is negligibly small. On the other hand, at the hypersonic speeds the streamline deflection is of the order of its value at low Mach numbers multiplied by $M_e{}^2$, and the induced pressure on a slender body due to the interaction of the new effective body shape with the Mach waves in the inviscid field is of the order of the streamline deflection times M_e^2 [3]. To provide some insight on the relative thickness (δ) of a flat plate laminar boundary layer, Anderson [4] develops the following relation:

$$\frac{\delta}{x} \propto \frac{M_e^2}{\sqrt{R_e}} \qquad\qquad (2.2)$$

In the above, x is the "running-length" along the flat plate, M_e is the Mach number at the edge (e) of the boundary layer, and R_e is the Reynolds number based on edge conditions. Due to the square of the Mach number dependency, hypersonic boundary layers can be "orders of magnitude thicker than low speed boundary layers at the same Reynolds number" [4]. An interaction effect of this order of magnitude will be very important at large Mach number. The considerable distortion of the flow field about plane surfaces or slender bodies in hypersonic flow due to the boundary layer displacement effects are the result of the low mass flows involved in laminar boundary layers; this effect can take on considerable importance at high Mach numbers and low Reynolds numbers.

Classically, for the purposes of analysis, viscous interaction (pressure interaction)has been sub-divided into two categories, "strong" and "weak" interaction regions, such as shown in Figure C.7 (from Ref. [4]). In these two regions, $\frac{d\delta^*}{dx}$ is the rate of growth of the boundary layer displacement thickness (δ^*). In the region of strong interaction, clearly the growth of the displacement thickness is the "triggering mechanism" which ultimately results in the induced pressure along the body's surface. Therefore, the concept of "displacement thickness" is "key" to understanding viscous interaction – it is "physically the distance through which the external flow is displaced by the presence of the boundary layer" (refer to figure 1.1, obtained from [4]). The name "effective body" is given to the sum of

13

the actual body shape plus the displacement thickness. In figure 1.1, the shaded region is the "effective body".

Three important points characterizing the strong interaction region are:

1. In the leading edge region (strong interaction) the growth of the displacement thickness is large. As a result, the incoming freestream no longer "sees" a sharp flat plate. Rather, the plate "possesses, in a certain sense, a fictitious curvature because the presence of the viscous layer" [36] – an "effective body". Consequently, a curved "induced shock wave" [37] is generated at the leading edge.

2. The boundary layer strongly influences the outer inviscid flow. In turn, changes are "fed back" into the boundary layer.

3. Results of detailed analyses of the strong interaction zone have shown that the boundary layer thickness scales with the three-fourth power of the streamwise coordinate [38].

In contrast [4], the growth of the boundary layer is small in the weak interaction region. Thus, the inviscid flow is only slightly affected, and feedback is ignored.

Engineers are constantly in search of similarity parameters to assist in the collection and interpretation of data. The relevant parameter for this leading-edge viscous inviscid interaction problem was first pointed out by Lees and Probstein

[39]. The Lees and Probstein interaction parameter, defined as

$$\bar{\chi} \equiv \frac{M_\infty^3 \sqrt{C_w}}{\sqrt{Re_{x,\infty}}} \qquad (2.3)$$

in which the Chapman-Rubesin constant C in the linear viscosity-temperature law is defined as [40]

$$C_w = \left(\frac{\mu_w}{\mu_\infty}\right)\left(\frac{\rho_w}{\rho_\infty}\right) \qquad (2.4)$$

Since the pressure can be taken as constant across the boundary layer

$$C_w = \left(\frac{\mu_w}{\mu_\infty}\right)\left(\frac{T_\infty}{T_w}\right) \qquad (2.5)$$

We use the Sutherland model to calculate μ:

$$\frac{\mu}{\mu_o} = \left(\frac{T}{T_o}\right)^{\frac{3}{2}}\frac{T_o + 110^o K}{T + 110^o K} \qquad (2.6)$$

From classical hypersonic similarity theory, for all practical purposes we know that the Lees parameter characterizes the strength of the boundary layer/shock interaction. White [37] provides the following ranges on $\bar{\chi}$ — these can be used to predict the significance of viscous interaction for a specific application.

- $\bar{\chi} \ll 1$: negligible interaction effects.

- $\bar{\chi} = 0(1)$: weak interaction;

    can be computed by simply assuming supersonic inviscid flow over the

    (uncoupled) body shape $\delta^*(x)$.

15

- $\overline{\chi} \gg 1$: strong interaction;

  $\delta^*(x)$ and the external supersonic flow are strongly interdependent and must be solved simultaneously.

As it turns out, Bertram and Blackstock[41] derive an ordinary differential equation valid for all these regimes. which correlates P with the local slope of the boundary layer and correlates δ^* with the favorable gradient $P(x)$ through the similar solutions. White [42], following Bertram and Blackstock [41], showed from hypersonic similarity theory that the hypersonic boundary layer displacement thickness could be represented as

$$\frac{\delta^*}{x} = \frac{1}{M_\infty} \frac{2\Lambda}{\sqrt{P}}$$

(2.7)

where $P \equiv \frac{P_t}{P_\infty}$, the pressure ratio across the shock and Λ a term is defined in equation 2.13. The pressure gradient due to shock curvature is assumed negligible, as Bertram and Blackstock demonstrated. Note that in the hypersonic limit, the mass flux in the boundary layer is so low that displacement thickness is approximately equal to the actual boundary layer thickness. The calculation of P is based upon the tangent wedge theory, which assumes that the local pressure at any point where the body slope is $\theta(x)$ is given by supersonic flow past a wedge of the same angle θ. This is known to be a good approximation at high Mach number [5]. At hypersonic speeds, wedge theory for P reduces to a simple formula which depends only on the specific heat ratio and single hypersonic similarity parameter. At any angle, Shapiro[44] has shown that

$$p = 1 + \frac{\gamma M^2}{2} C_p$$

(2.8)

16

where the pressure coefficient Cp is given by

$$\frac{Cp}{[1 - \frac{1}{2}Cp]} = \frac{4M^2 \sin^2 \beta - 1}{M^2(\gamma + \cos \beta) + 2} \qquad (2.9)$$

A closed-form solution for shock pressure ratio can be found at large Mach numbers and small wedge angles such that $tan\Theta_{wedge} \simeq \Theta_{wedge}$ and $cos\beta_{shock} \simeq 1$, $C_p \ll 1$:

$$P = 1 + \frac{\gamma(\gamma + 1)}{4}K^2 + \gamma K \sqrt{1 + (\frac{\gamma + 1}{4}K)^2} \qquad (2.10)$$

where the hypersonic similarity parameter is

$$K = M_\infty(\Theta_{wedge} + \frac{d\delta_{b.l.}^*}{dx}) \qquad (2.11)$$

This formula is valid whenever $K = 0(1)$ and θ is less than about 20 degree [37]. The second angle term, due to the boundary layer slope, is transformed into a function of the Lees parameter:

$$\frac{d\delta_{b.l.}^*}{dx} = \frac{\Lambda}{M_\infty}(\frac{1}{\sqrt{P}} + \frac{\bar{\chi}}{2P^{\frac{3}{2}}}\frac{dP}{d\bar{\chi}}) \qquad (2.12)$$

from Eq.(2.11) Note that as $\bar{\chi} \to 0$, the hypersonic similarity parameter K approaches $M_\infty\Theta_{wedge}$ as should be the case in the weak interaction zone.

The Λ function characterizes the gas/wall heat transfer, and is here written for general Prandtl number, Pr; this form was determined by Lewis [43] fitting the results for Pr =1. and Pr =.73 to a power law form;

$$\Lambda = \{0.4302Pr^{0.1344}(\frac{T_w}{T_{ad}}) + 0.1660Pr^{0.2854}\}(\gamma - 1)\bar{\chi} \qquad (2.13)$$

along the plate, in the so-called weak interaction region. Thus, for large values of x, corresponding to small values of $\bar{\chi}$,

17

$$\frac{\delta^*}{x} \simeq \frac{2\Lambda}{M_\infty} \qquad (2.14)$$

with a slope that approaches zero as x → ∞.

It is assumed that the total wedge angle is positive, or else the forebody flow would have to be treated as an expansion flow. The above model is iterated in $\overline{\chi}$, which is an inverted spatial coordinate:

$$\lim_{\overline{\chi} \to 0} x = \infty \qquad (2.15)$$

$$\lim_{\overline{\chi} \to \infty} x = 0 \qquad (2.16)$$

Thus, the solution begins at the weak interaction limit and proceeds to the strong interaction limit. In the present implementation, a simple Euler forward iteration scheme is used. The derivative in equation(2.12) is calculated with a finite difference method between two closely spaced values of $P(\overline{\chi})$. Smaller increments are required at large $\overline{\chi}$ to adequately resolve the strong interaction region.

For application to a waverider, it is assumed apply *locally* along each streamline over the surface of the waverider. This appears to be justified because the streamlines over a waverider have very little transverse curvature; they are reasonably straight. Moreover, the pressure gradients along the surface stream-lines are small(in the non-interaction case), and therefore it appears reasonable to apply the above flat plate analysis locally at each point along a streamline. In equations (2.3) — (2.14), wherever freestream variables appear, denoted by the subscript infinity, these are replaced by the local values at each point along

a surface streamline as calculated from the standard, non–interaction, waverider analysis. For example, in equation (2.10), P_∞ is replaced by the local static pressure at a given point along the waverider streamline as calculated from the non–interaction analysis, and P_e as calculated from equation (2.10) then represents the pressure on the waverider surface at that point, including the induced pressure increment due to viscous interaction.

2.2 Skin Friction Coefficient

An important aspect of the present work is the inclusion of viscous interaction effects within the waverider optimization process itself. Although the waveriders are carved from inviscid flow fields, as will be discussed in the next chapter, a locally, two–dimensional viscous interaction analysis is performed on the waverider along each streamline at every level of the optimization.

The hypersonic flow field through an oblique shock is nearly unchanged for small deflection angles. This means that under conditions compatible with hypersonic similarity, the skin friction and heat transfer merely change inversely with the boundary layer thickness. So we can use Reynolds analogy for the skin friction calculations. The skin friction distribution along the streamlines that form the waverider is calculated using the flat plate viscous interaction solution. In the use of Reynolds analogy for the present work, approximate formulas are used to predict the skin friction, with the physical properties evaluated with the increased pressure due to the viscous interaction.

For the laminar flow over a flat plate, the local skin friction coefficient is

given by

$$C_f = 2C_h = 0.664\sqrt{\frac{PC_w}{Re_x}} \qquad (2.17)$$

Re_x is the local Reynolds number defined as

$$Re_x = \frac{\rho_\infty V_\infty x}{\mu_\infty} \qquad (2.18)$$

where the subscript e denotes conditions at the edge of the boundary layer. Also in equation 2.17, P is the pressure ratio defined as

$$P = \frac{P_e}{P_\infty} \qquad (2.19)$$

The shear stress is evaluated as

$$\tau = C_f\, q_\infty = C_f\, (\frac{1}{2}\rho_\infty V_\infty^2) \qquad (2.20)$$

For calculating the waverider skin friction drag, this shear stress is calculated along each stream line, and then integrated along the complete waverider surface.

2.3 Procedure for Examing the Viscous Interaction Regime

The investigation was carried out for many predetermined altitude–Mach number points with the altitude varying from 20 – 80 Km and the Mach number varying from 3 – 30. A 5% or more reduction in the maximum Lift/Drag for an optimum waverider shape at a particular altitude–Mach number point was used as a criterion to determine if viscous interactions were important.

1. Because Corda's code utilized the reference temperature method, the input of a wall temperature was required as a boundary condition. Instead of just randomly choosing a wall temperature, it was decided to set $T_w/T_{aw} = 0.33$ all cases. This implies that whenever T_{aw} changes due to a change in M_∞, T_w also changes accordingly.

2. Corda's code was run using 100 iterations for optimization to obtain the viscous optimized waverider shape with the largest maximum Lift/Drag a given the altitude–Mach number point. The code had to be run a number of times at the given altitude–Mach number point, wherein the cone angle of the body used to generate the flow field was varied. This would yield the optimum of optimums, the best viscous optimized waverider shape with the largest maximum Lift/Drag for the altitude–Mach number point.

3. The viscous interaction code was run using no additional optimization by inputing the leading edge geometry of the best viscous optimized waverider shape determined in step 2 and the same cone angle used to generate the same flow field. This forced the code to determine the characteristics of the

21

same viscous optimized waverider shape obtained in step 2, but the effects of viscous interactions were now included in the analysis. this allowed for a comparison to be made to determine if viscous interactions were important.

4. The maximum Lift/Drag values obtained in steps 2 and 3 were compared. If the value for the maximum Lift/Drag determined in step 2 exceeded the value determined in step 3 by 5% or more, viscous interaction were said to be important and should be considered in the analysis of viscous optimized waveriders at that altitude–Mach number point.

5. If viscous interactions were found to be important in step 4, The viscous interaction code was run at the altitude–Mach number point. It was run in the same manner as Corda's was in step 2. This would yield the new family of best viscous optimized waverider shape with the inclusion of viscous interaction effects in its generation analysis.

Throughout the investigation the slenderness or base to length ratio was constrained to 0.075, and the length was 60 meter for all of the waverider shapes generated. This was done so the waveriders would be analogous to actual hypersonic vehicles.

Chapter 3

Waverider Construction

For the single waverider construction, two basic functions need to be performed. First, a flow field solution must be obtained around some generating body, which, as stated in the introduction, is the basic premise of the waverider concept. In the present work, cones are used as the generating bodies; an inviscid flow of a calorically perfect gas is assumed. Second, once the flow field solution has been obtained, it is redefined so that a stream function may be generated on a workable grid to allow for streamline tracing. Once these two tasks have been completed, it is possible to carve any number of different waveriders from a single generating flow field. The solutions of the generating flow fields, the redefinition of the generating flow field, and the construction of a single waverider geometry, are described in the Ph. D. dissertation of Stephen Corda [30] and the master thesis of the Thomas McLaughlin [31]. So as to make the present dissertation more self-contained, the description that appears in Reference 30 and 31 is repeated here in appendix A. The reader is referred to appendix A for all the details. For all practical purposes, appendix A is chapter 3 of this dissertation.

Chapter 4

Aerodynamic Analysis of a Waverider Configuration

4.1 Inviscid Aerodynamic Analysis

The inviscid lift, drag, and moment are obtained by numerically integrating the pressure distribution over the surface of the waverider. Recall that the waverider surface is defined by 51 streamlines. Flow properties are known along these streamlines from the space-marching flow field solution. The inviscid lift, L_p, is calculated by integrating (in cartesian coordinates x and z) over the projected planform area as given below.

$$L_p = 2 \int_0^l \int_0^{x=f(z)} P(x,z) \, dx \, dz \qquad (4.1)$$

where P(x,z) is the pressure distribution on the waverider surface, l is the length of the waverider, f(z) is the function that defines the planform in the (x,z) plane, 0 denotes the origin of coordinates (at the nosetip of the waverider), and the factor of 2 accounts for the fact that the actual integration is performed over half of the vehicle due to symmetry.

Similarly, the inviscid drag, D_P, is obtained by integrating (in polar coor-

dinates r and θ) over the base area of the waverider as follows.

$$D_p = 2 \int_0^{\pi/2} \int_0^{r=g(\theta)} [p(r,\theta) - p_\infty] \; r \; dr \; d\theta \tag{4.2}$$

where $p(r,\theta)$ is the pressure distribution over the surface of the waverider, P_∞ is the freestream pressure, $g(\theta)$ is the function that defines the base in the (x,y) plane, and 0 denotes the origin of coordinates (centerline of the waverider).

The pitching moment about the waverider leading edge or nose is calculated by performing similar integrations over the planform and base area of the waverider. The contribution to the pitching moment due to the pressure distribution over the planform area, $M_{p,plan}$, is given by

$$M_{p,plan} = 2 \int_0^l \int_0^{x=f(z)} p(x,z) \; z \; dx \; dz \tag{4.3}$$

The pitching moment due to the pressure distribution over the waverider base, $M_{p,base}$, is given by

$$M_{p,base} = 2 \int_0^{\pi/2} \int_0^{r=g(\theta)} p(r,\theta) \; r^2 \; dr \; d\theta \tag{4.4}$$

The total pitching moment due to the inviscid forces, M_p, is the sum of equations 4.3 and 4.4.

$$M_p = M_{p,plan} + M_{p,base} \tag{4.5}$$

The integrations is equations 4.1 through 4.4 are evaluated numerically, using the composite trapezoidal rule [45] as given below for an arbitrary function, f, of two variables, x and y.

$$\int_a^b \int_{c(x)}^{d(x)} f(x,y) dy dx =$$

$$\frac{b-a}{4}\{[d(a) - c(a)][f(a, c(a)) + f(a, d(a))] +$$

$$[d(b) - c(b)][f(b, c(b)) + f(b, d(b))]\} \tag{4.6}$$

4.2 Viscous Aerodynamic Analysis

The calculation of the lift, drag, and moment due to the skin friction distribution over the waverider surface is conceptually similar to the aerodynamic analysis due to the pressure distribution. Values of the shear stress are again known along the streamlines that describe the waverider's upper and lower surface. Using the values of C_f that have just been calculated, the viscous shear stress forces can be determined and then integrated over the surfaces of the waverider. Determining the shear stress force, τ, at a given point on one of the waverider surfaces is a matter of multiplying the local skin friction coefficient, C_f, by the local edge dynamic pressure, q_e such that

$$\tau_i = (C_f \, q_e)_i \tag{4.7}$$

This calculation is performed at each of the points that define the waverider. Once the shear stress distribution is known, the surfaces of the waverider are divided into triangular panels, as described in a paneling scheme is used where the vertices of triangular panels correspond to data points along the streamlines that describe the waverider. Knowing the value of the shear stress at the corners of a triangular panel (τ_1, τ_2 and τ_3), the average value of the shear stress, τ_{avg}, over the panel is given by

$$\tau_{avg} = \frac{1}{3}(\tau_1 + \tau_2 + \tau_3) \tag{4.8}$$

The viscous force over a panel, F_{panel}, is given by

$$F_{panel} = \tau_{avg} A_{panel} \qquad (4.9)$$

The area of a panel, A_{panel}, in equation 4.9, is defined for an arbitrary panel as

$$A_{panel} = \sqrt{s(s-a)(s-b)(s-c)} \qquad (4.10)$$

where a, b, and c are the lengths of the sides of the triangular panel and s is defined as

$$s = \frac{1}{2}(a+b+c) \qquad (4.11)$$

The viscous force on a panel is separated into lift and drag components, $L_{\tau,panel}$ and $D_{\tau,panel}$ respectively, as shown in Figure C.14. The lift and drag components are defined as

$$L_{\tau,panel} = F_{panel} \ \cos(\theta_{yh}) \ \sin(\theta_{xz}) \qquad (4.12)$$

$$D_{\tau,panel} = F_{panel} \ \cos(\theta_{yh}) \ \cos(\theta_{xz}) \qquad (4.13)$$

where $F_{panel} \cos(\theta_{yh})$ is the component of the force in the (x-z) plane.

It is assumed that the forces act at the shear stress weighted centroid of the panel. The y and z coordinates of this centroid are needed to evaluate the pitching moment. These coordinates are given by

$$Y_c = \frac{y_1 \tau_1 + y_2 \tau_2 + y_3 \tau_3}{\tau_{avg}} \qquad (4.14)$$

$$Z_c = \frac{z_1 \tau_1 + z_2 \tau_2 + z_3 \tau_3}{\tau_{avg}} \qquad (4.15)$$

These coordinates are measured from the leading edge of nose of the waverider. The contribution to the pitching moment about the leading edge due to the viscous forces on a panel, $M_{\tau,panel}$, is defined as

$$M_{\tau,panel} = -Y_c D_{\tau,panel} + Z_c L_{\tau,panel} \qquad (4.16)$$

The total lift, drag, and pitching moment due to skin friction are obtained by summing over all of the panels.

$$L_\tau = \sum_{i=1}^{N} L_{\tau,i} \qquad (4.17)$$

$$D_\tau = \sum_{i=1}^{N} D_{\tau,i} \qquad (4.18)$$

$$M_\tau = \sum_{i=1}^{N} M_{\tau,i} \qquad (4.19)$$

where the index i specifies a particular panel and N is the number of panels.

4.3 Total Aerodynamic Forces and Moments

The total aerodynamic forces and moments on the waverider is simply the sum of the contributions due to the inviscid (pressure) and viscous (shear stress) sources. The total lift, drag, and pitching moment about the leading edge are defined as

$$L = L_p + L_\tau \qquad (4.20)$$

$$D = D_p + D_\tau \qquad (4.21)$$

$$M = M_p + M_\tau \qquad (4.22)$$

Aerodynamic coefficients can be defined any of the terms in equations 4.20

through 4.22. The total lift, drag, and moment coefficients are defined as

$$C_L = \frac{L}{q_\infty S} \tag{4.23}$$

$$C_D = \frac{D}{q_\infty S} \tag{4.24}$$

$$C_M = \frac{M}{q_\infty S l} \tag{4.25}$$

where S is the waverider planform area, l is the centerline length of the waverider, and q_∞ is the freestream dynamic pressure, defined as

$$q_\infty = \frac{1}{2}\rho_\infty V_\infty^2 \tag{4.26}$$

The lift to drag ratio is simply defined, using equations 4.23 and 4.24, as

$$L/D = C_L/C_D \tag{4.27}$$

This concludes the aerodynamic analysis of a single waverider configuration. Once again, recall that the results of the entire waverider construction and corresponding aerodynamic analysis are completely dependent on the choice of the initial five leading edge points, once the generating flow field is defined. This fact is important to the optimization procedure described in the next chapter.

Chapter 5

Waverider Optimization

The goal of the optimization procedure is to find the best performance waverider (optimized for one figure of merit) within a given generating flow field. The construction and aerodynamic analysis of a single waverider configuration is shown by Chapter 3 and 4. The numerical optimization routine wraps itself around this core analysis of a single waverider. The optimization is performed by perturbing the shape of the leading edge curve (which corresponds to a unique waverider geometry), until a configuration is found with the optimum value of the specified figure of merit – a maximum lift-to-drag ratio. The optimization procedure used in the present work, is based directly on the work of Corda. Defining the current situation in more concrete terms, we have one figure of merit associated with one waverider, which it turn is defined by five leading edge points. Each of these five leading edge points is defined by two coordinates in the x-y plane which results in eight degrees of freedom for the definition of a single waverider, and hence, a single figure of merit. The details of the numerical optimization procedure will be discussed first.

5.1 The Simplex Optimization Method

The non-linear simplex method of Nelder and Mead [46] is used for the numerical optimization. This is a zero order method – only function evaluations are needed to find an optimum (no derivative information is required). These function evaluations are the calculations of the figure of merit (e.g. L/D or C_D) for each configuration.

The non-linear simplex method minimizes a function of n variables by comparing values of the function at (n+1) vertices of a "simplex". The vertex with the highest function value is replaced by another point, determined by the logic of the scheme, with a lower function value. The simplex "moves" over the function surface in the direction of the function minimum. Three operations are used by the simplex in its search for the function minimum – reflection, expansion, and contraction. These operations are graphically illustrated by considering the minimization problem shown in Figure C.15. Here, the minimum of a function of two variables (x1 and x2) is sought, where the surface defines the function. A simplex composed of n+1 =3 vertices (a triangle) moves over the function surface by reflecting or "flip-flopping" up or down the function valley, expanding if possible to speed up the process, and finally contracting around the function minimum. The following outlines the simplex method for the minimization of a function.

1. Define the object function F as a function of n variables

$$F \;=\; F(x_1, x_2, x_3, \ldots, x_n) \qquad (5.1)$$

31

The minimum value of this function is sought.

2. Generate an initial (n+1) dimensional polytrope or simplex. (The generation of this initial simplex is discussed in section 5.3.) Each vertex of the simplex is represented by a vector of the variables, For the jth vertex, this vector is given by

$$X_j = X_j(x_1, x_2, x_3, \ldots, x_n) \tag{5.2}$$

3. Evaluate the object function, F, at each simplex vertex.

4. Order the object functions in step 3 such that

$$F_1 < F_2 < F_3 < \ldots < F_n < F_{n+1}$$

The logic of the simplex method replaces the vertex with the highest function value, X_{n+1}, with a vertex corresponding to a lower function value.

5. Calculate the centroid, $\overline{C}$, of the best n vertices.

$$\overline{C} = \frac{1}{N} \sum_{j=1}^{n} X_j \tag{5.3}$$

6. Generate a new vertex by reflection. This vertex is represented by the vector X_r given by

$$X_r = \overline{C} + \alpha(\overline{C} - X_{n+1}) \tag{5.4}$$

where α is the reflection coefficient.

7. Evaluate the object function at the reflected point, $F_r(X_r)$. Three options are now available:

a If X_r is not a new best point or a new worst point, $(F_1 < F_r < F_n)$, then the vertex, X_r, replaces the old worst vertex, X_{n+1}, and a new iteration is begun(return to step 4).

b If X_r is the new best point $(F_r < F_1)$, then it is assumed that the direction of reflection is "good" and an expansion is defined by

$$X_e = X_r + \gamma(X_r - \overline{C}) \qquad (5.5)$$

where γ is the expansion coefficient. If the expansion is successful $(F_e < F_r)$ then X_e replaces X_{n+1}. If the expansion fails $(F_e > F_r)$ then X_r replaces X_{n+1}. A new iteration is now begun (return to step 4).

c If the simplex is too large $(F_r > F_n)$ then a contraction is defined by

$$X_c = \overline{C} + \beta(X_{n+1} - \overline{C}) \quad if \quad F_r > F_{n+1} \qquad (5.6)$$

$$X_c = \overline{C} + \beta(X_r - \overline{C}) \quad if \quad F_r < F_{n+1} \qquad (5.7)$$

where β is the contraction coefficient. If the contraction is successful $(F_c < min\{F_r, F_{n+1}\})$ then X_c replaces X_{n+1}. If the contraction fails $(F_c > min\{F_r, F_{n+1}\})$ then the entire simplex is contracted according to

$$X_c = \frac{1}{2}(X_c + X_1) \qquad (5.8)$$

A new iteration is now begun (return to step 4).

8. The optimization is halted after a specified number of iterations.

An optimization level concludes each time a new simplex is created, and by continuing this procedure over a number of optimization levels, a minimum to the function is eventually reached. A physical description of the algorithm has been presented above to give the reader a flavor of how the optimization process proceeds.

5.2 Application to Current Study

The procedure described above is easily extended to minimize a function of eight variables. The simplex becomes "nine-sided", and operates in an eight-dimensional space. Each function evaluation, in the current study, is the negative of the lift over drag ratio, and is analogous to the elevation of a given node in the above description. In addition, since each leading edge shape defines a particular waverider, each new location in the domain of the mountain analogy corresponds to new leading edge shape. The result of this is that by parameterizing the leading edge shape, an optimum waverider can be found.

The domain of the optimization is controlled by the user in the present study. This is accomplished by enforcing constraints on the generation of each new node of the simplex, and hence on each new waverider that is created. For example, if a specific minimum slenderness ratio is set by the user and a waverider is created that falls below this minimum, then that node is not allowed to be created, and simplex optimization must operate within these bounds.

34

Certain constraints must be enforced in order to create valid waveriders, and to have control over the optimization procedure. Each constraint is stated and discussed in the following sections.

Recall that the leading edge curve projected in the x-y plane is the initial parameter that needs to be specified in order to create a single waverider. Past experience in generating waveriders, gained by Bowcutt and Corda, has shown that there are a number of restrictions that need to be placed on the geometry of each leading edge in order to insure that a valid waverider is constructed. The reasons for some of these constraints are relatively obvious, while others are somewhat subtle.

Constraints on the leading edge shapes:

1. The second leading edge point away from the centerline cannot be on the line of symmetry. — If this were to occur, the resulting waverider would have a sharp spike on the upper surface which is undesirable. In addition two streamlines would lie in the same flow plane. This, too should be avoided because problems will arise in the integration of the waverider volume and surface areas.

2. All leading edge points must lie within the shock wave.— Since the flowfield is not defined outside for the shock wave, the streamlines, resulting in extra surfaces. More importantly, the shock wave would not be attached to the leading edge, which violated the basic waverider premise.

3. The radial distance to each of the leading edge points from the centerline

to the shock wave must continually increase. — In some cases, a violation of this occurrence will cause the waverider's upper and lower surfaces to cross over each other. This is obviously an unrealistic result.

4. The polar angle to each of the leading edge points from the centerline to the shock wave must continually increase. — A violation of this occurrence also causes the waverider's upper and lower surfaces to cross each other.

A completely different set of constraints are placed on the entire vehicle geometry for the optimization procedure. For each of these cases, even though a valid leading edge is created, the resulting waverider may exceed other limits imposed by the user. The user imposed limits provide a control mechanism over the optimization procedure. The simplex is never allowed to move beyond these bounds, and therefore some control is gained over which local minimum is found by the optimization procedure. All of the constraints listed below have the option of being made inactive. This is sometimes done since it is occasionally necessary to relax some of the constraints to allow the optimization procedure to continue operating properly.

Constraints on the Vehicle Geometry:

1. Minimum Slenderness Ratio — The user can adjust this constraint to limit the lower bound of the slenderness ratio of the vehicle. Any vehicle that has a slenderness below this minimum is discarded by the optimization procedure.

2. Box Size — The user can set both the upper and lower bounds on the box

size of the vehicle. The box size is defined as the semi-span to length ratio of the vehicle. This constraint can be imposed to keep the waverider planform narrow,or it can be relaxed to allow the waverider to have a wide planform. The suggested values for these parameters are $0.1 < \frac{b/L}{L} < 0.4$. These are the values that are used for most of the applications in the present study. Any vehicles outside of these bounds are discarded by the optimization procedure.

3. Volume — The user can also impose limits on the minimum and maximum volume of the waveriders. This is useful when optimizing for maximum L/D since no waverider will be considered if it has a volume below this minimum. The maximum limit is useful when relaxing either the slenderness ratio or box size constraints. This keeps the waveriders for getting drastically out of proportion in some of these cases.

For each optimized waverider, between seventy and one-hundred optimization levels are run to achieve a converged solution. These numbers are determined by experiment and prove to be acceptable for all of the cases that are run in this study. A typical optimization history is shown in Figure C.16.

Values of the coefficients α, β and γ of 1, 0.5, and 2 respectively are use in the present study. These are the values suggested by Nelder and Mead[46]. For an interesting treatment of the application of the simplex method, and also other higher-order methods, to optimization problems similar to the present study, see

37

the work by Van Wie [47].

5.3   The Leading Edge Shapes

It is clear that the simplex optimization procedure is able to minimize a given function, but recall the minimum that the simplex finds is a local minimum. Since a set of somewhat arbitrary points is chosen to start the optimization, the choice of the nine initial (or "basis") leading edge shapes will influence which particular minimum is found.

An effort is made to select a diverse set of basis leading edge curves. Six of the basis leading edge shapes are polynomials of the form

$$Y_{le} = C_1 + C_2 X_{le} + C_3 X_{le}^2 + C_4 X_{le}^3 \tag{5.9}$$

and three of the basis shapes are of the form

$$Y_{le} = C_5 + C_6 \left(1 - \cos\frac{\pi X_{le}}{r_s}\right) \tag{5.10}$$

$$Y_{le} = C_7 + C_8 \sin\left(\frac{\pi X_{le}}{r_s}\right) \tag{5.11}$$

where X_{le} and Y_{le} are the X and Y coordinates of the leading edge and r_s is the radius of the shock wave at the base of the waverider. By chosing a set of basis leading edge shapes that are all similar, the optimum waverider will most likely be of the same general nature as leading edge shapes. Choosing a diverse set of leading edge shapes, however, will allow the initial simplex to encompass many more possible minimums, and provide the opportunity for the optimization

procedure to find a "better" minimum.

In the present work, both methods of chosing the basis leading edge shapes are used. For cases in which a particular type of resulting leading edge shape is desired beforehand, a set of similar basis leading edge shapes are chosen. For most cases, however, a diverse set of leading edges are chosen as shown in Figure C.17. The final optimized leading edge shape is also shown as the bold curve in this figure.

This set of leading edge shapes consists of two horizontal linear curves, three first order polynomials, two second order polynomials, and two trigonometric functions. For cases in which rounded leading edges are desired, all of the leading edge shapes are moved away from the origin, made to be nonlinear, and kept similar to each other in their general shape.

A small parametric study is performed to examine the effects of varying the basis leading edge shapes between these two extremes. In most cases the effects are small enough to ignore, since the figures of merit change by only a few percent. In some cases, however, the choice of the basis leading edge shapes causes the optimization procedure to find a completely different waverider class.

Chapter 6

Results and Discussion

6.1 Computer Code Validation

The initial portion of the work in the present study is the calculation of viscous interaction on a flat plate in hypersonic flow as described in Chapter 2. The first step in validating the present code is to insure that the computed distribution of induced pressure versus $\bar{\chi}$ on a flat plate is the same as that obtained from previous solutions in the literature. Results from Chapter 2 are compared against the results in reference [37] as well as analytical expressions given by Hayes and Probstein's[5] for the induced pressures as a function of $\bar{\chi}$.

For an insulated flat plate, the induced pressure for both the strong and weak interactions are given by:

$$\frac{P}{P_\infty} = 0.759 + 0.514\bar{\chi}$$
$$\frac{P}{P_\infty} = 1 + 0.31\bar{\chi} + 0.05\bar{\chi}^2$$

For a cold wall case, where $T_w \ll T_{aw}$, the expressions are as follows:

$$\frac{P}{P_\infty} = 1 + 0.15\bar{\chi}$$

$$\frac{P}{P_\infty} = 1 + 0.078\overline{\chi}$$

The viscous interaction parameter, $\overline{\chi}$, is indicative of the strength of the hypersonic viscous interaction. White[37] provides ranges for $\overline{\chi}$ for both the strong interaction region and the weak interaction region. These are presented in section 2.1. They can be used to predict the significance of viscous interaction for a specific application. The results are presented in figures 6.1 - 6.3 and are discussed below:

1. In Figure C.18, the induced pressure ratio is plotted as a function of, Λ, a stretching variable used by White to make his differential equation for the interaction independent of growth parameter, a. This growth parameter is given by, the following,

$$a = 0.425(\frac{Tw}{Taw} + 0.35)(\gamma - 1)$$

The solutions were generated for an insulated wall with a=0.23. The computed results show good agreement with those given by White's method.

2. In Figure C.19, the pressure ratio is plotted function of $\overline{\chi}$ from the trailing edge to leading edge. The freestream conditions are that for Mach 6 flow at 60 kilometers. The computed solutions which follow Bertram and Blackstock's formulation and those given by White are in good agreement.

3. In Figure C.20, solutions given by Hayes and Probstein, and White are compared to the present calculations for a cold wall case with a=0.07. Again

these results are in good agreement with each other with all solutions falling along the same line. Note that for the cold wall solution the induced pressure ratio is approximately four times lower than for the insulated plate.

Thus, it is shown in Figures C.18 to C.20 that the method of solution, adapted from Bertram and Blackstock, predicts the correct pressure distribution for a given value of the interaction parameter.

The next step in the code validation procedure was to make sure that given a leading edge curve, the same waverider results as those obtained using Corda's method[30] were obtained. Corda's waverider generation has been well validated both numerically and experimentally, and for this reason, is used here for comparison. Using Corda's code, a 60 meter waverider was generated from five leading edge coordinates at a given flight condition and cone angle. This waverider was optimized for maximum L/D. This resulting waverider was compared to one generated by the current code using the same leading edge points but inducing the effects of viscous interaction. Geometric parameters for both cases are given in Table B.1. Note that the major differences occurred in waverider volume. This is due to the accumulation error when the volume is integrated over the cross-sectional areas. These trends were also found by Mclaughlin[31]. Despite these small differences, the numbers indicate that the two codes do produce the same waverider shapes. These are shown in Figures C.21 and C.22.

6.2 Viscous Interaction Flight Regime

One of the primary goals of the present study was to determine the range of Mach numbers and altitude for which viscous interaction becomes significant for hypersonic flight vehicles. This range was determined on the basis of a comparison of waveriders designed with and without the inclusion of viscous interaction effects.

In order to have a valid basis of comparison, two waveriders were generated using the same cone angle, flight conditions, and construction process. The flight regimes have been constructed on the basis of 5% or more reduction in optimum L/D when viscous interactions are considered at a given Mach number–altitude design point for all cases, a cold wall was assumed with $T_w/T_{aw} = 0.33$. It should be noted however that data for the low speed , high altitude range was not obtainable for the given waverider optimization constraint.

From the above described process, a Mach number–altitude map was constructed and is illustrated in Figure C.23. The heavy solid line separates the viscous interaction region from the region where this interaction is negligible or nonexistent. Thus, for vehicles planning on operating in viscous interaction regime, the viscous interaction effect may be excluded from their design. However, if a vehicle is to be designed for flight conditions above this line, the shaded region in Figure C.23 is that region where viscous interaction effects must be included. This region was mapped by running hundreds of different waverider calculations for different Mach and Reynolds numbers. For a waverider larger

than a 60m length , the boundary will move upwards and to right; the adverse effects of viscous interactions will be shifted to larger Mach numbers and higher altitudes. In contrast, for a waverider smaller than a 60m length, the boundary will move down and to the left in Figure C.23.

To illustrate the importance of viscous interaction on current high speed vehicles, the space shuttle trajectories and the anticipated NASP flight envelop are superimposed from Reference [48] and [49]. For the space shuttle trajectories, these calculations show that viscous interaction on the waveriders become important above Mach numbers of six and altitudes greater 200,000 feet on the ascent flight trajectory. Upon entry, the waverider is subjected to this effect until the Mach number and altitude fall below 14 and 180,000 feet respectively. Within the NASP flight envelope, viscous interaction is important above 160,000 feet at Mach number 15 and 140,000 feet at Mach number 16.

It was also determined that viscous interactions become stronger as the viscous interaction flight regime is further penetrated. At a constant Mach number, viscous interactions become stronger as altitude is increased, and at a constant altitude, they become stronger as the Mach number is increased.

6.3 Viscous Interaction Effects on Waverider Geometry and Performance

A primary objective of the present study is to determine the effect of viscous interaction on the geometric shape and aerodynamic performance of existing hypersonic optimized waveriders. In the present work, maximum lift over drag

44

ratio waveriders are generated by using the L/D parameter as the figure of merit in the optimization procedure. This waverider class is aimed at producing the best cruise configuration for hypersonic vehicles. No effort is made to reduce the total drag, achieve a high volume, or enhance the volumetric efficiency of the vehicle. Effort is only made to achieve a high lift over drag ratio. Results are presented in this section for waveriders constructed both with and without viscous interaction based on a 60 meter length for Mach numbers of 6.0, 10.0, 15.0, 20.0, and 25.

In the generation process of an optimized waverider several quantities were specified as follows. The slenderness ratio, defined as the ratio of base height to length, was set equal to 0.075. The box size, defined as the semi–span to length ratio, was set to BOXMAX=0.4 and BOXMIN=0.1, also in all cases, a cold wall was assumed with $T_w/T_{aw}=0.33$.

6.3.1 Results of Viscous Interaction Effects at an Altitude 50 km

In this section waveriders with and without the inclusion of viscous interaction are compared for various Mach numbers at an altitude of 50 kilometers. Again, to have a valid comparison of the waveriders the same leading edge points are used to generate each set of waveriders at the given flight condition. The results presented herein show the effect of the interaction on the maximum L/D; lift coefficient, C_L; and the drag coefficient, C_D, also pressure distributions are shown as a function of $\overline{\chi}$ and actual waverider shapes for each pair of waveriders generated are presented.

By first examining the definition of $\overline{\chi}$, the governing similarity parameter of viscous interactions, it is evident that an increasing Mach number, increases $\overline{\chi}$ directly. Also, since $\overline{\chi}$ is inversely proportional to the square root of the Reynolds number, a decrease in Reynolds number due to an increase in altitude also increases $\overline{\chi}$. Since the viscous interaction effect becomes greater for higher values of $\overline{\chi}$, it is expected that high Mach number, low altitude conditions produce strong viscous interaction effects.

Distribution of $\overline{\chi}$ are shown in Figures C.24 and C.25 for the best viscous optimized waverider shapes analyzed in step 3 in section 2.3 for Mach 15 and Mach 25 at 50 km. The distributions are presented for streamline #1, the streamline directly down the center of a waverider on both the upper and lower surfaces. The distributions presented in both these two figures agree with well–documented trends of $\overline{\chi}$ along a flat plate. It is very large near the leading edge where strong viscous interactions exist due to the large boundary layer growth rate in this region and then tapers off to a small value further downstream where weak viscous interactions exist due to the moderate boundary layer growth rate. Note also that the $\overline{\chi}$ values are three times greater in Figure C.26 for the case of Mach 25 than in Figure C.25 when Mach 15. This can be correlated with the previous conclusion that viscous interactions increase with increasing Mach number. Also, an interesting result related to the general concept of a waverider is the significant difference between the $\overline{\chi}$ values for the top and bottom surfaces. The values of $\overline{\chi}$ are much larger for the top surface because the top surface is designed to be a surface parallel to the freestream which acts in a manner much like the flat plate

46

shown in Figure C.1. The bottom surface, however, has lower values of $\overline{\chi}$ because the waverider is designed such that the bottom surface is a compression surface and flow must first pass through a shock wave attached along its entire leading. This reduces the Mach number and increases the density, therefore reducing the subsequent values of $\overline{\chi}$.

Figures C.26 and C.27 illustrate the top and bottom pressure distributions for both Mach number 15 and Mach number 25 along streamline #1. The surface pressure has been nondimensionalized by the freestream pressure. The dotted lines represent the results for the waveriders without the inclusion of viscous interaction effects. These were generated following the procedure outlined in step 2 of section 2.3. Note that in both figures, the pressure distributions along the upper surface are simply equal to unity. This is because when the viscous interaction is not included the upper surface is simply a freestream surface. Shown as solid lines are the pressure distributions obtained by including the viscous interaction effect as outlined in step 3 of section 2.3. In comparing the two different Mach numbers, it can readily be seen that the pressure is a factor of two times larger at the higher Mach number. This is because the shock waves as well as the viscous interaction is stronger at the higher Mach number. Also, in comparing the upper and lower surfaces, the pressure is higher on the bottom because the flow has been compressed as it passes through the shock wave which is attached along the leading edge.

Figures C.28 – C.31 illustrate the various waveriders which are generated by both including and excluding the viscous interaction effect in the generation

47

of the waverider. In Figures C.28 and 6.29 waveriders are shown but without and with this interaction for the case of Mach number 15, 50 kilometers altitude and a cone angle of 5.4 degrees. Note that the geometry seems to be similar but quantitative information regarding the geometric and aerodynamic parameters is given in Table B.2. Similarly Figure C.30 and C.31 illustrate the waveriders for the second case of Mach number 25. The altitude again is 50 kilometers however the cone angle is 5 degrees. Again, quantitative information regarding these waveriders is given in Table B.3. It was found that the difference between the waverider shapes at a given flight condition and cone angle became more significant at higher Mach numbers. For example, the waverider volume difference for Mach 25 was 10% compared to an 8% difference at Mach 15. This of course follows logically because the viscous interactions are stronger for the higher Mach number.

The optimized L/D of the waveriders, as well as the lift and drag coefficients are plotted versus Mach number in Figures C.32 through C.34. In Figure C.32, the optimized values of L/D are plotted. In general, there was a reduction in L/D when viscous interaction was considered. The highest reduction was found to be 10% at Mach 25 which was 2% higher than the reduction at Mach 15. At a Mach number of six, where there was negligible viscous interaction, no reduction in L/D was present. In Figure C.33, a small increase is shown in the lift coefficient when viscous interaction was included. However, the largest difference between the lift coefficients in the Mach range considered is 2%. In Figure C.35, we find that although the drag coefficient decreases with increasing Mach number, the value

48

of the drag coefficient at a given Mach number is higher when viscous interaction is included and this increment in C_D increases with increasing Mach number. Quantitatively, there is a 0% increment at Mach number 6 and this increases to 23% at Mach number 25. The increase in drag coefficient for the waverider which includes viscous interaction can be traced to the physical characteristics of the viscous interaction effects. Thus, the reduction of the L/D ratio is due mainly to an increase in the drag associated with the viscous interaction phenomena.

The breakdown of the drag coefficient in terms of the pressure and skin friction drag coefficients is shown in Figures C.35 and 6.19. Calculations of the skin friction drag coefficient were performed using the equation (2.17) for the case in which included the viscous interaction. For the case which it was not taken into account, the reference temperature method was used. These methods, however are considered to be equivalent. In figure 6.18, the wave drag coefficient is consistently higher when viscous interaction is accounted for. This is true even at Mach number 6 where the interaction is weak. In Figure C.36, the skin friction coefficient is lower for the case with the viscous interaction for Mach number 6 and Mach number 10. At the higher Mach numbers, however, the skin friction drag is once again higher relative to the case with no viscous interaction.

6.3.2 Results of Viscous Interaction Effects at an Altitude 60 km

The second set of results presented are for waveriders generated for Mach number 6, 10,15,20, and 25 at 60 kilometers altitude. Detailed results are presented for

Mach 15 and Mach 25. In Figures C.37 and C.38, distributions of $\overline{\chi}$ versus the length of the waverider are given for Mach 15 and 25 respectively. The values of $\overline{\chi}$ are calculated for both the upper and lower surfaces along streamline #1, the streamline directly down the center of the waverider. As found in the lower altitude case, the values for $\overline{\chi}$ on the upper surface are twice as high for the Mach number 25 case as that for Mach 15. Also, as was found earlier for the 50 kilometer altitude case, the bottom surface has lower $\overline{\chi}$ values since the Mach number has decreased and the density has increased as the flow passes through the attached shock wave. According to the White's [37] analysis the lower surface results for both Mach numbers should typify the characteristics of weak viscous interaction except near the leading edge.

Figures C.39 and C.40 illustrate the top and bottom nondimensionalized pressure distribution for Mach number 15 and Mach number 25 at 60 kilometers. As in the previous section, the solid lines represent the pressure distribution on the top and bottom surface of the waveriders generated with the inclusion of viscous interaction. The squares denote actual data points. These pressure distributions agree with flat plate trends given in Figure C.1. Quantitatively, the pressure distributions are two times larger in Figure C.40 for Mach number 25 than in Figure C.39 for Mach number 15. This follows logically since both the viscous interaction and the shock waves are stronger for Mach number 25. The pressure along the bottom is also larger than on the top because of the higher pressure on the bottom due to the flow passing through the shock.

Figures C.41 through C.44 show the geometry of the waveriders developed

for Mach 15 and Mach 25. In Figures C.41 and C.42, waveriders without and with viscous interaction are presented for Mach 15. These are generated with a cone angle of 6.5 degrees. The geometric and aerodynamic parameters for these vehicles are presented in Table B.4. Likewise, in Figures C.43 and C.44, the same comparison is made for waveriders at Mach 25 generated with the same cone angle as above. Detailed geometric and aerodynamic data is available in Table B.5. In general, inclusion of the viscous interaction phenomena smooths the leading edge. In both cases, the waveriders designed with viscous interaction had reduced planform area and volumetric efficiency. These reductions became greater as the Mach number increased.

In Figures C.45 through C.49 various aerodynamic characteristics are compared over the full range of Mach numbers studied for waveriders which include viscous interaction versus the baseline viscous optimized waverider. In Figure C.45, the lift to drag ratio is plotted. Note that the reduction in L/D due to the interaction is 10% for Mach 25 and that this percent reduction decreases for the lower Mach number. Note also that at the higher altitude, viscous interaction effects are more heavily present at Mach 6 then they were at the 50 kilometer altitude of the previous section. This Mach 6, 60 km flight condition corresponds to the border between the viscous interaction region of the Mach number–altitude map of Figure C.23.

In Figure C.46, the lift coefficient, C_L is plotted versus Mach number. As with the previous 50 km altitude case, the lift coefficient is increased due to the interaction and since higher Mach numbers enhance this interaction, the

51

increments in lift coefficients increase with increasing Mach number. The total drag coefficient also increases for the viscous interaction with an increase of 3% for Mach 6 to 23% for Mach number 25. The net result is a decrease in the lift to drag ratio which is consistent with Figure C.45.

Figures C.48 and C.49 show the breakdown of the drag coefficient into pressure drag coefficient and the skin friction coefficient. In both cases, these drag coefficients are higher for the case which includes the viscous interaction. Increments in C_{Dp} range from 9% for Mach 6 to 21% for Mach 25. Roughly the same is found for the skin friction with increments range from 4% at Mach 6 through 27% at Mach 25. Again, these findings verify that the interaction becomes stronger at the higher Mach numbers. Finally, by comparison with previous altitude of 50 km. It is seem that the strength of the interaction is increasing with altitude as well.

6.3.3 Results of Viscous Interaction Effects at an Altitude 80 km

The third set of results are obtained at an altitude of 80 kilometers. This high altitude is chosen to accentuate the effects of viscous interaction. Recall that $\overline{\chi}$ is inversely proportional to the Reynolds number which decreases at the higher altitudes. In general the results presented here follow the same trends as in the previous cases. Therefore, they will not be repeated in detail. At this altitude, however, $\overline{\chi}$ is a large value at both the leading and trailing edges which suggests that the impact of the viscous interaction is much more significant. In Figures

C.50 and C.51, the values of $\overline{\chi}$ of 110 and 300 are obtained at the leading edge for each Mach number respectively. Also, at the trailing edge, where typically $\overline{\chi}$ is small, values of 4 an 12 are obtained. Again this suggests that for these cases the viscous interaction will dominate the entire length of the waverider. For this reason, the emphasis here is to briefly highlight the differences between this high altitude case and the prior relatively low altitude case.

Figures C.52 and C.53 show the nondimensional surface pressure distribution for Mach number 15 and 25. The trends at this altitude are similar to those at 50 km. However in comparing Figures C.26 and C.27 which pertain to the 50 km altitude with Figures C.52 and C.53, it is clear that the induced pressure increment is greater for the high altitude case. This is to be expected since the values of $\overline{\chi}$ along the length of vehicles is higher for this case. Also by comparison of Mach 15 with Mach 25, again it is shown that the viscous interaction is accentuated at the higher Mach numbers. At Mach number 25, the induced pressure increment at the trailing edge is four times greater than that of Mach number 15. The resulting waverider geometrics for the Mach 15, 80 kilometers design-point are shown in Figures C.54 and C.55. In Figure C.54, the baseline waverider excludes viscous interaction in the generation process is given Figure C.55 shows the for waverider generated by including the interaction process. In Table B.6 the geometric and aerodynamic characteristics are given. Similarly, in Figures C.56 and C.57, waveriders are presented for the Mach 25 case. Table B.7 presents a quantitative assessment of their characteristics. In general for the 80 kilometer waveriders, the overall shape of the waveriders was not significantly

altered by the inclusion of the viscous interaction. In Figures C.58 through C.62, the L/D ratio, lift and drag coefficients are plotted for Mach numbers ranging from 6 to 25. Overall, these plots are qualitatively similar to the previous cases and are discussed here only to emphasize the effect of the high altitude on the results.

1. Figure C.58: The distribution of L/D versus Mach number is similar to that 50 km. However, the reductions due to the viscous interactions are 8% and 16% for the Mach number 6 and the Mach number 25, respectively. — At an altitude of 50 km the reduction in L/D was 10% for Mach number 25. Thus the viscous interaction is causing a larger decrease in the L/D ratio.

2. Figure C.59: The distribution of lift coefficient shows the same trend as at the lower 50 km altitude. The effect of viscous interaction on C_L is to increase it over the baseline configuration. This increment is 2% at 50 km altitude while at 80 km, the increase is 18%. Here the viscous interaction is strongly effecting the lift coefficient.

3. Figure C.60: The drag coefficient distribution also shows the same trend as at the lower altitudes. As with the lift coefficient the viscous interaction causes an increase in C_D. This increment ranges between 14% at 50 km and 42% at 80 km at Mach number of 25. Thus this increment has increased three fold by increasing the altitude from 50 km to 80 km.

4. Figure C.61: The pressure drag coefficient shows the same qualitative variation as the total drag coefficient.

5. Figure C.62: The skin-friction drag coefficient varies similarly with C_{Df} at the 60 km altitude. The increment in C_{Df} due to the viscous interaction increases with both Mach number and altitude. There is an increment in C_{Df} at Mach 25 at 50 km. This can be contrasted to 65% increase in C_{Df} at 80 km.

The basic trend that appears for these analyses is a lowering of the maximum L/D ratio with increasing altitude due mainly to the increasing strength of the viscous interaction.

Note that the strength of the viscous interaction is a strong function of the wall temperature. This is illustrated by Figures C.63 and C.64. It is shown that higher wall temperature ratios tend to yield higher L/D values. This is expected because physically, the effect of increasing the wall temperature is to increase the boundary layer thickness δ. In turn, the velocity gradient at the wall is decreased. Since $(du/by)_w = O(U_e/\delta)$. Because the wall shear stress τ_w is proportional to the velocity gradient, then it also will decrease, thus yielding a decreased value of the skin friction. It should be noted that there is not a large gain in L/D obtained when the wall temperature ratio is increased above 0.33. Although there are decreases in skin friction due to the thicker of boundary layer, this increased thickness may yield a stronger overall viscous interaction effect which opposes the gains in decreasing skin friction.

Figures C.65 and C.66 show the L/D distribution plotted versus altitude for Mach 15 and Mach 25 respectively. As we expected, the lift to drag ratios decrease with increasing altitude because the viscous interaction becomes stronger

at the higher altitudes.

Figures C.67 through C.73 display the aerodynamic characteristics of waveriders, designed both with and without the inclusion of viscous interaction effects. These waveriders were designed for altitudes ranging from 30.0 to 80.0 km in altitude and operational Mach numbers which varied between 6.0 and 30.0. Specifically in Figures C.67 and 6.51 the L/D ratio is overlaid on a Mach number-altitude map for both the case where viscous interaction was not accounted for and for the case where it was included. The same type of comparison is available for the lift coefficient in Figures C.69 and C.70 and the drag coefficient in 6.54 and 6.55. These maps are useful for waverider design and performance analyses.

Viscous interactions can affect the design of viscous optimized hypersonic waveriders. They must be considered in the analysis and design of any hypersonic waverider which will operate within the viscous interaction flight regime. The basic trend that appears throughout these analyses is a lowering of the maximum L/D ratio with increasing altitude. The physical reason for this is the combined effects of increasing skin friction and increasing viscous interaction with the decreasing Reynolds number that accompanies an increase in altitude.

6.4 New family of Waverider

A new family of waveriders was developed by optimizing the viscous interaction waveriders at specific design points along the proposed NASP flight trajectory given in Figure C.23. The design points, denoted by squares in the same figure, were chosen to be within the viscous interaction regime. Specifically, the design

56

points used in the present study were flight Mach numbers of 14.0, 16.0, 20.0, and 25.0 with corresponding altitudes of 140,000, 175,000, and 230,000 feet. Table B.8 lists the freestream conditions for these design points as well as the wall temperature used in each analysis.

As with the previous studies, the length of the waveriders generated was fixed at 60 meters. This is typical of proposed hypersonic vehicles. Geometric constraints were placed on the waverider generation procedure as detailed in section 5.2. In particular, maximum L/D waveriders are generated by using L/D as the figure of merit in the optimization procedure. This class of waveriders is aimed at producing the best cruise configuration for hypersonic vehicles. The geometric constraints were placed on vehicle box size and the slenderness ratio.

Another parameter, the cone angle of the generating flowfield, must also be specified. This has a significant impact on the geometry and performance of hypersonic waveriders. These waveriders can be optimized for a given figure of merit and generated for a range of cone angles when the figure of merit is plotted versus cone angle is usually found which provides the best figure of merit. This was done for conditions at Mach 25 and 230,000 ft altitude. The figure of merit was the lift to drag ratio as mentioned above. The results are shown in Figure C.73 which show L/D versus cone angle Θ_c for the given class of viscous interaction optimized waveriders. This figure shows that the maximum value of Lift/Drag that is achieved at the given condition is L/D = 4.13 at a cone angle of $\Theta_c = 8.0^o$.

In summary, the viscous interaction optimized waverider is based on the

aerodynamic properties as predicted by the viscous interaction analyses described in Chapter 2. It is suspected that a further optimization can be achieved by "scooping out" the waverider surface to account for the local displacement thickness of the boundary layer. Such "scooping out" was not included here. It is interesting to point out that such "scooping out" is not possible at and near the leading edge, because δ^* is thicker than the vehicle thickness itself. This is shown in Figure C.74, where the variation of δ^* is shown as a function of distance from the leading edge for a typical case of $M_\infty = 25$ and altitude 230.000 ft.

The methodology discussed above was applied to the Mach 14.0, 140,000 feet altitude design condition. The resulting waverider which can be labeled an optimized viscous interaction waverider, is shown in Figure C.75. For comparison, Figure C.76 and Figure C.77 are given which displays waveriders generated without accounting for viscous interaction and with viscous interaction but no optimization. Notice that a major difference between the waveriders which account for the viscous interaction and the one which does not is that the pointed leading edge of the latter is smoothed in the former. Note also that for the optimized viscous interaction waverider, the cone angle of the generating flowfield is $\Theta_c = 5.7$ degrees. A detailed comparison of the geometric and aerodynamic characteristics of all three waveriders is shown in Figures C.78–C.79, and is given in Table B.9. The last column in this table gives the percentage change between the parameters for waveriders optimized with and without viscous interaction effects. It is interesting that even at these small values of $\overline{\chi}$ and resulting induced pressures, there is a significant change in shape of the waverider when it is optimized

with viscous interaction, but this change in shape only results in a 2% reduction in L/D. Figure C.78 shows the distribution of $\bar{\chi}$ against the waverider length for the optimized viscous interaction waverider. The distribution is presented for streamline #1 the streamline passing through the center of a waverider, on both the upper and lower surfaces. Figure C.79 illustrates the upper and lower surface pressure distributions for the same waverider.

Similar studies where undertaken for the second design condition of Mach 16, 140,000 ft altitude along the NASP trajectory. The resulting shape for the optimized viscous interaction waverider is given in Figure C.80. Note for this case, the optimum cone angle is slightly lower with $\Theta_c = 5.43$ degrees. For the purposes of comparison, Figures C.81 and C.82 show the shapes of waveriders which are generated when viscous interactions are not accounted for and when the viscous interactions are included but the optimization process is not invoked. In Table B.10 the comparisons in the geometric and aerodynamic characteristics are given. The format is similar to that of Table B.9. In particular the volume of the optimized viscous interaction waverider has decreased by 32% and there are also significant reductions in the area. Both the Table and the Figures show large changes in shape, however there is only a moderate decrease of 9% in the lift to drag ratio. Figure C.83 illustrates the. $\bar{\chi}$ distribution and Figure C.84 illustrates the pressure distribution for this case. As expected the $\bar{\chi}$ distribution is higher for this higher Mach number case and thus there is a larger increment in the induced pressure.

Typical results are given for Mach 20 at 175,000 feet in Figures C.85

through C.89. Detailed quantitative comparisons are given in Table B.11. Similarly results are illustrated for Mach 25 at 230,000 feet in Figures C.90 through C.94 and Table B.12. The general features of these results can be summarized for all cases in the following manner:

1. Viscous interactions tend to reduce the lift to drag ratio, but some of this loss is recovered when the waveriders are optimized for viscous interactions.

2. The percent by which the lift to drag ratio is reduced by the inclusion of viscous interaction effects, increases with Mach number and altitude. At Mach 14 the L/D reduction is 2% where as at Mach 25 there is a 21% reduction in this ratio.

3. The loss in L/D is due mainly to an increase in both pressure drag and skin-friction drag associated with the viscous interaction phenomena. The increment in C_D ranges from 7% at Mach 16 to 64% at Mach 25.

4. The viscous interaction effects are increased with increasing the Mach number and altitude.

5. When the waverider is optimized for viscous interaction, the area, volume and overall shape can change significantly.

Once again the study shows how important the viscous interaction effects can be inside this regime. Therefore we must consider the viscous interaction effects when we design the hypersonic vehicles, especially for high altitude, high Mach number applications.

60

All of the studies that were conducted in the present work were performed on the Unisys 1100 and Sun Microsystems file server. As stated earlier, 100 optimization levels are used in the optimization of a given waverider configuration. This requires approximately 15 minutes of CPU time on a Unisys 1100 and 20 minutes on a Sun station. The relatively short running time allows for a large number of parametric studies for generating the viscous interaction flight regime and new family of waveriders that are discussed in this chapter.

Chapter 7

Conclusions and Recommendations

The present results show for the first time the effects of accounting for viscous interactions in the generation of hypersonic waveriders. Also, another important contribution is the generation of a Mach number–altitude map which delineates the region of viscous interaction effects for typical hypersonic vehicles. The results of the present study illustrate a number of important conclusions regarding the effects of the viscous interaction on viscous optimized hypersonic waveriders. The results also provide useful insight as to when the viscous interaction effect should be accounted for in the design procedure. Although instructive, the conclusions of the present study suggest that further work must be done in order to improve upon the current design process as well as to gain more information about the detailed aspects of the waverider's performance.

7.1 Summary of Results

A summary of the major results discussed in the previous chapter are itemized below:

1. The region of significant viscous interaction for waveriders, 60 meters in length has been delineated on a Mach number–altitude map. By overlaying the anticipated NASP flight envelope on this map, it is shown that the waverider will undergo viscous interaction effects above a Mach number of 16 and altitude of 140,000 feet.

2. Viscous interactions tends to reduce L/D, but some of this loss is recovered when waveriders are optimized for viscous interactions.

3. The loss in L/D increases with increasing Mach number and altitude. Note that a 9% loss in L/D was found for Mach 16 and this increased to 21% for Mach number 25 case.

4. The loss in L/D is due mainly to an increase in both pressure drag and skin-friction drag associated with the viscous interaction phenomena. The increment in C_D is increased from 7% for Mach 16 case to 64% for Mach number 25 case.

5. Contour plots are generated for L/D, C_L, and C_D for cases with and without viscous interaction cases. These clearly show how viscous interaction effects are increased with increasing the Mach number and altitude, as well as provide useful information for vehicle designers.

6. A new family of waveriders were generated wherein viscous interaction effects are included within the optimization process. When the waverider is

optimized for viscous interaction, the shape can undergo significant changes.

7. The present work provides a versatile and efficient engineering design tool which allows parametric analyses of many waverider configurations.

7.2 Recommendations

In this study, the question of viscous interaction effects on hypersonic waveriders has been addressed. In order to verify the results for the viscous interaction waverider the following independent studies are suggested.

1. Experimental testing at one or more of the design conditions to confirm the prediction of aerodynamic characteristics such as the lift to drag ratio and also to examine the off- design characteristics and the stability and control of such a vehicle.

2. Computational solutions of the detailed flowfield surrounding a viscous interaction optimized waverider. This would also verify the aerodynamic characteristics predicted in this study as well as provide interesting information on the heat transfer to the vehicle.

Additionally, there are a number of studies which could be performed to advance the waverider concept. This author believes that future work should focus on detailed aerodynamic analysis of existing waverider geometries, as well as the development of the waverider concept into a total vehicle concept. Such studies are described below:

1. Studies should be made to determine the effects of other physical phenomena such as low density effects and heat transfer on waverider configurations.

2. Since the leading edge of the waveriders will have to be blunted for heat transfer purposes, the effects of a resulting entropy layer should be studied.

3. Methods for integrating propulsion systems into the waverider design process need to studied.

4. Stability and control considerations should be examined and integrated into the waverider design.

It should be noted that a number of these studies are currently under way in the hypersonics group at the University of Maryland.

Finally the author would like to suggest two improvements on the existing waverider methodology.

1. The basic waverider program which provides viscous optimized waveriders (following Corda) should be integrated with current programs which include the effects of equilibrium chemistry, viscous interaction and heat transfer. In this way the user could easily select the effects which should be accounted for in any given design.

2. The current numerical optimization scheme should be improved upon since the resulting optimized waveriders are dependent on the choice of initial simplex and only local minimums can be found.

Appendix A

Waverider Construction

A.1   Generating Flow Field Solutions

The conical flow field solution for the calorically perfect gas is generated using a standard Taylor-Maccoll formulation, as described by Anderson in Reference 4. A spherical coordinate system with coordinates (r, θ, ϕ) is used for this solution as shown in Figure C.8.

The solution is obtained for a semi-infinite cone at zero angle of attack, producing an axisymmetric flow independent of the angle ϕ. Conical flow fields at zero angle of attack have curved streamlines within the shock layer, and constant properties along rays stemming from the vertex of the cone. Properties are therefore constant along the radial coordinate r. These two conditions are written as

$$\frac{\partial}{\partial \phi} = 0 \tag{A.1}$$

for axisymmetric flow, and

$$\frac{\partial}{\partial r} = 0 \tag{A.2}$$

for constant flow properties along rays from the vertex. The continuity equation for steady flow is

$$\vec{\nabla} \cdot (\rho \vec{V}) = 0 \tag{A.3}$$

Writing Equation (A.3) in spherical coordinates, evaluating the derivatives and applying the conditions for axisymmetric flow, this equation reduces to

$$2\rho V_r + \rho V_\theta \cot \theta + \rho \frac{\partial V_\theta}{\partial \theta} + V_\theta \frac{\partial \rho}{\partial \theta} = 0 \tag{A.4}$$

where V_r and V_θ are the velocity components in the r and θ directions, respectively.

Crocco's equation for irrotational flow is,

$$\vec{\nabla} \times \vec{V} = 0 \tag{A.5}$$

which simplifies to

$$V_\theta = \frac{\partial V_r}{\partial \theta} \tag{A.6}$$

Since the conical flow is irrotational, this equation can be used in place of the Euler's equation,

$$dp = -\rho V \, dV \tag{A.7}$$

is used as an appropriate format the momentum equation. Recognizing that the flow is isentropic, and defining a new reference velocity V_{max} such that $h_0 =$

$\frac{V_{max}^2}{2}$ these equations cascade into one ordinary differential equation which is the Taylor-Maccoll equation.

$$\frac{\gamma - 1}{2} \ \{ \ V_{max}^2 - V_r^2 - (\frac{dV_r}{d\theta})^2 [2V_r + \frac{dV_r}{d\theta}\cot\theta + \frac{d^2V_r}{d\theta^2}]\}$$
$$- \frac{dV_r}{d\theta}[V_r\frac{dV_r}{d\theta}(\frac{d^2V_r}{d\theta^2})] = 0 \qquad\qquad (A.8)$$

The only dependent variable in this equation is V_r , so the solution of this equation gives V_r as a function of θ. Once V_r is known, V_θ can be determined from Equation A.6.

Since there is no closed form analytical solution to this equation, it must be solved numerically. Defining a new variable V' as

$$V' \ \equiv \ \frac{V}{V_{max}} \qquad\qquad (A.9)$$

helps to speed up the numerical procedure. The dependent variables representing the velocities then become V_r' and V_θ'; these will be referred to in the subsequent discussion as the "working" velocities. Solving the Taylor-Maccoll equation numerically for a specific cone angle involves an inverse approach in which the shock wave angle is guessed and the cone angle that supports that shock is calculated. Once the shock angle has been assumed, the conditions immediately downstream of the shock, including V_r' and V_θ' are calculated using oblique shock relations. The equation is then numerically integrated using a fourth order Runge-Kutta method, stepping in the θ direction, from the shock wave to the body. For this solution, twenty-one rays are used within the shock layer. At each theta step,

the value of V_θ' is calculated; the θ value where V_θ' equals zero corresponds to the cone surface. Successive shock wave angles are chosen until the desired cone angle is found. Once the proper solution is achieved, the flow field variables such as pressure, temperature, and density are found using isentropic relations.

A.2 Redefinition of the Generating Flow field

Redefining the generating flow field to prepare it for the creation of a waverider consists of generating a workable grid within the shock layer, interpolating for the flow field variables between the grid points, and defining a stream function on the grid.

A.2.1 Grid Generation and Curve Fits

The conical flow algorithm produces constant values of pressure, temperature, density, and velocity on twenty-one rays emanating from the vertex of the cone. This network of rays, however, does not lend itself to the generation of a waverider shape, so a new grid must be defined within the conical shock layer.

A conical grid, which consists of the twenty-one rays from the cone flow solution and one-hundred equally spaced stations in the streamwise direction is created for the purposes of waverider generation. This grid is fitted between the shock wave and the body, as illustrated in the a sectional view is given in Figure

C.9.

This is the same grid network that has been used in previous works by Bowcutt and Corda, and has proven to be quite acceptable for waverider generation. Since the flow is axisymmetric, the grid only needs to be defined in a single plane. For simplicity, the y-z plane is chosen. Within this grid, therefore, the distance of a given point form the z-axis is denoted as y. This is identically the projection of the radial coordinate in the x-y plane.

Using the flow field variables that are now defined on this grid, it is possible to construct cubic splines vertically along each of the streamwise stations for the flow field variables. This interpolation between the grid points allows the calculation of surface conditions on the waverider once it has been generated. For example, from the cubic splines for pressure, at a given streamwise station, it is possible to get the pressure at any y-location between grid points. Cubic splines are chosen for the interpolations due to their accuracy and ease of implementation.

A.2.2 Definition of the Stream Function

During the curve fitting process, it is necessary to define a stream function vertically along each of the streamwise stations in order to trace the streamlines through the flow field. Cubic splines are then fit to the stream function values in a fashion similar to that used for the flow field variables. The stream function is defined as a function of the mass flow rate between the surface of the generating

body and a conical surface corresponding to a given point in the flow field. As a result, the stream function value becomes zero along the surface of the generating body. Defining a stream function within the conical flow field involves the integration of the local mass flow rates from the surface of the generating body, outward, toward the shock wave.

Determination of Mass Flow Rate Between Grid Points :

The elemental area used for the integration of the ith mass flow rate is depicted in Figure C.10.

The mass flow rate through this elemental area is defined as

$$\dot{m}_i = (\rho w)_i r_i dr_i d\phi \qquad (A.10)$$

where ρ is the local density, w is the local z-velocity, and r_i is the projection of r on the x-y plane. The total mass flow rate is the elemental area mass flow rate integrated over r_i and ϕ. the symbol r_{sh} denotes the radius to the shock.

$$\dot{m} = \int_0^{2\pi} \int_0^{r_{sh}} (\rho w)_i r_i dr_i d\phi \qquad (A.11)$$

Performing the outside integration, this expression becomes the following:

$$\frac{\dot{m}}{2\pi} = \int_0^{r_{sh}} (\rho w)_i r_i dr_i \qquad (A.12)$$

This expression can now be recast in terms of the working variables used in the present study. Since the projection of the radial coordinate is defined as y, r_i becomes y_i. In order to define stream function values at all of the grid points

71

within the flow field, the remaining integration is performed numerically. The integration becomes a summation in the vertical, y-direction of the grid, and the differential, dr_i, becomes the y-spacing between grid points. The expression for mass flow, therefore, becomes

$$\frac{\dot{m}}{2\pi} = \sum_{i=1}^{20}(\rho w)_i y_i (y_{i+1} - y_i) \qquad (A.13)$$

The mass flow rate between a pair of grid points corresponds to the above value determined between two indices. Now that the mass flow rates have been determined, the stream function values can be calculated.

Determination of Stream Function Values :

The stream function values generated by the code are proportional to the mass flow rate between the surface of the generating cone and the conical stream surface uniquely defined by any point within the flow field. The stream function is defined as zero on the cone surface, and as the value $(\dot{m}/2\pi)_i$ at each vertical y-location on the grid at a given streamwise z-station. This is precisely the value defined in Equation (A.13), so we let this value be the stream function at each y-location. The stream function is denoted by Ψ, and at each y-grid point $\Psi_i = (\dot{m}/2\pi)_i$ for a given z-station.

At each z-station, a cubic spline is fit to the y-coordinates versus the Ψ values, so that it becomes possible to extract a y-location for a given value of the

72

stream function, Ψ. These stream function value are the basis for tracing stream-lines through the flow field and generating the lower surface of the waverider.

A.3 Generation of a Single Waverider Geometry

In order to construct a waverider, it is first necessary to define a leading edge that is coincident with the shock wave of the generating body. Streamlines emanating from a number of discrete points on the leading edge curve are then traced through the flow field, and the resulting stream surface becomes the lower surface of the waverider. The upper surface is defined by freestream streamlines emanating from the same points along the leading edge curve. The resulting conically derived waverider is illustrated in Figure C.5, along with its generating flow field.

Note that since the upper surface of the waverider is a freestream stream surface, the flow field depicted above this surface, and the generating cone, do not exist when the waverider is actually in flight. The entire flow field above the upper surface is strictly used in the design of the vehicle, and only the flow field below the waveriders lower surface actually exists at flight conditions.

A.3.1 Definition of a Single Leading Edge

Due to the fact that the waverider is symmetrical about the y–z plane, it is only necessary to define one half of the entire leading edge. For this reason, further references to the construction and analysis of the upper and lower surfaces will

refer to only one half of the entire waverider. Each leading edge curve is defined by a projection of five points in the x-y plane, one of which is forced to lie on the y-axis and one of which is forced to lie on the shock wave. Figure C.11 depicts these points for a typical leading edge curve.

Since one point must always lie on the y-axis and one on the shock wave, these five points represent eight degrees of freedom for the definition of a single leading edge curve. Five degrees of freedom result from the y-coordinates of each of the five points, and the three remaining degrees of freedom result from the x-coordinates of the three points that are not forced to lie on the y-axis or the shock wave. The importance of the recognition of these eight degrees of freedom will become clear during the discussion of the optimization procedure.

The original five points of the leading edge are not sufficient to give enough resolution of the lower surface, since they would only allow for the tracing of five streamlines of the lower surface. In order to create a greater number of leading edge points, a cubic spline is generated to fit the original five leading edge points. Fifty-one equally spaced points are defined along the x-axis between the y-axis and the x-value of the leading edge point that lies on the shock wave. The corresponding y-values are determined by interpolation from the cubic spline. This results in fifty-one points defined along the leading edge. These fifty-one points serve as the starting points for the streamline tracing of the waverider, for a typical leading edge curve.

At this point it is important to note that an entire waverider geometry, along with all of its particular aerodynamics and resulting figure of merit, is completely defined by the choice of the five original leading edge points. Of course, if a different flight condition is used for the solution of the generating flow field, or a different generating body is chosen, the same geometric leading edge shape produces an entirely different waverider. For a single case however, the rest of the waverider analysis results from the choice of the five original leading edge points.

A.3.2 Lower Surface Construction

Once the fifty-one leading edge points are defined on the x-y plane, it is possible to begin to construct the lower surface of the waverider. The first step is to recognize that each leading edge point uniquely defines a single flow plane perpendicular to the z axis. Due to the axisymmetric nature of the generating flow field, however, the flow field solution in each flow plane is identical, and it is possible to use the same locally two dimensional flow to trace each of the streamlines. Tracing the streamlines emanating from each of the leading edge points defines the lower surface of the waverider.

Flow Planes :

A flow plane, shown in Figure C.12, is characterized by its flow plane angle, ϕ, which is simply the polar angle from the x-axis to the ray that contains a particular leading edge point. By recognition of the axisymmetric nature of the flow, it becomes evident that a streamline which originates in a particular flow plane will have its projection remain in that flow plane as it is traced through the flow field.

At this point, it should be noted that there are certain leading edge shapes that can cause more than one leading edge point to lie in the same flow plane. If this occurs, or if the polar angle to each successive leading edge point does not continually increase or decrease,then a non-realistic waverider is produced when the streamlines are traced. In order to avoid this and other violations, a number of constraints are implemented into the code. A detailed discussion of all the various constraints and violations that may occur are presented in Chapter 5.

Streamline Tracing :

Recall that values of the stream function were defined between the shock wave and the body at each of the one hundred one streamwise stations. Each flow plane, therefore, already contains information sufficient to trace streamlines. For tracing purposes, the radial distance from the z-axis to a point in a flow plane is defined as h. In order to trace a particular streamline through the flow field, a value of the stream function must first be determined immediately behind the

shock wave and then used to evaluate the y-location of that streamline at each successive downstream station.

The initial value of the stream function is determined by taking the radial distance, h, of a particular leading edge point and using that value to find the mass flow rate between the axis of the generating body and the leading edge point. The mass flow rate $(\rho w h)$, where ρ is the freestream density, and w is the freestream velocity is calculated and converted into the modified stream function as defined previously. This initial stream function value is then applied at the appropriate z–location and used to begin the tracing of a single streamline.

The radial distance, h, of a particular leading edge point uniquely defines a downstream distance, z, at which h is the exact distance between the axis of the generating body and the conical shock wave. Applying this fact, each leading edge point is defined in a cylindrical coordinate system of (h, ϕ, z). Note that this definition of z insures that each leading edge point is coincident with the shock wave. Starting from each leading edge point z-location, the previously defined initial value of the stream function is traced through the flow field.

The tracing is conducted from the shock wave, downstream, to the end of the generating body. The first data point on a single streamline coincides with the first z-station downstream of the shock wave. Using the cubic spline fit generated for determining the stream function along a z-station, a value of h is calculated which corresponds to the appropriate stream function value. This h-value is the

distance,perpendicular to the freestream, between the surface of the generating cone and the current streamline being traced. The h-value locates a point on the lower surface of the waverider at this z-station, within the current flow plane. This procedure is repeated for all of the remaining downstream z-stations within the current flow plane, and then applied to all of the fifty remaining flow planes. In this way, the lower surface of the waverider becomes completely defined in a cylindrical coordinate system.

As a note to this discussion, the exact choice of the leading edge curve influences the number of z-stations that exist for a given waverider. For example, if the centerline leading edge point is chosen to lie halfway between the shock wave and the centerline of the cone, only half of the z-stations of the generating flow field are part of the resulting waverider. If the centerline leading edge point is chosen to lie close to the vertex of the cone, however, almost all of the z-stations are part of the waverider. This is clearly illustrated in the graphical pictures of the waveriders in this paper. Each waverider graphic has the same number of cross-sections as the number of z-stations that lie downstream of the leading edge point which is forced to lie on the y-axis.

A.3.3 Upper Surface Construction

The upper surface of the waverider is much simpler to construct. This surface is defined by tracing freestream streamlines downstream from the leading

C-2

edge points. Since each leading edge point has a y-coordinate which represents that particular points vertical distance from the x-axis of the generating body, a freestream streamline is simply a streamline with this y-coordinate at each downstream z-station for the given flow plane.

The combination of the upper and lower surfaces, defined in the manner described above, completely defines a waverider shape, which stems entirely from the definition of five original leading edge points. Now that the geometry is defined, the next step is to calculate the waverider's volume and surface areas.

A.3.4 Calculation of Waverider Volume and Areas

Since the waverider geometry is now completely defined, calculation of the vehicle volume, planform area, and total surface area is possible. In order to accomplish this, the base area at each z-station, planform area, total upper surface area, and total lower surface area must be numerically integrated.

The volume of the vehicle is calculated by applying the trapezoid rule in two different stages. First, the upper and lower surface points that define the waverider are projected onto the x-y plane for each z-station (the same plane as that utilized for definition of the leading edge points). This projected cross-sectional area is then integrated using the trapezoid rule between the projected points. Note that this integration for the last z-station is the base area of the

entire vehicle. The same cross-sectional area integration is carried out for all of the z-stations that make up the waverider. The next stage involves the numerical integration of all of the calculated cross-sectional areas over the entire length of the vehicle. This is also accomplished using a trapezoid rule applied to a curve of the values of cross-sectional area versus the streamwise locations of the z-stations. In this manner, the entire volume of the vehicle is determined.

To calculate the planform area, the fifty-one leading edge points in cylindrical coordinates are first projected onto the cartesian x-z plane represented by a flow plane angle of zero degree. Using these projected points, the planform area is numerically integrated using the trapezoid rule from the nose tip toward the base of the vehicle.

The calculation of the upper and lower surface areas of the waverider is much more intensive since the surfaces are, in general, curved. This means that to keep accuracy in the integration, a large number of small panels must be chosen. In order to perform these integrations, each surface is divided into triangular panels as depicted in Figure C.13.

There are one-hundred panels between each of the z-stations of the waverider. Each surface, therefore, is divided into anywhere from two-thousand to ten-thousand panels, depending on the exact number of z-stations that make up the waverider. The areas of these triangular panels are calculated and summed

systematically from the wingtips to the centerline, and then from the nose tip to the base of the vehicle.

In order to achieve better computational efficiency, the actual calculation of the upper and lower surface areas is deferred in the code until the viscous aerodynamic force calculations are made. This is done since a detailed knowledge of the surface area panels is not needed for the inviscid aerodynamic analysis, but becomes important when the skin friction forces are integrated on both of these surfaces. It is more efficient, therefore, to calculate these areas at the same time the viscous force coefficients are being calculated.

Now that the waverider is completely defined, and its volume and areas are known, the next step is to determine the aerodynamic characteristics of the waverider.

Appendix B

Tables

Table B.1: Waverider shape comparison between without and with viscous interaction at 60Km M=6

Case	$Corda$	$Chang$	$\%difference$
$S_{plan}(m^2)$	1915.89	1886.5	1.5%
$S_{base}(m^2)$	134.22	129.18	4%
$S_{lwet}(m^2)$	1973.33	1926.2	2%
$S_{uwet}(m^2)$	1942.67	1902.1	2%
$S_{twet}(m^2)$	3916.00	3828.3	2%
$Volume(m^3)$	3256.43	2963.12	9%
V_{eff}	0.1147	0.1093	5%

$Corda$: Without viscous interaction optimum waverider
$Chang$: Non-optimized viscous interaction waverider

Table B.2: Waverider comparison between without and with viscous interaction at 50Km M=15

Case	No.Visc.	Visc.Int.	%difference
$S_{plan}(m^2)$	1256.0	1258.44	0.2%
$S_{base}(m^2)$	91.92	89.48	3%
$S_{wet}(m^2)$	2548.48	2553.3	0.2%
$Volume(m^3)$	2216.36	2069.76	7%
V_{eff}	0.1353	0.129	5%
C_L	0.0178	0.0179	+ 0.6%
C_D	0.0019	0.0021	+ 11%
L/D	9.23	8.49	8%

$No.Visc.$: Without viscous interaction optimum waverider
$Visc.Int.$: Non-optimized viscous interaction waverider

Table B.3: Waverider comparison between without and with viscous interaction at 50Km M=25

Case	No.Visc.	Visc.Int.	%difference
$S_{plan}(m^2)$	1186.43	1178.02	0.7%
$S_{base}(m^2)$	88.82	85.11	4%
$S_{wet}(m^2)$	2411.5	2390.2	0.9%
$Volume(m^3)$	2203.88	1983.23	10%
V_{eff}	0.1427	0.134	6%
C_L	0.0153	0.0156	+ 2%
C_D	0.00167	0.00191	+ 14%
L/D	9.15	8.2	10%

$No.Visc.$: Without viscous interaction optimum waverider
$Visc.Int.$: Non-optimized viscous interaction waverider

Table B.4: Waverider comparison between without and with viscous interaction at 60Km M=15

Case	$No.Visc.$	$Visc.Int.$	$\%difference$
$S_{plan}(m^2)$	1690.93	1639.48	3%
$S_{base}(m^2)$	156.45	146.07	6.6%
$S_{wet}(m^2)$	3438.48	3330.72	3.1%
$Volume(m^3)$	3937.48	3334.72	15%
V_{eff}	0.147	0.136	7.5%
C_L	0.0256	0.027	+ 5.5%
C_D	0.00358	0.00427	+ 19%
L/D	7.16	6.54	8.6%

$No.Visc.$: Without viscous interaction optimum waverider
$Visc.Int.$: Non-optimized viscous interaction waverider

Table B.5: Waverider comparison between without and with viscous interaction at 60Km M=25

Case	$No.Visc.$	$Visc.Int.$	$\%difference$
$S_{plan}(m^2)$	1412.4	1463.38	+ 3.6%
$S_{base}(m^2)$	140.49	133.61	5%
$S_{wet}(m^2)$	2878.45	2889.9	+ 0.4%
$Volume(m^3)$	3315.32	2901.65	12%
V_{eff}	0.157	0.143	9%
C_L	0.0255	0.028	+ 10%
C_D	0.00367	0.0045	+ 23%
L/D	6.96	6.23	10%

$No.Visc.$: Without viscous interaction optimum waverider
$Visc.Int.$: Non-optimized viscous interaction waverider

Table B.6: Waverider comparison between without and with viscous interaction at 80Km M=15

Case	No.Visc.	Visc.Int.	%difference
$S_{plan}(m^2)$	1654.83	1659.37	+ 0.3%
$S_{base}(m^2)$	224.8	218.7	3%
$S_{wet}(m^2)$	3438.6	3449.03	+ 0.3%
$Volume(m^3)$	5642.15	5274.2	6.5%
V_{eff}	0.192	0.1826	5%
C_L	0.0489	0.0555	+ 5%
C_D	0.0124	0.0167	+ 35%
L/D	3.93	3.33	15%

$No.Visc.$: Without viscous interaction optimum waverider
$Visc.Int.$: Non-optimized viscous interaction waverider

Table B.7: Waverider comparison between without and with viscous interaction at 80Km M=25

Case	$No.Visc.$	$Visc.Int.$	$\%difference$
$S_{plan}(m^2)$	1359.09	1359.05	0%
$S_{base}(m^2)$	194.44	188.89	3%
$S_{wet}(m^2)$	2820.5	2820.51	0%
$Volume(m^3)$	4613.54	4280.61	4%
V_{eff}	0.204	0.194	7%
C_L	0.049	0.058	+ 18%
C_D	0.0129	0.0183	+ 42%
L/D	3.79	3.17	16%

$No.Visc.$: Without viscous interaction optimum waverider
$Visc.Int.$: Non-optimized viscous interaction waverider

Table B.8: Flight condition of viscous interaction optimum waverider

Property	Mach 14	Mach 16	Mach 20	Mach 25
Length (m)	60.	60.	60.	60.
Altitude (ft*1000)	140	140	175	230
Pressure (N/m^2)	201.3	201.3	52.61	5.52
Density (Kg/m^3)	2.72E-3	2.72E-3	6.82E-4	8.75E-5
Temperature (K)	257.7	257.7	268.9	219.7
Temperature Wall(K)	1020.0	1020.0	1200.0	1500.0

Table B.9: Waverider comparison between with and without viscous interaction at 140,000Ft M=14

	$Case1$	$Case2$	New	$\%difference$
$S_{plan}(m^2)$	1452.30	1479.52	1236.50	15%
$S_{base}(m^2)$	117.15	111.46	88.69	24%
$S_{wet}(m^2)$	2951.64	3007.11	2526.05	14 %
$Volume(m^3)$	2494.30	2149.28	1843.29	26%
V_{eff}	0.127	0.113	0.122	4%
C_L	0.0216	0.0215	0.0194	10%
C_D	0.00217	0.00223	0.00198	9%
L/D	9.96	9.66	9.75	2%

$Case1$: Without viscous interaction optimum waverider
$Case2$: Non-optimized viscous interaction waverider
New : With viscous interaction optimum waverider

Table B.10: Waverider comparison between with and without viscous interaction at 140,000Ft M=16

	$Case1$	$Case2$	New	$\%difference$
$S_{plan}(m^2)$	1691.22	1697.40	1442.56	15%
$S_{base}(m^2)$	127.31	119.55	99.73	22%
$S_{wet}(m^2)$	3408.62	3421.15	2918.11	14 %
$Volume(m^3)$	2986.42	2522.04	2023.03	32%
V_{eff}	0.123	0.109	0.111	10%
C_L	0.0181	0.0181	0.0176	3%
C_D	0.00167	0.00187	0.00178	+ 7%
L/D	10.9	9.7	9.9	9%

$Case1$: Without viscous interaction optimum waverider
$Case2$: Non-optimized viscous interaction waverider
New : With viscous interaction optimum waverider

Table B.11: Waverider comparison between with and without viscous interaction at 175,000Ft M=20

	$Case1$	$Case2$	New	$\%difference$
$S_{plan}(m^2)$	909.25	903.12	664.88	27%
$S_{base}(m^2)$	66.89	65.28	48.77	27%
$S_{wet}(m^2)$	1866.22	1851.1	1381.38	26 %
$Volume(m^3)$	1647.7	1552.41	1116.18	28%
V_{eff}	0.153	0.148	0.162	+ 6%
C_L	0.0156	0.0161	0.0163	+ 4%
C_D	0.00193	0.00240	0.00243	+ 25%
L/D	8.1	6.7	6.7	17%

$Case1$: Without viscous interaction optimum waverider
$Case2$: Non-optimized viscous interaction waverider
New : With viscous interaction optimum waverider

Table B.12: Waverider comparison between with and without viscous interaction at 230,000Ft Mach=25

	$Case1$	$case2$	New	$\%difference$
$S_{plan}(m^2)$	1467.82	1364.22	1194.8	19%
$S_{base}(m^2)$	184.82	166.13	145.3	21%
$S_{wet}(m^2)$	3026.89	2861.41	2480.56	18 %
$Volume(m^3)$	4578.38	4081.07	3230.20	29%
V_{eff}	0.188	0.187	0.183	3%
C_L	0.034	0.043	0.044	+ 29%
C_D	0.00644	0.0107	0.0106	+ 64%
L/D	5.26	4.07	4.13	21%

$Case1$: Without viscous interaction optimum waverider
$Case2$: Non-optimized viscous interaction waverider
New : With viscous interaction optimum waverider

Appendix C

Figures

(a) Inviscid flow

(b) Viscous flow
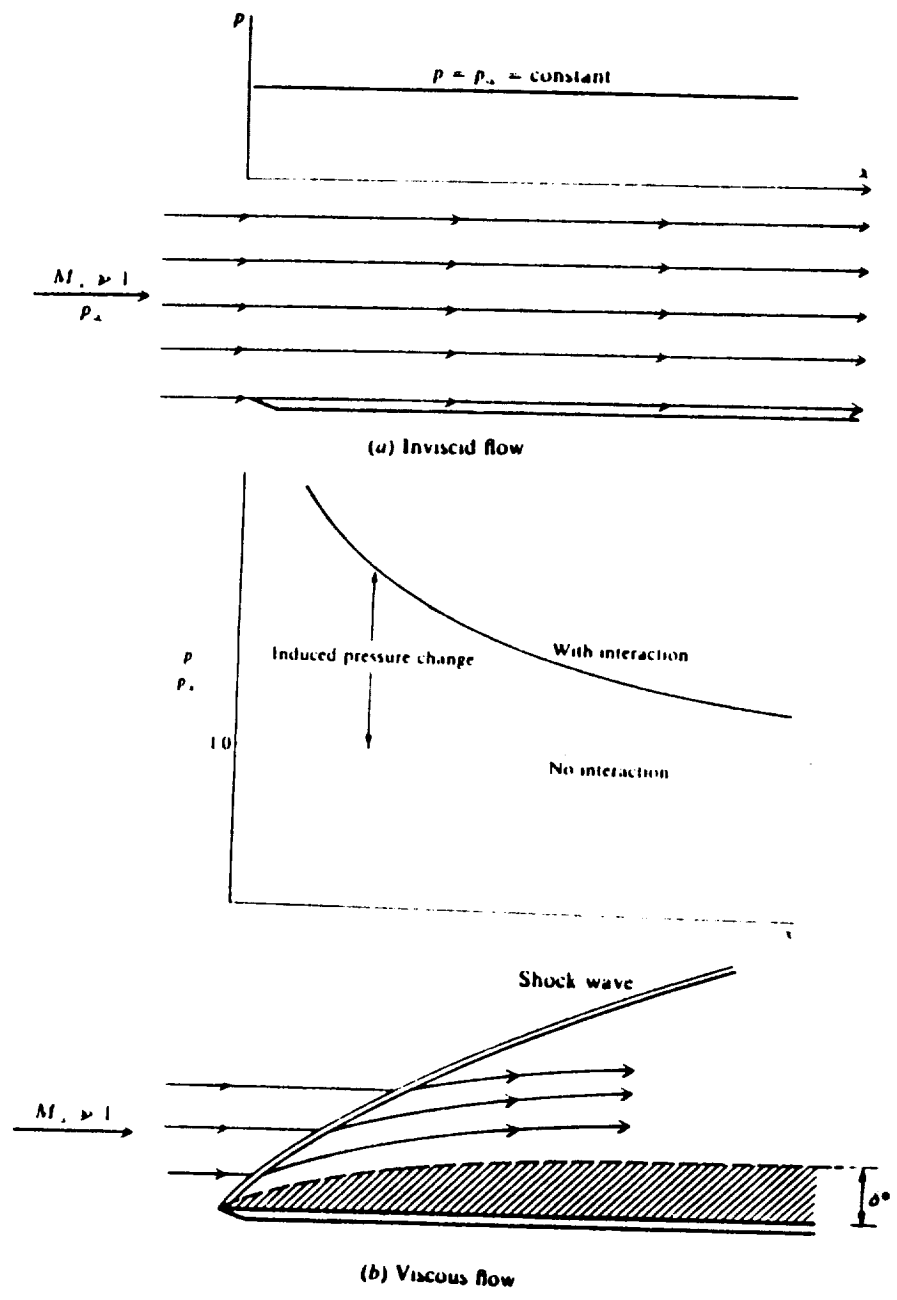
Figure C.1: Illustration of pressure distributions over a flat plate[4]
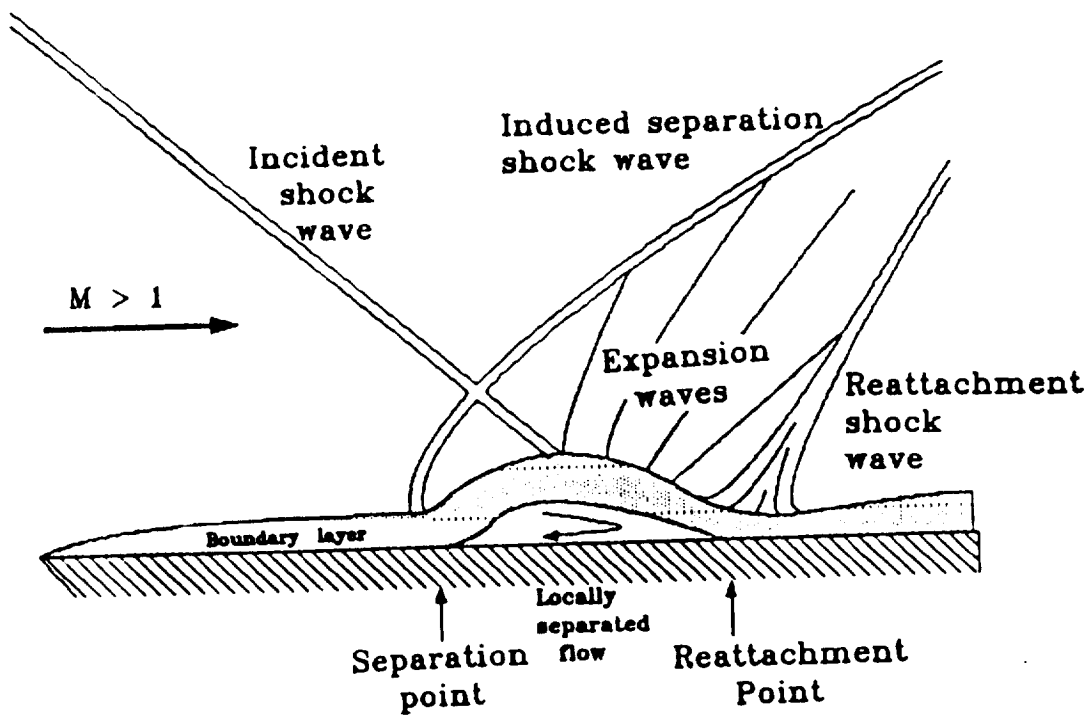
Figure C.2: Schematic of the shock-wave / boundary-layer interaction
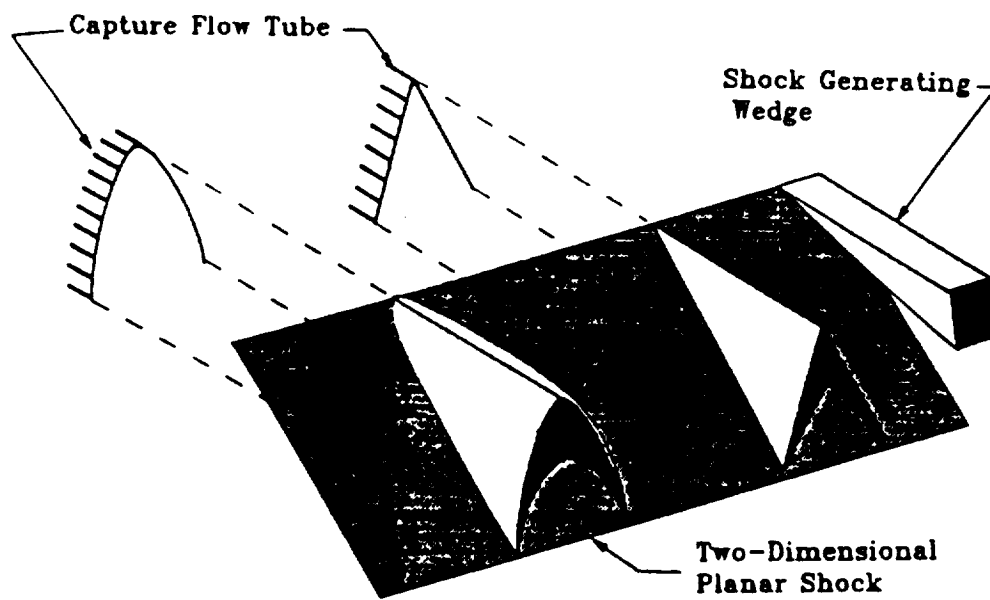
Figure C.3: Derivation of waveriders from a two-dimensional planar flow field
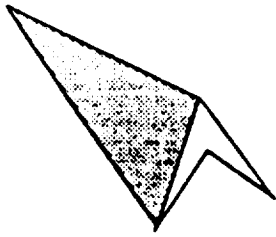
Caret
(Nonweiler)
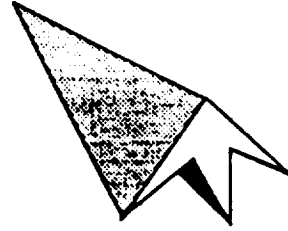
W—Delta
(Nonweiler)
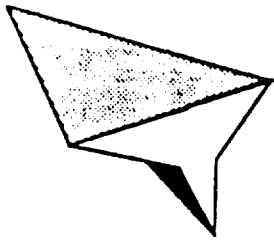
T—Delta
(Flower)
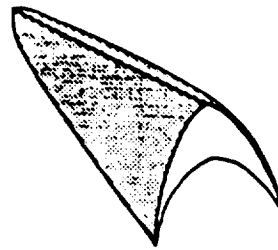
Concave
(Woods)
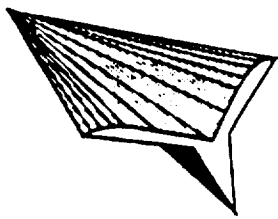
Y—Delta
(Flower)
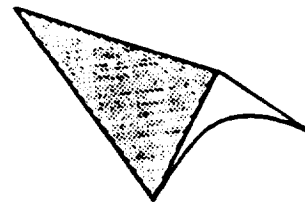
Caret—Isentropic
Compression(Townend)

Figure C.4: Waverider concepts derived from two-dimensional planar shocks
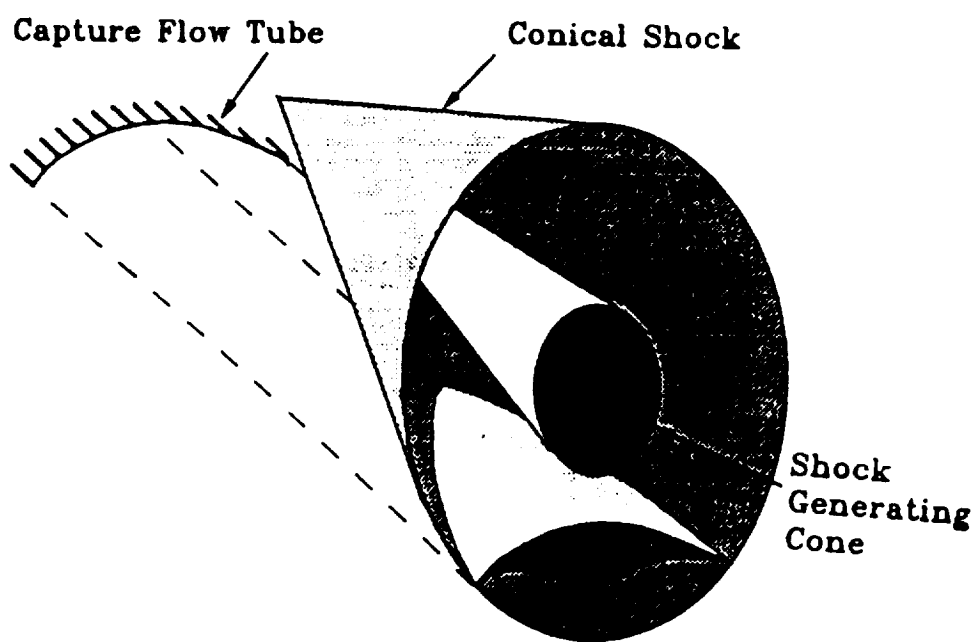
Figure C.5: Waverider from a conical flow field
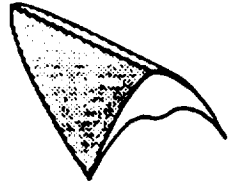
Axisymmetric Body
Inviscid (Jones)
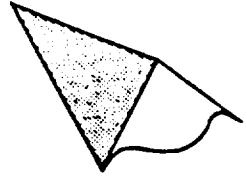
Cone−Derived
Inviscid(Rasmussen)
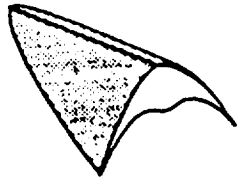
Cone−Derived
(Bowcutt)
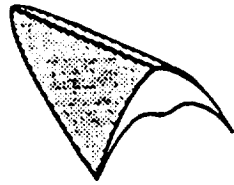
Axisymmetric Body
(Corda)
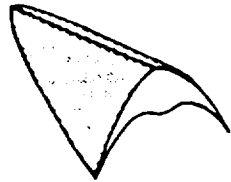
Chemical Equil. Flow
Cone (McLaughlin)
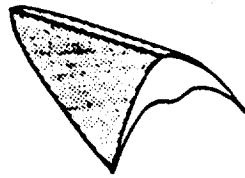
Arbitrary Shock
(Sobieczky)

Figure C.6: Waverider concepts derived from axisymmetric or arbitrary shocks
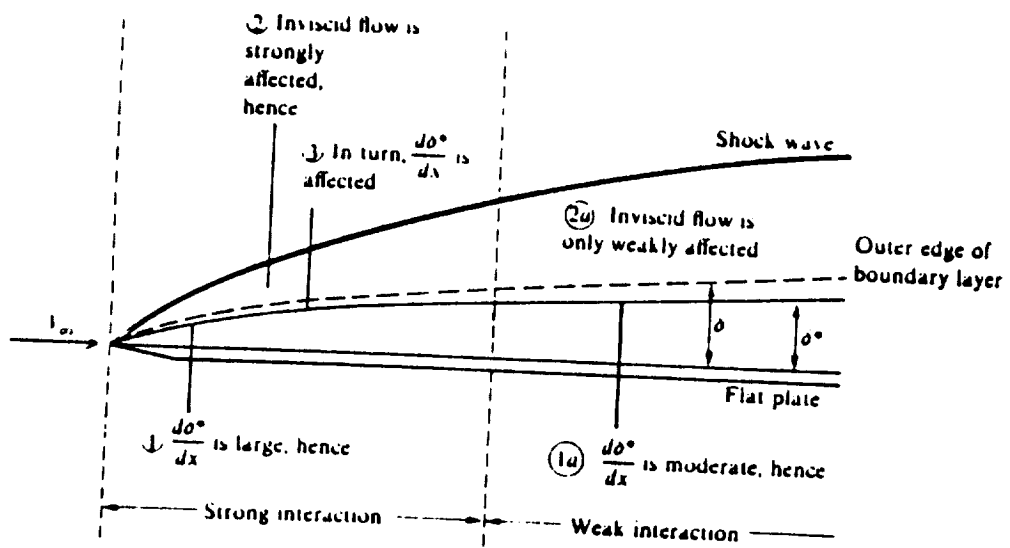
Figure C.7: Illustration of strong and weak viscous interaction[4]
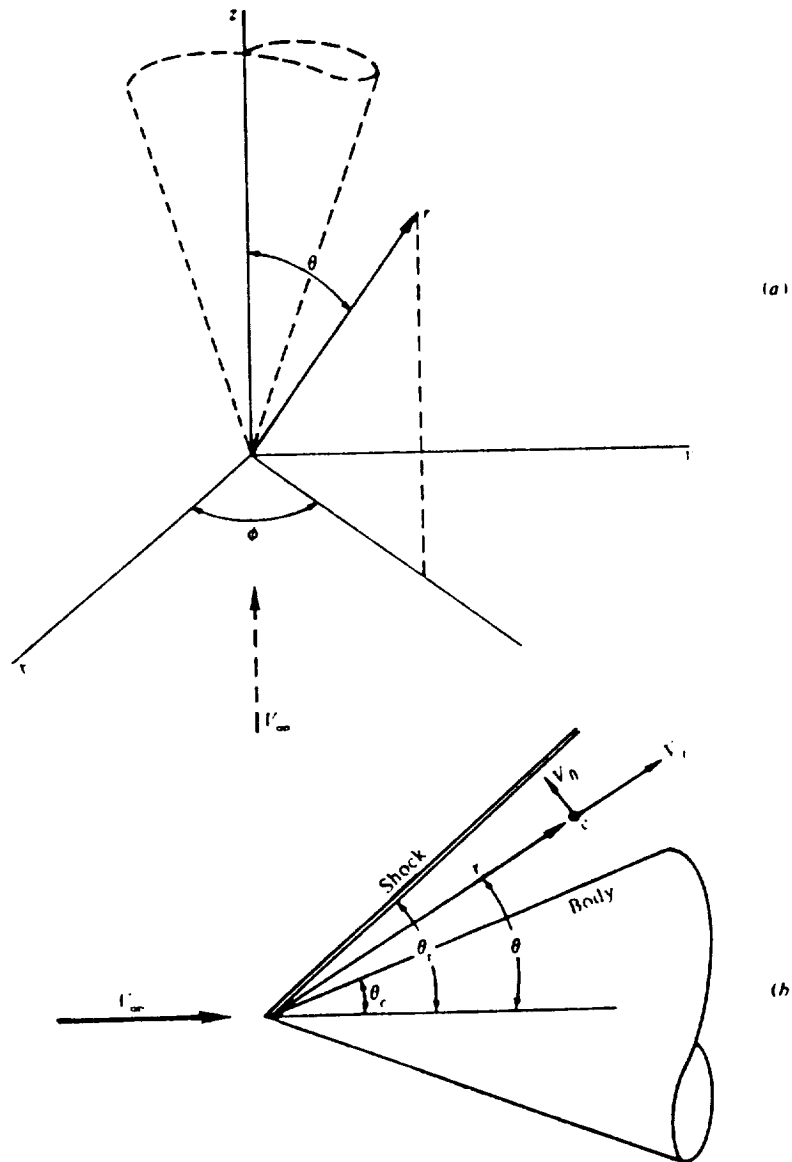
Figure C.8: A spherical coordinate system for cone
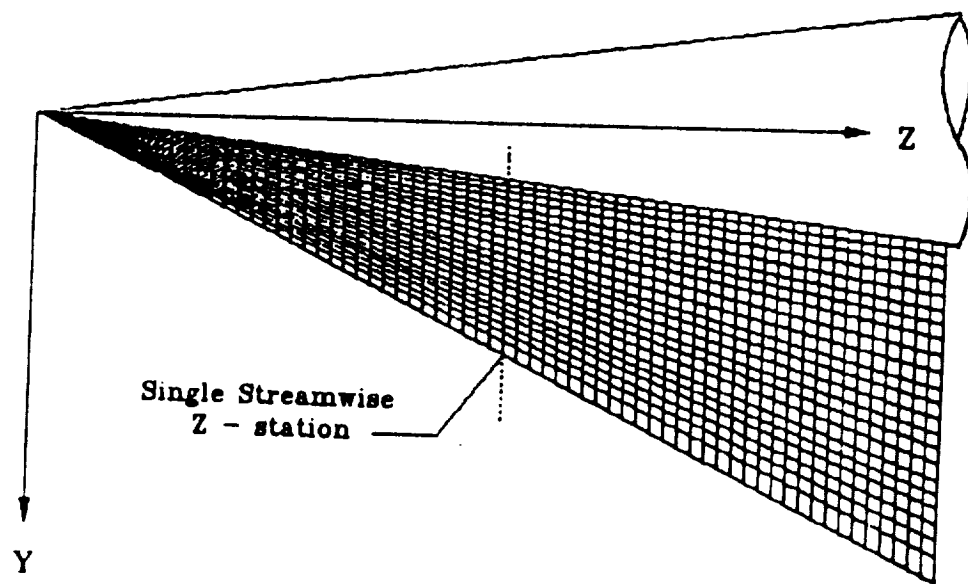
Figure C.9: Section of conical grid fitted between shock wave and cone
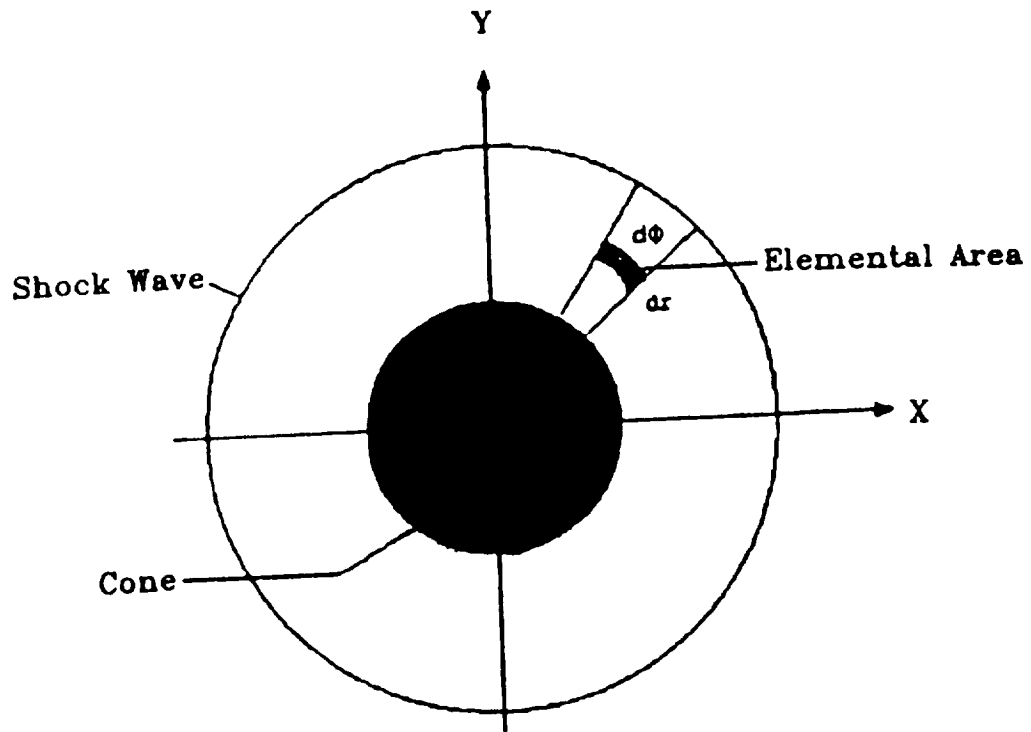
Figure C.10: Elemental area used for integration of mass flow rate
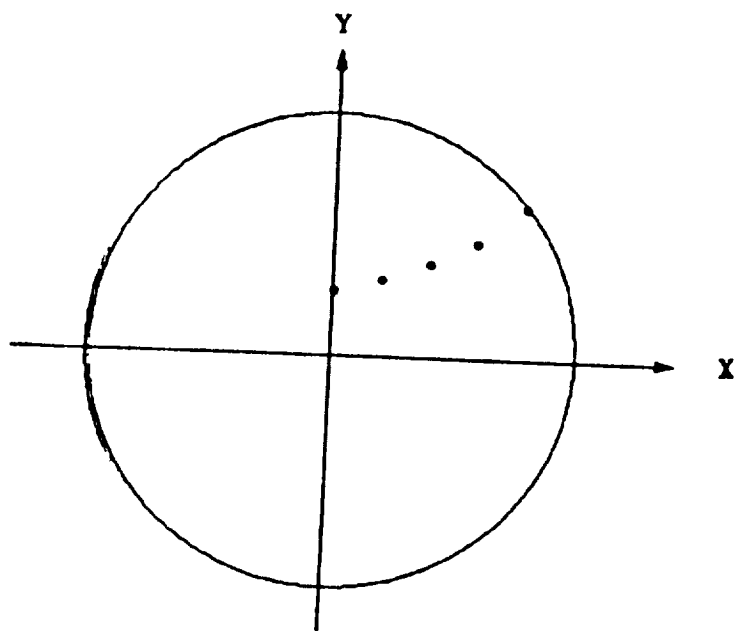
Figure C.11: Illustration of five original leading edge points
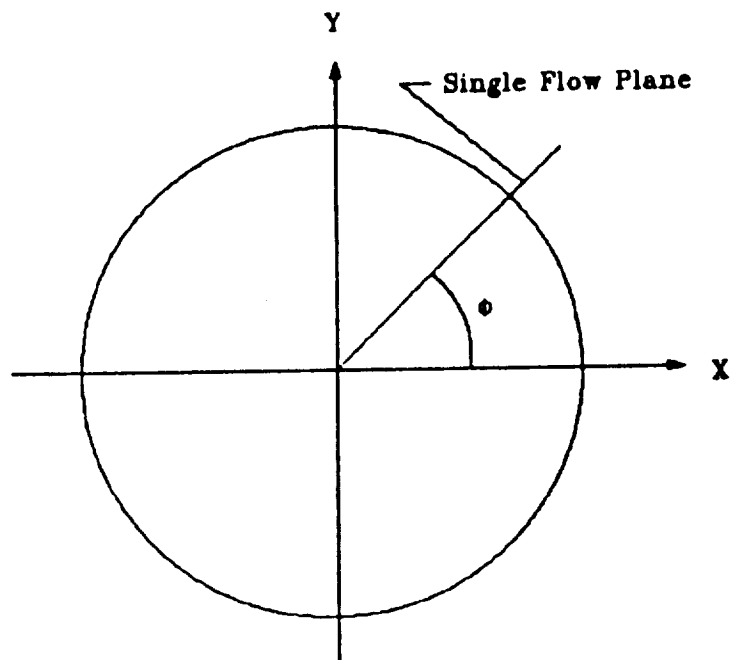
Figure C.12: Definition of flow plane
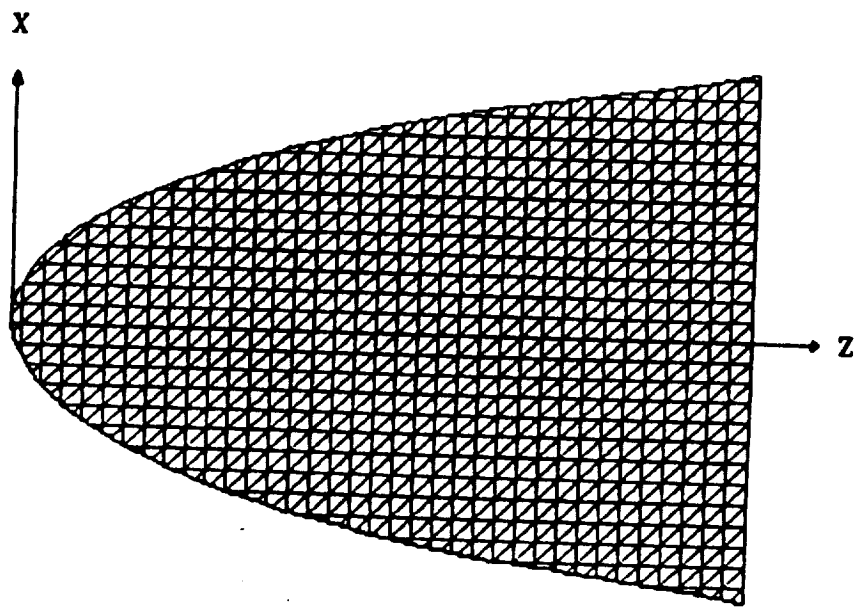
Figure C.13: Triangular panels for surface area integration
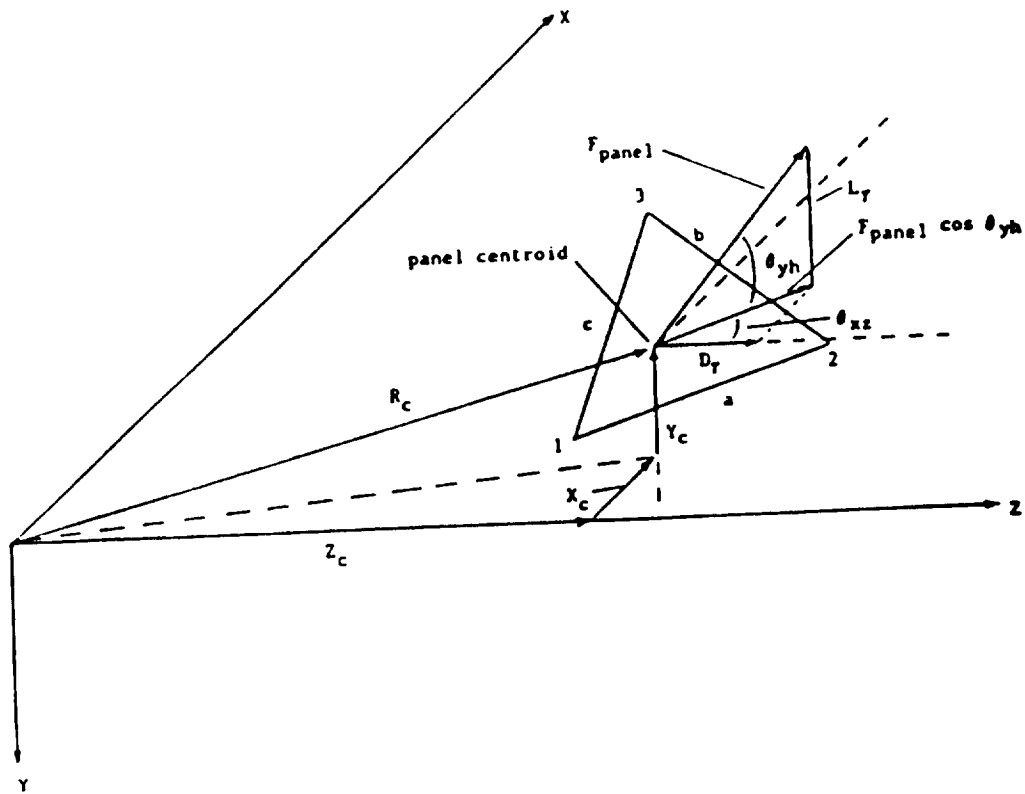
Figure C.14: Nomenclature for a single panel
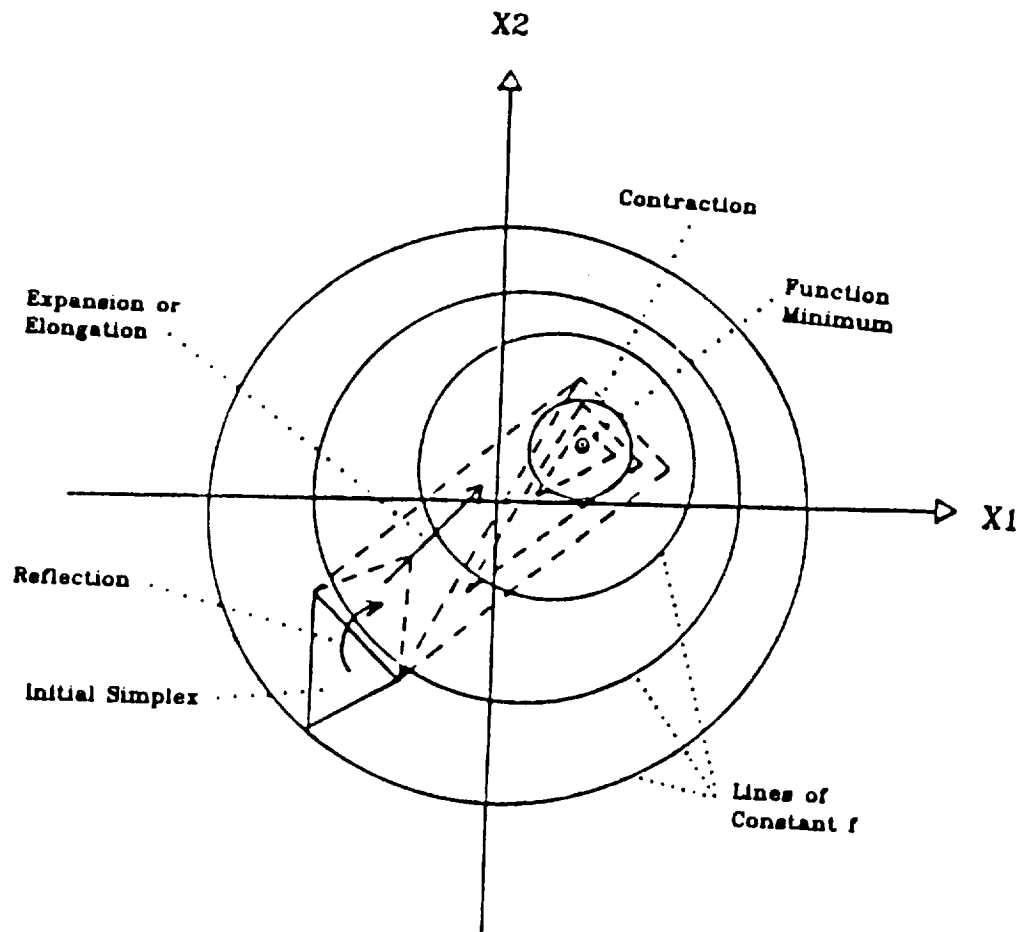
Figure C.15: Example of the simplex method using two variables

Mach Number=6, Altitude=110,000 ft.

Aircraft Length(l)=60 m, Re_l=7.73x10^7
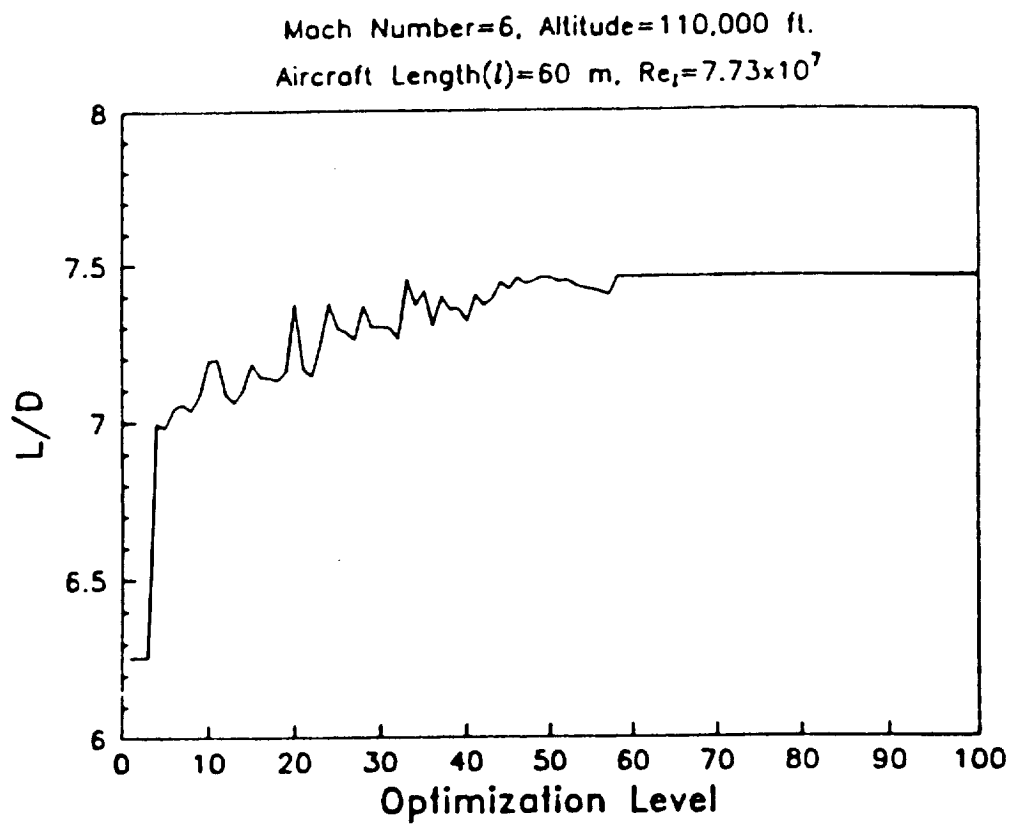
Figure C.16: Typical optimization history
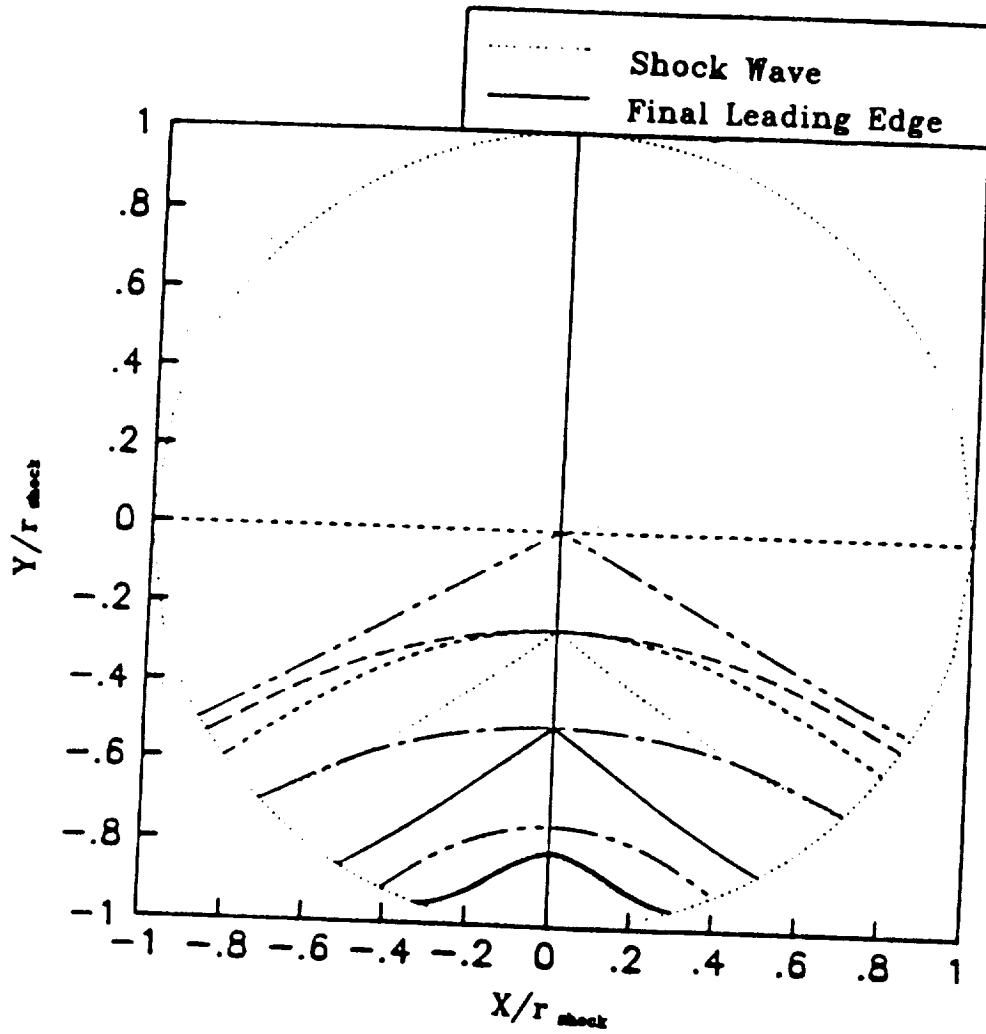
Figure C.17: Basis(initial) and final leading edge curves
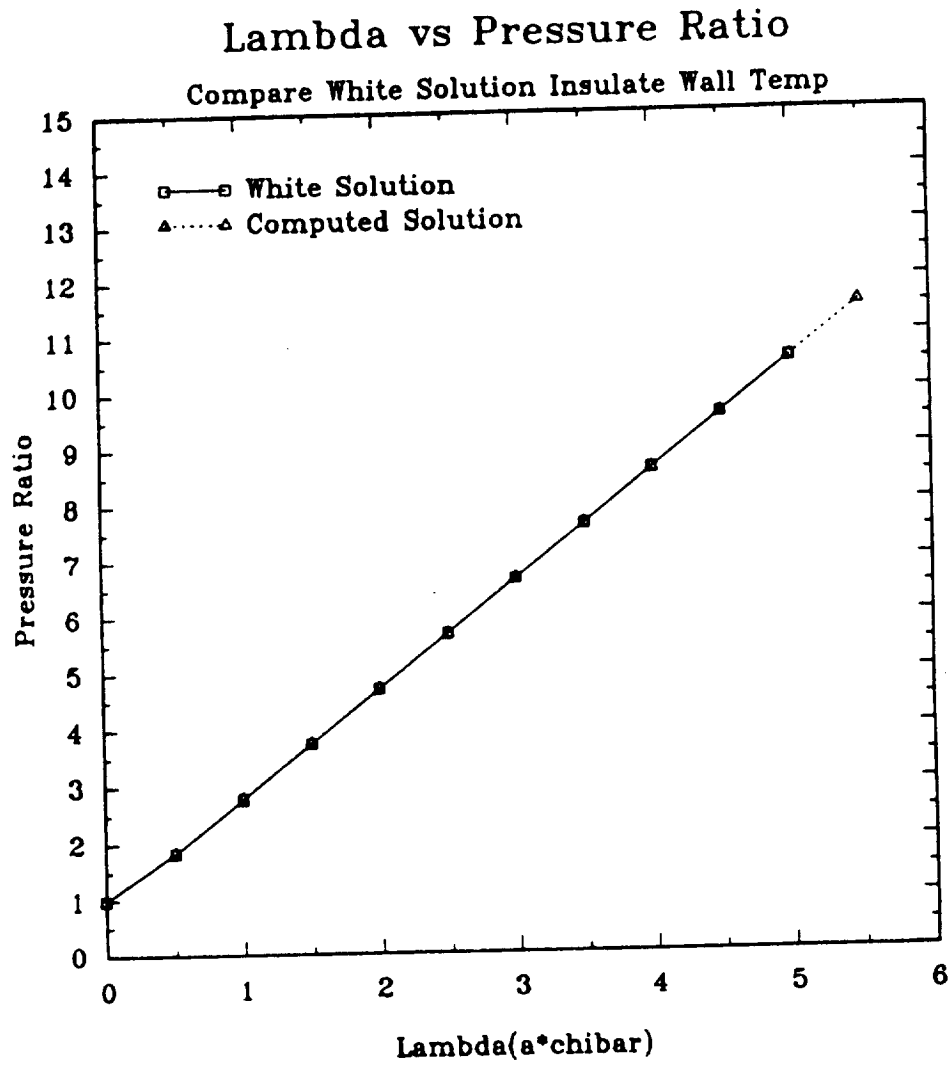
Figure C.18: Comparison of viscous interaction results on flat plate with Λ

Figure C.19: Comparison of viscous interaction results on flat plate with $\bar{\chi}$

Compare Flat–Plate Solution(cold wall)

Mach=6, Alt=60Km Bertram vs Hayes
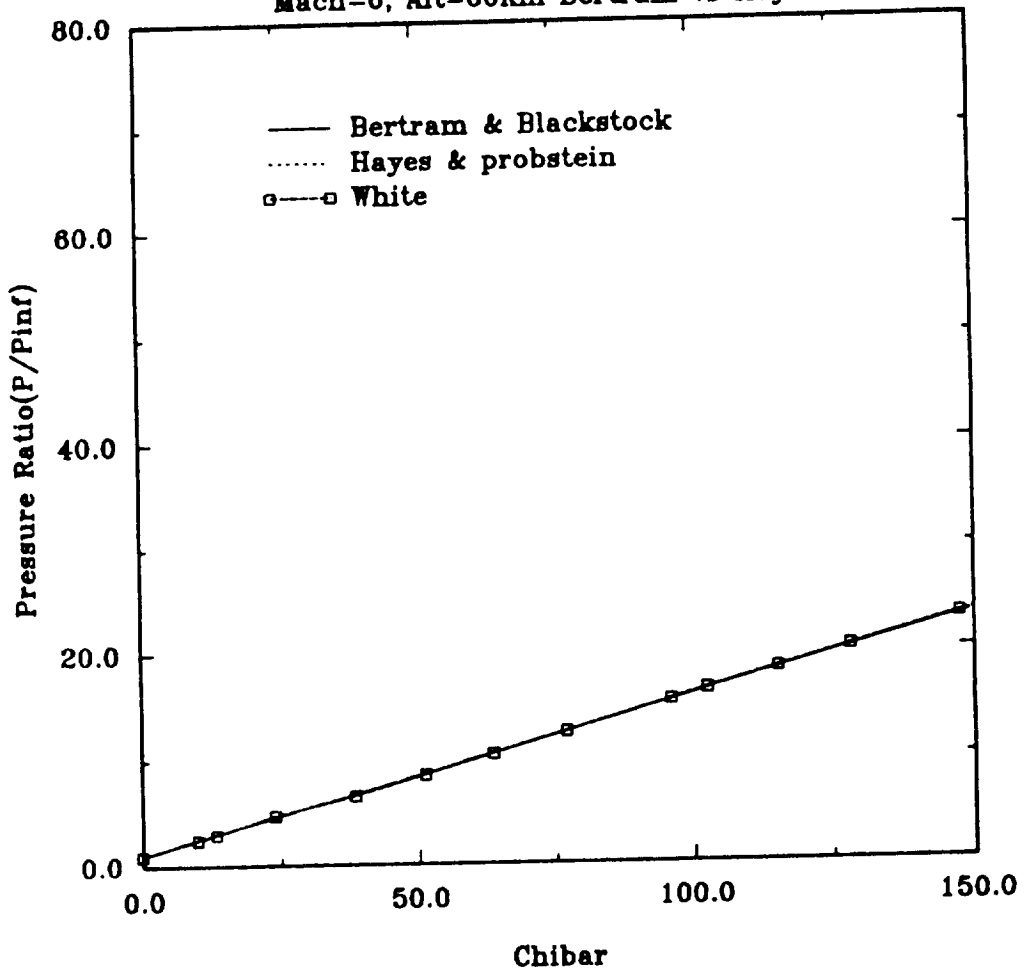
Figure C.20: Comparison of viscous interaction results(cold wall case)
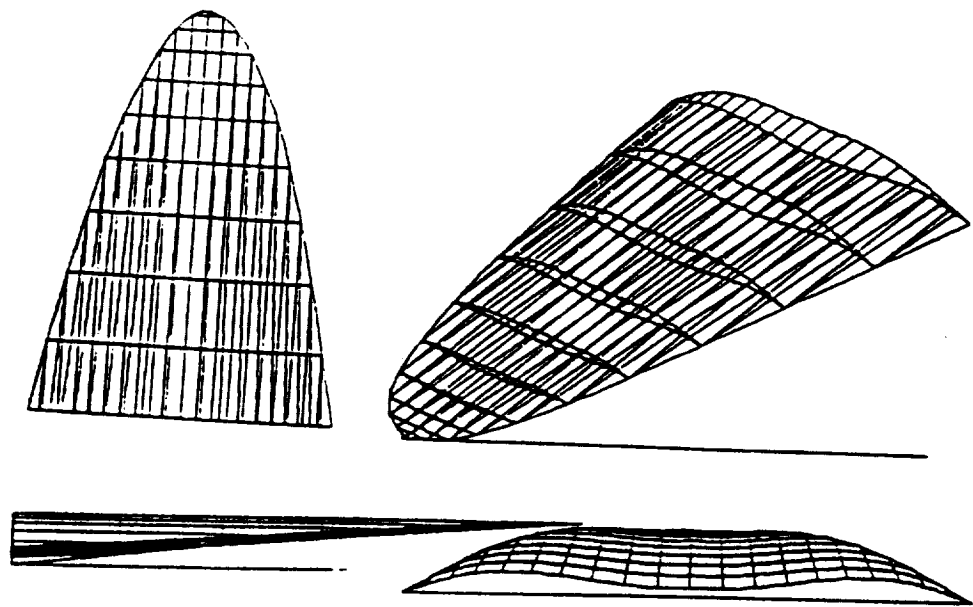
Figure C.21: Without viscous interaction waverider H=60km, M=6
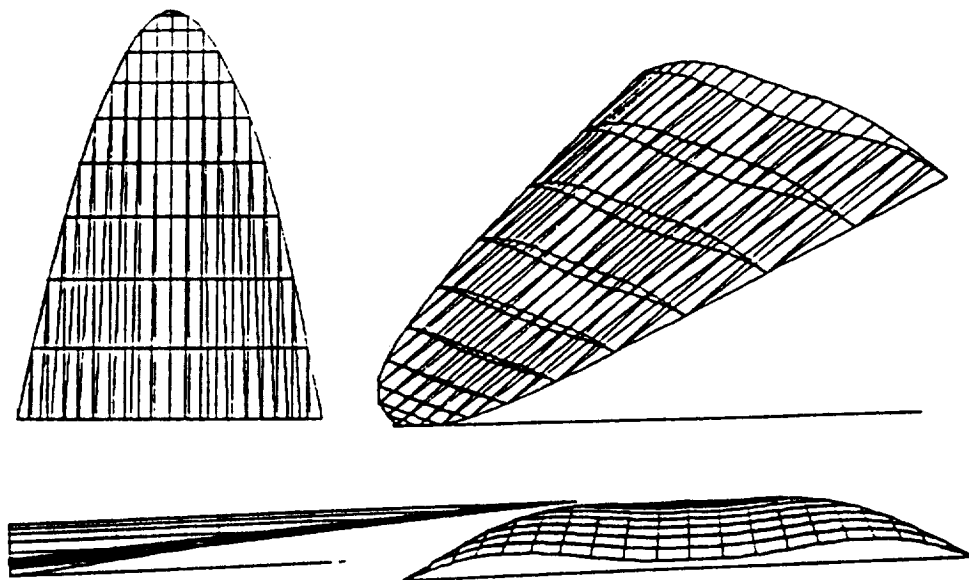
Figure C.22: With viscous interaction nonoptimized waverider H=60km, M=6
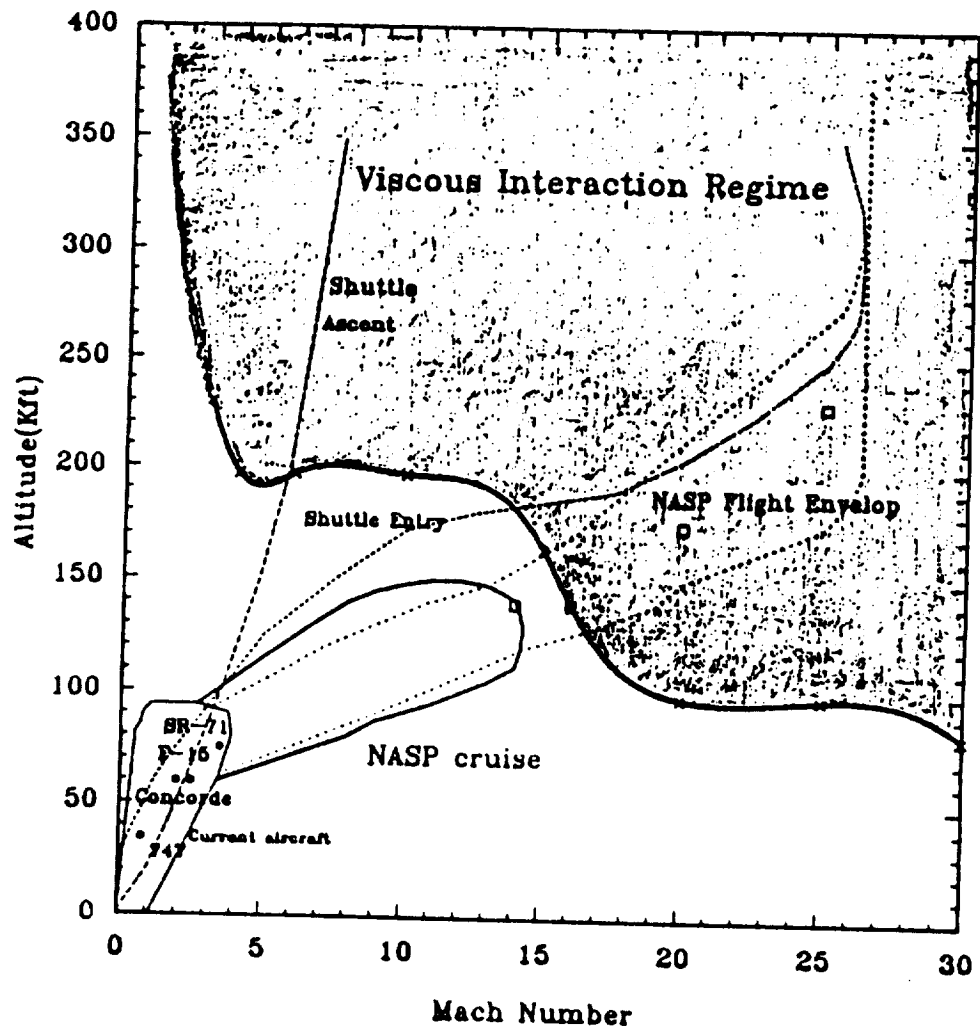
Figure C.23: Flight envelope and viscous interaction flight regime

Figure C.24: $\bar{\chi}$ distribution on waverider H=50km, M=15

Figure C.25: $\overline{\chi}$ distribution on waverider H=50km, M=25

Pressure Distribution on Waverider

Alt=50 Km, Mach=15 Stream line # 1
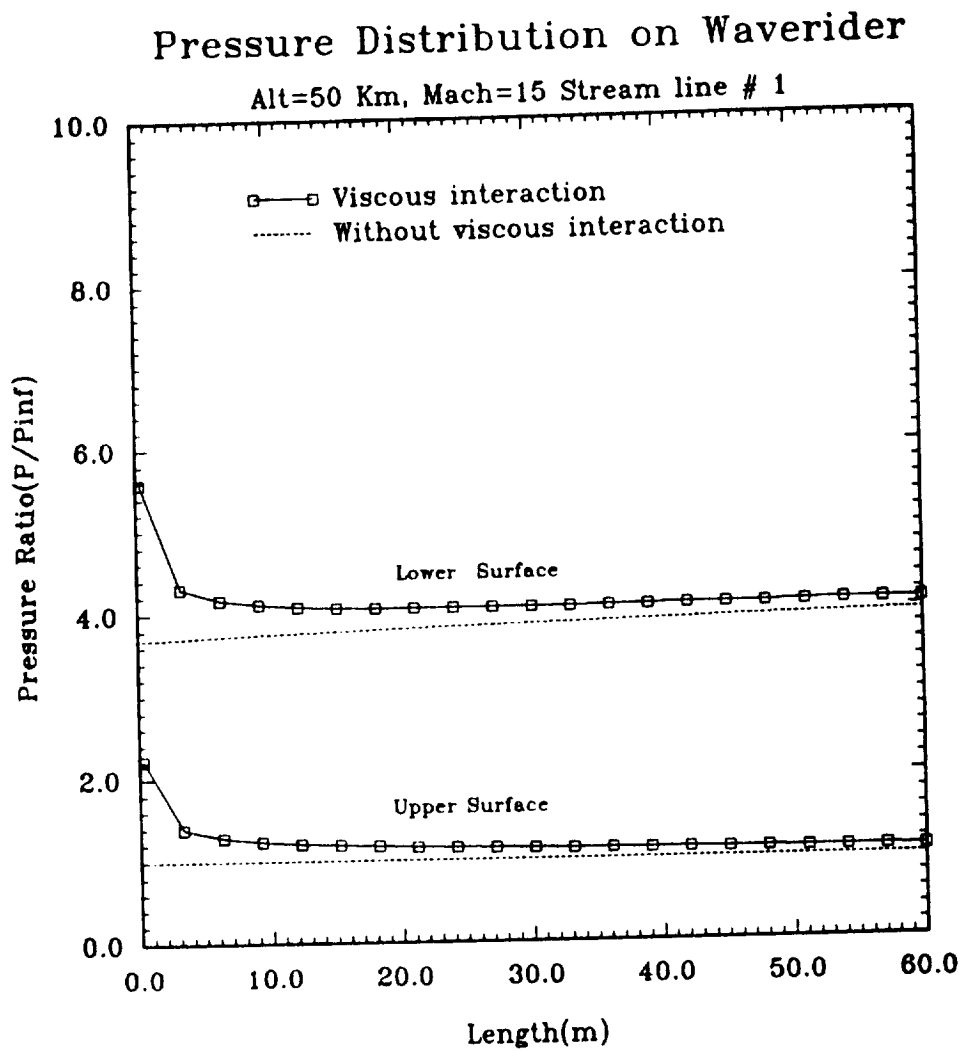
Figure C.26: Pressure ratio distribution on waverider H=50km, M=15
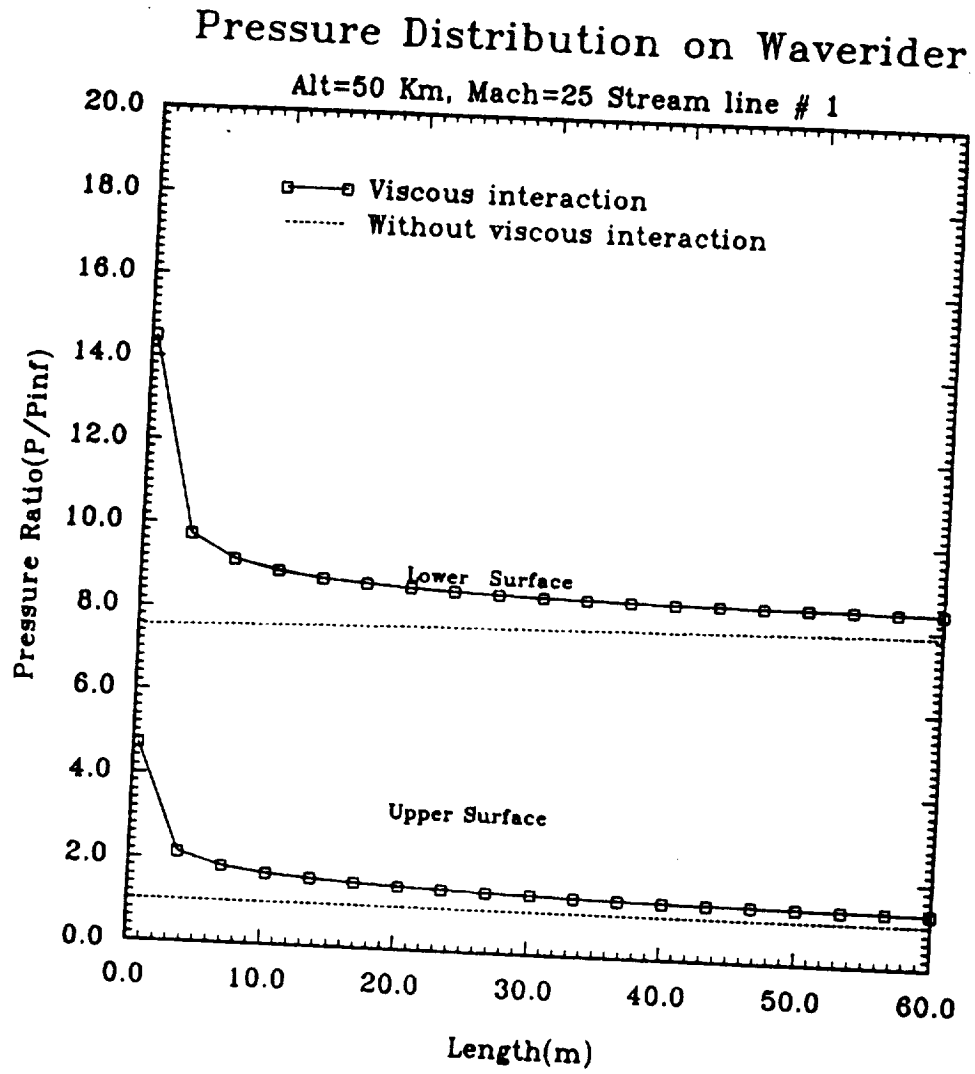
Figure C.27: Pressure ratio distribution on waverider H=50km, M=25
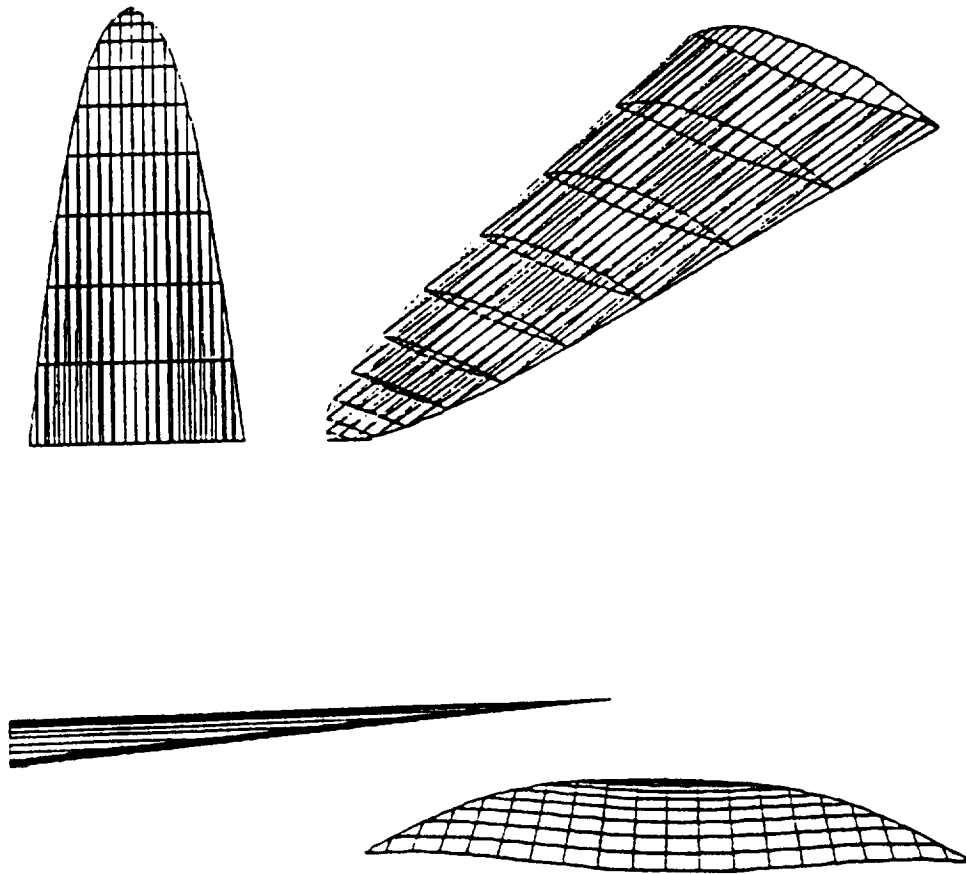
Figure C.28: Without viscous interaction waverider H=50km M=15 θ=5.4
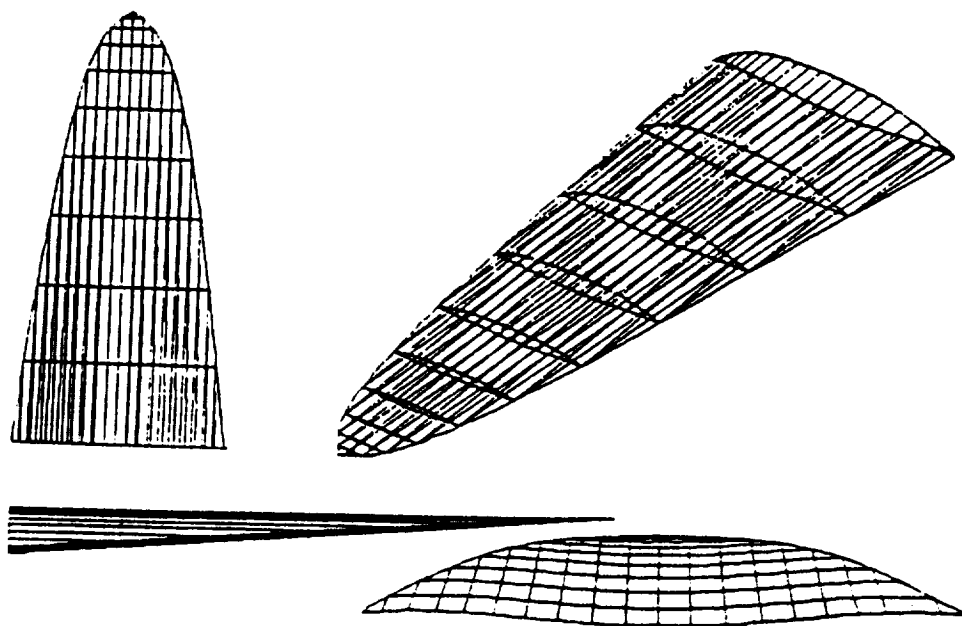
Figure C.29: Nonoptimized viscous interaction waverider H=50km M=15 θ=5.4
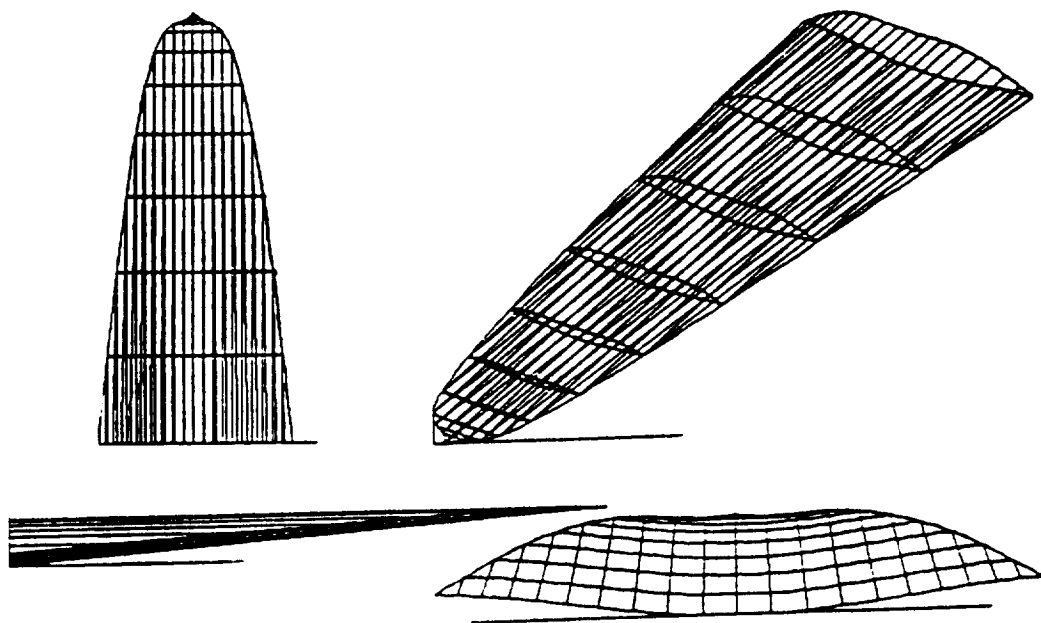
Figure C.30: Without viscous interaction waverider H=50km M=25 θ=5
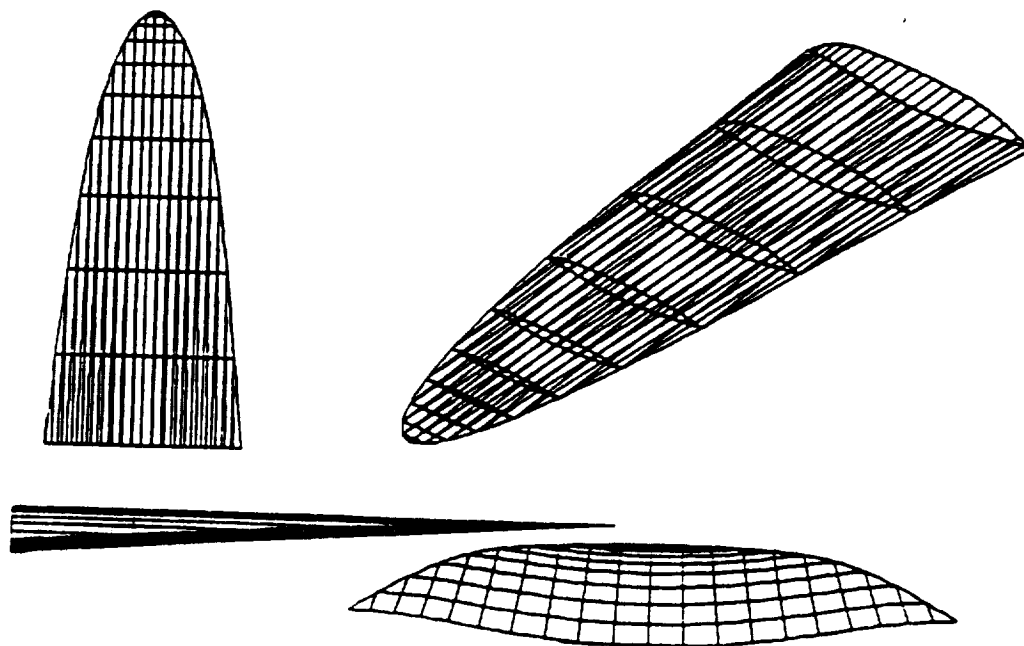
Figure C.31: Nonoptimized viscous interaction waverider H=50km M=25 θ=5

L/D vs Mach No. at Alt=50 Km
Tw/Tad=0.33
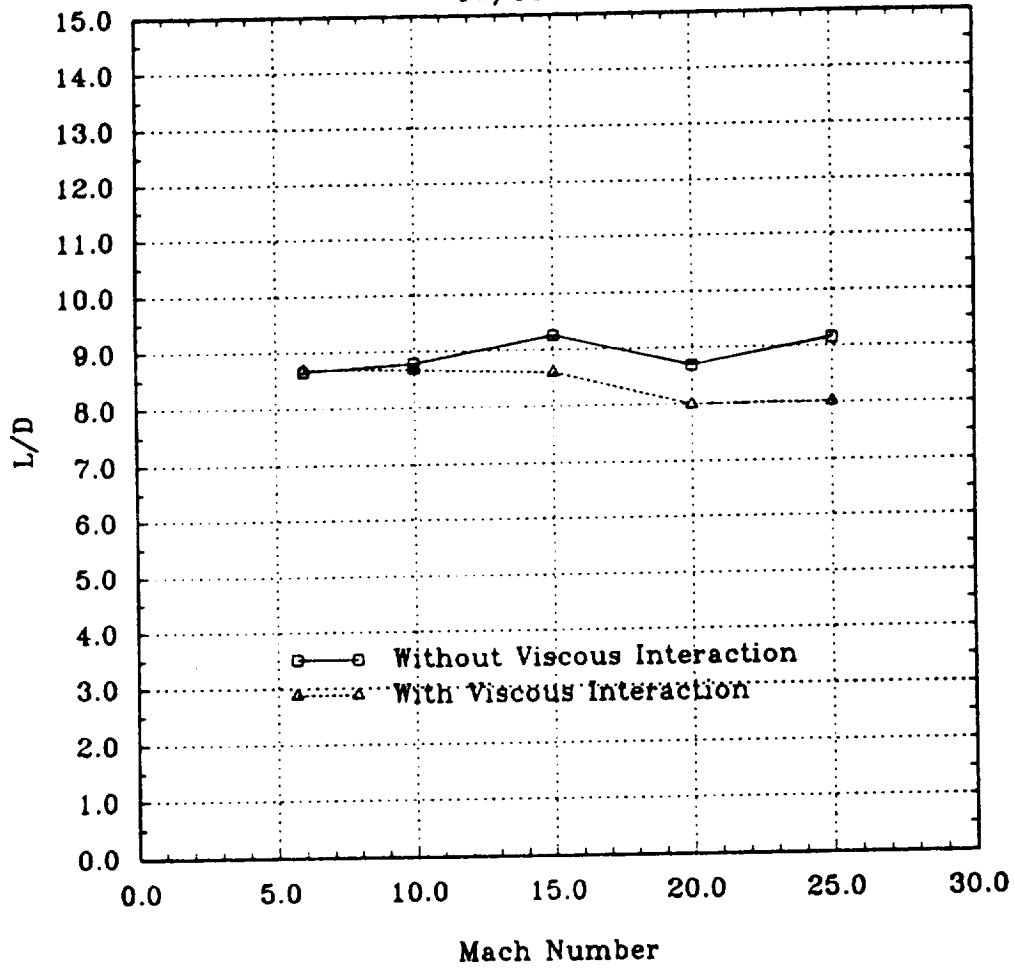
Figure C.32: Lift/Drag distribution on waverider at H=50km
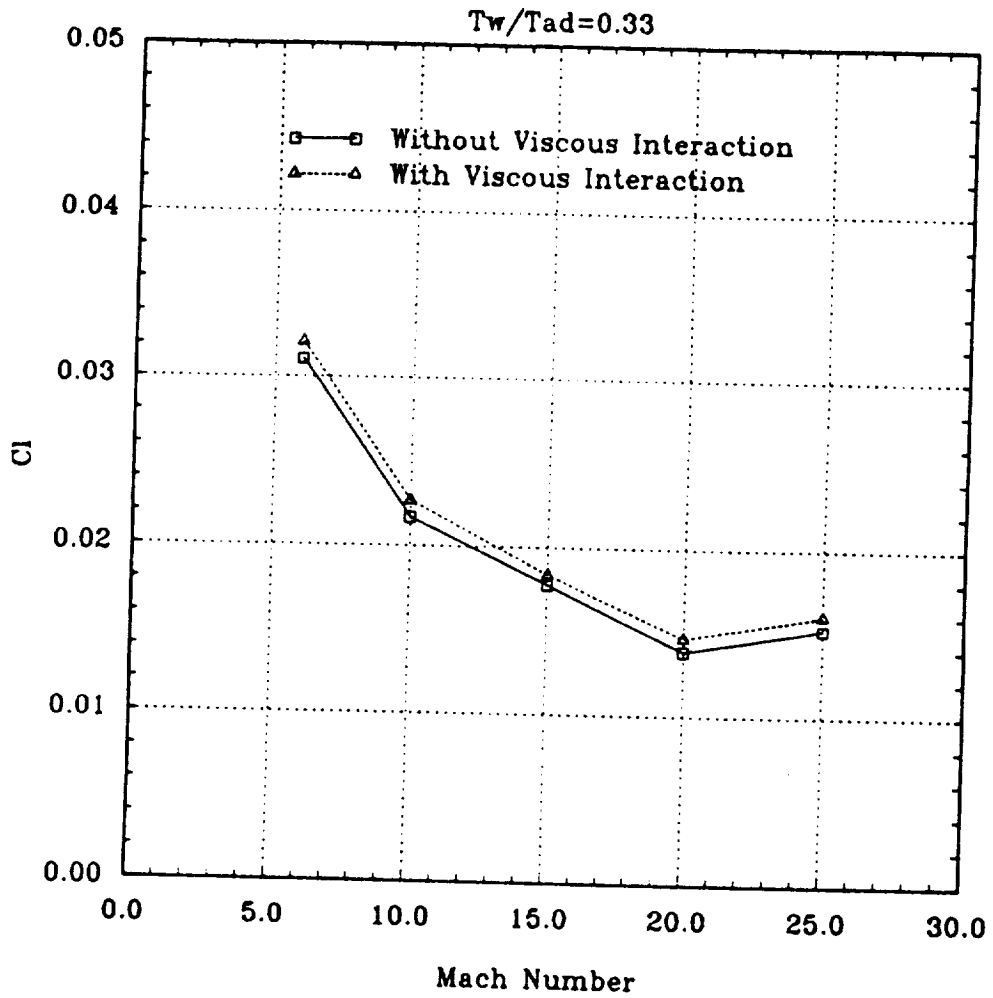
Figure C.33: Lift coefficient distribution on waverider at H=50km

Cd vs Mach No. at Alt=50 Km

Tw/Tad=0.33
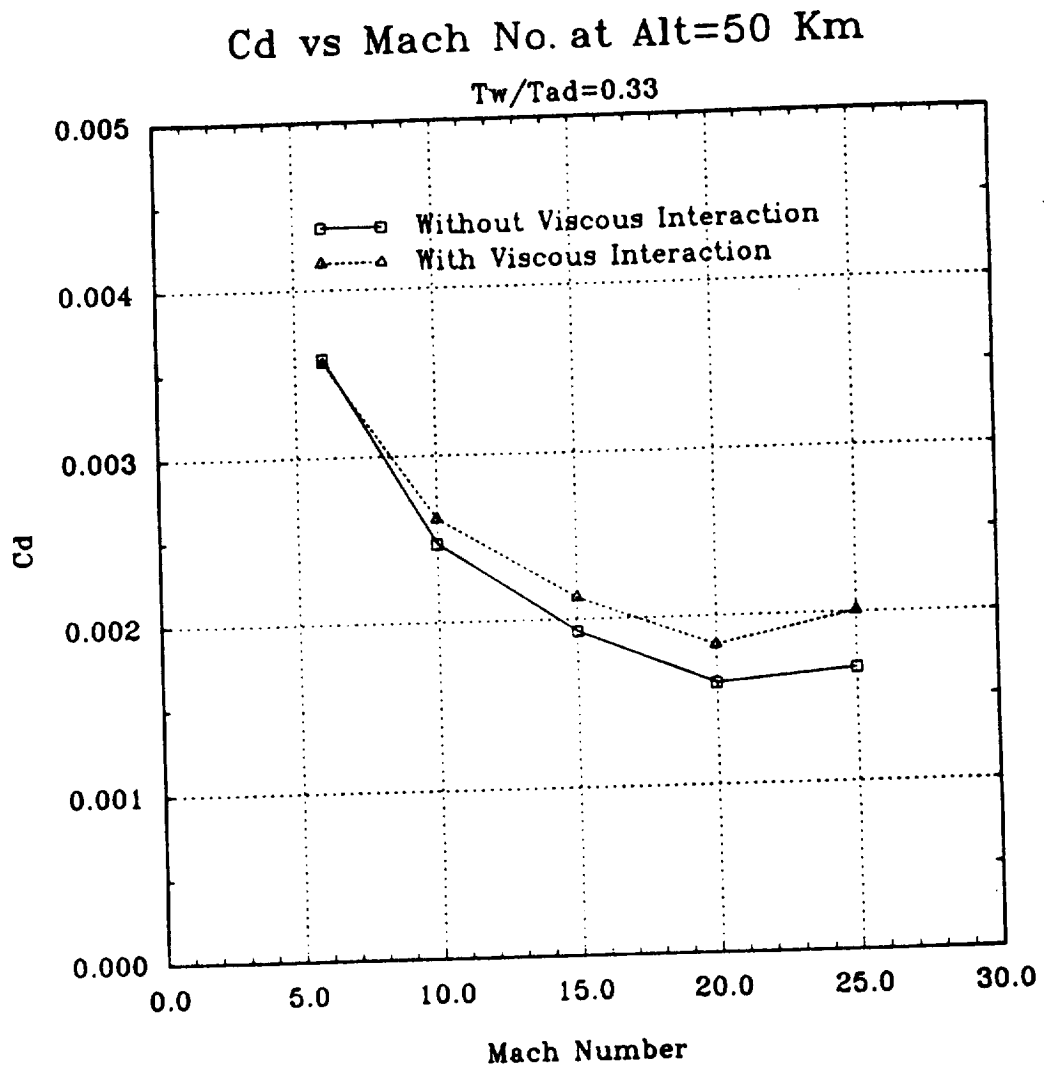
Figure C.34: Drag coefficient distribution on waverider at H=50km
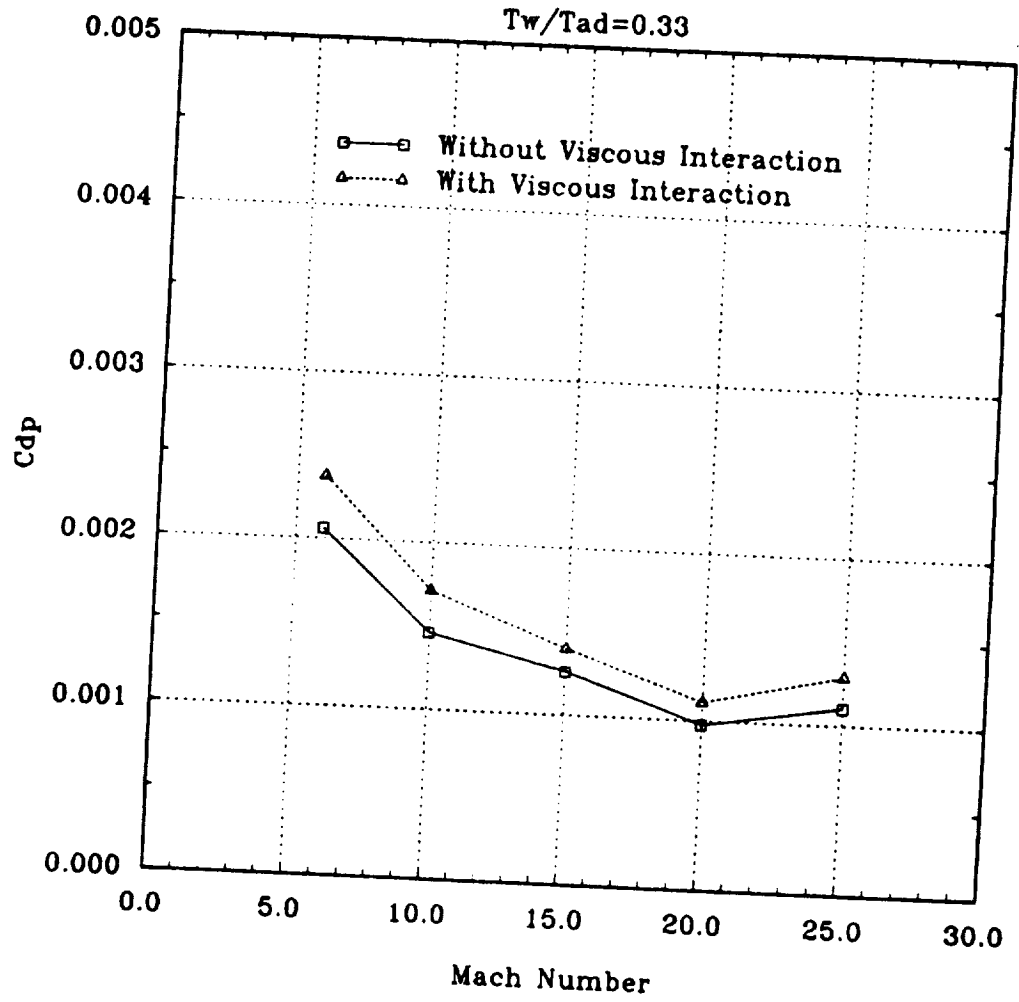
Figure C.35: C_{Dp} distribution on waverider at H=50km
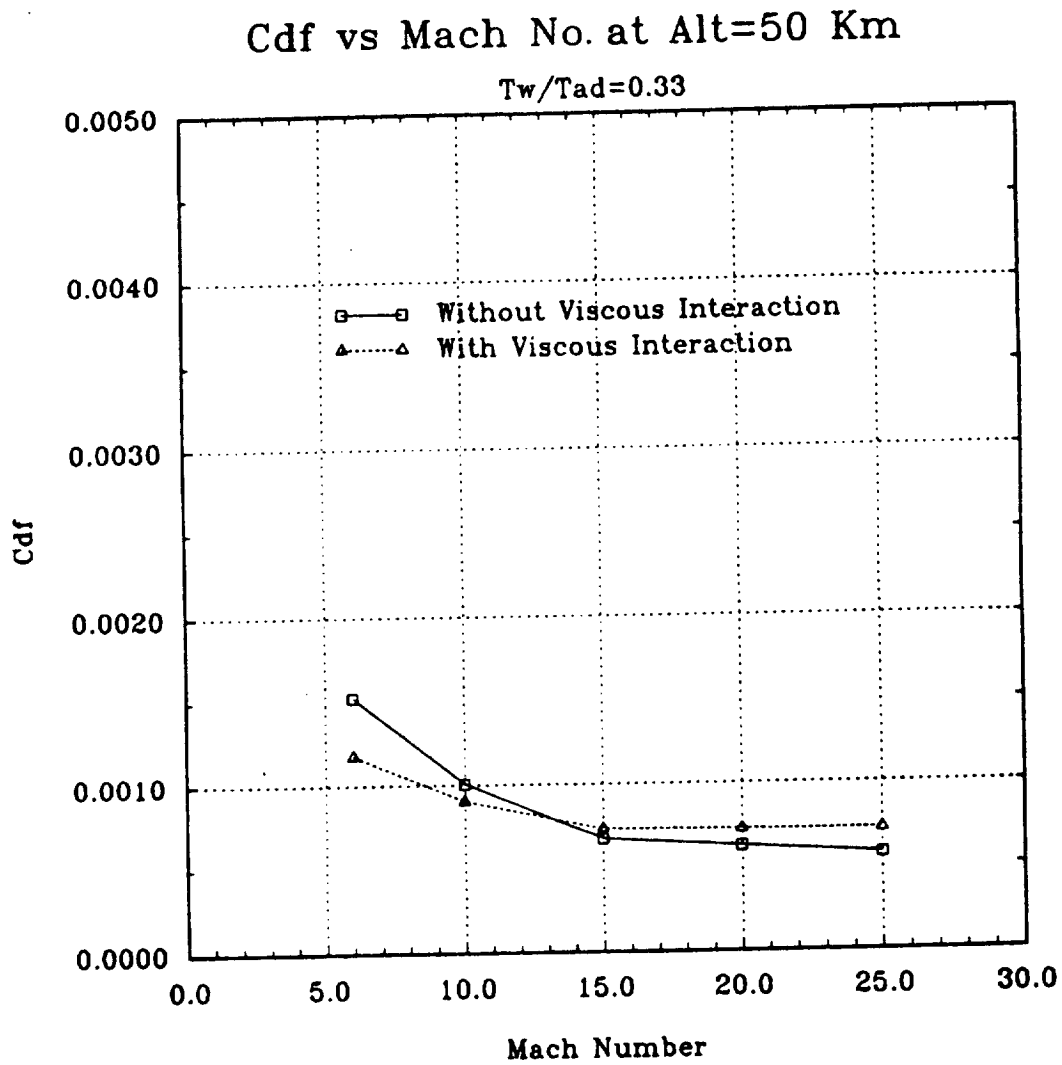
Figure C.36: C_{Df} distribution on waverider at H=50km
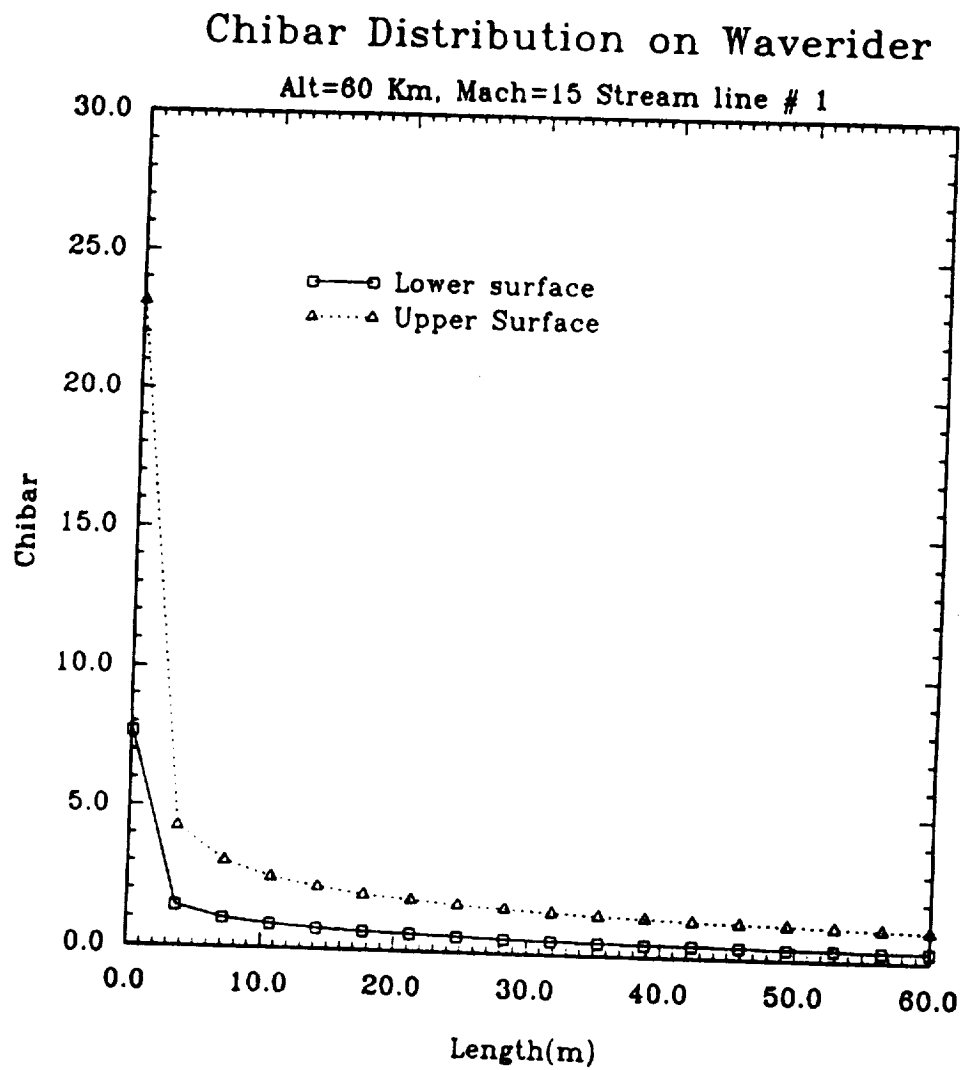
Figure C.37: $\overline{\chi}$ distribution on waverider H=60km, M=15

Chibar Distribution on Waverider

Alt=60 Km, Mach=25 Stream line # 1

Lower surface
Upper Surface
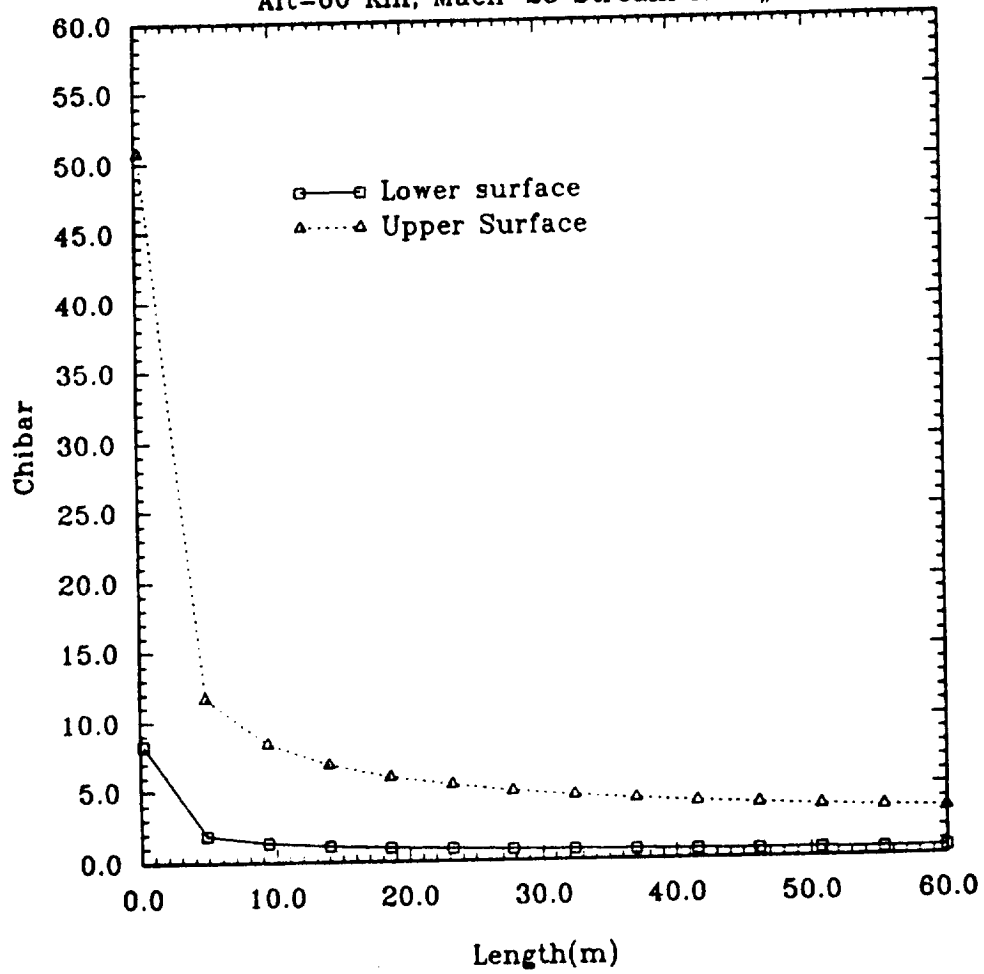
Figure C.38: $\bar{\chi}$ distribution on waverider H=60km, M=25

Figure C.39: Pressure ratio distribution on waverider H=60km, M=15

134
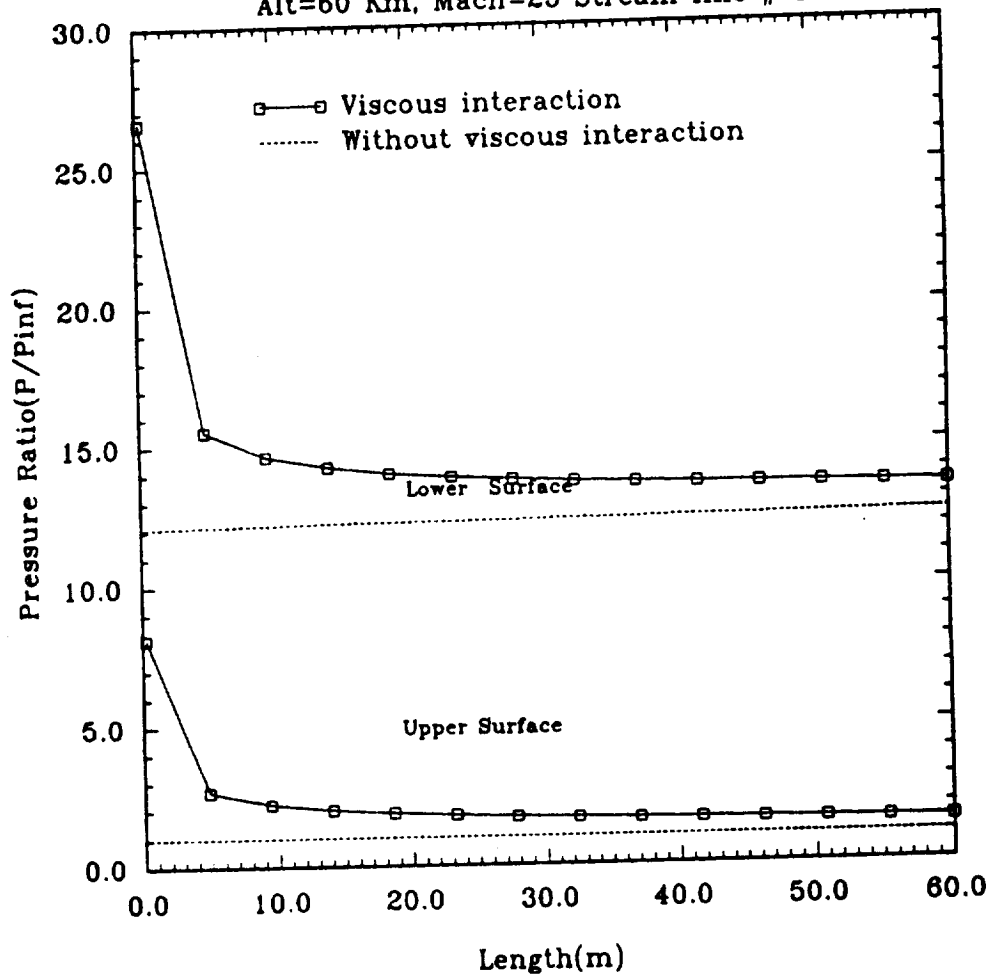
Figure C.40: Pressure ratio distribution on waverider H=60km, M=25
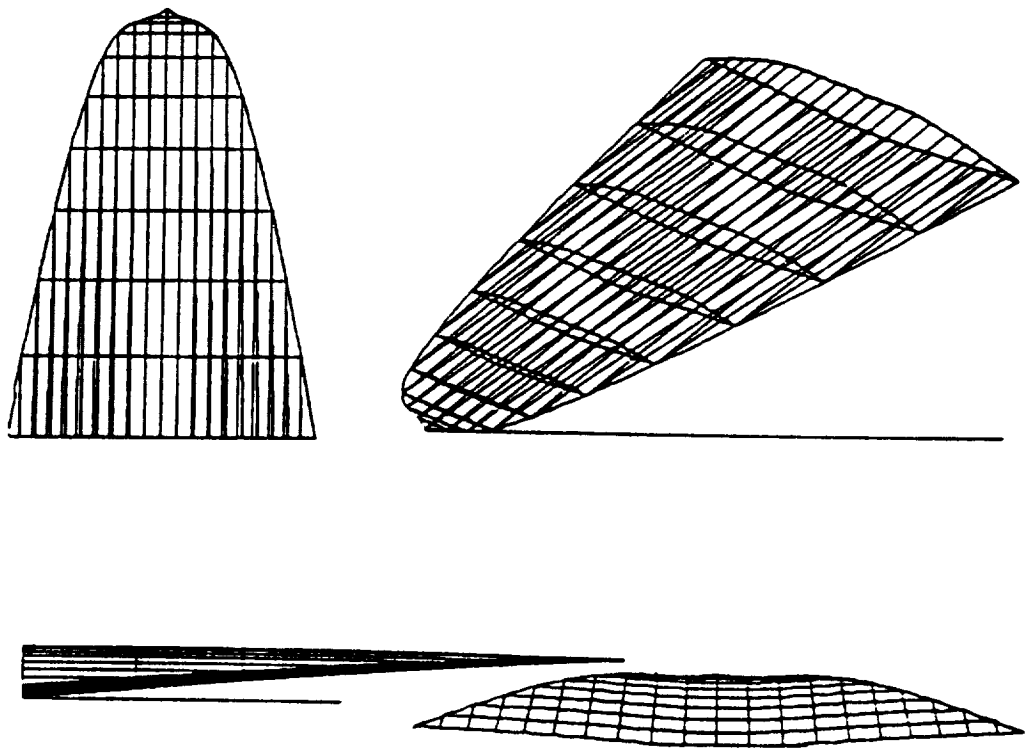
Figure C.41: Without viscous interaction waverider H=60km M=15 $\theta = 6.5$
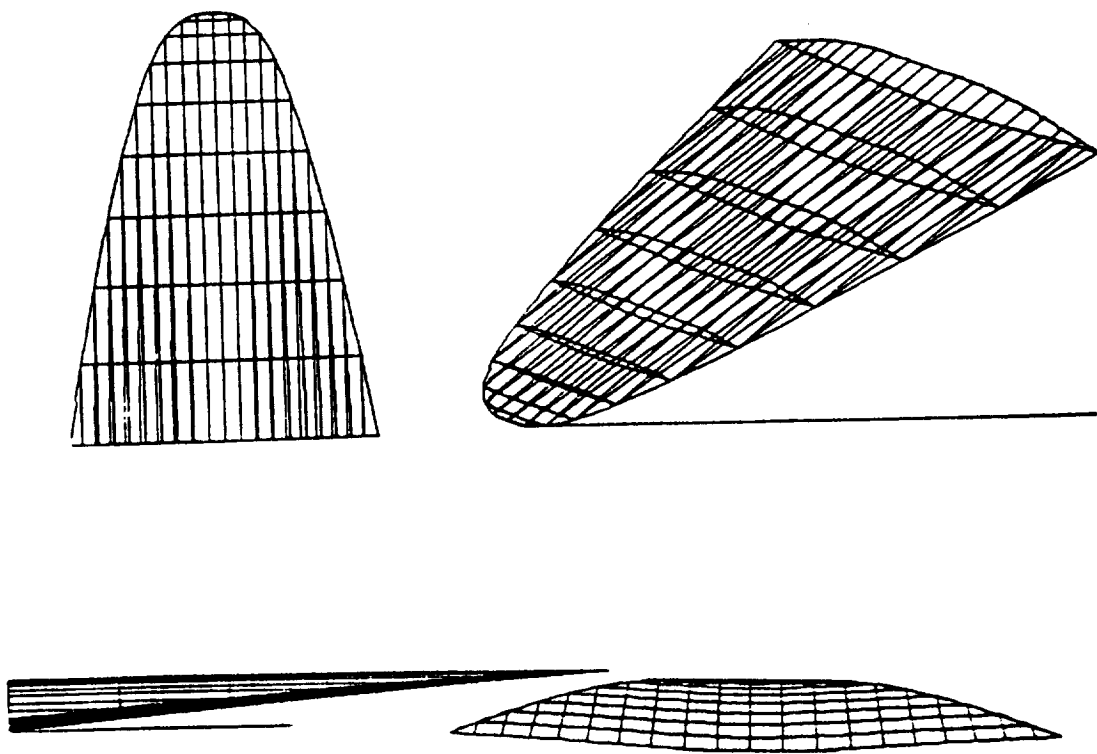
Figure C.42: Nonoptimized viscous interaction waverider H=60km M=15 $\theta = 6.5$
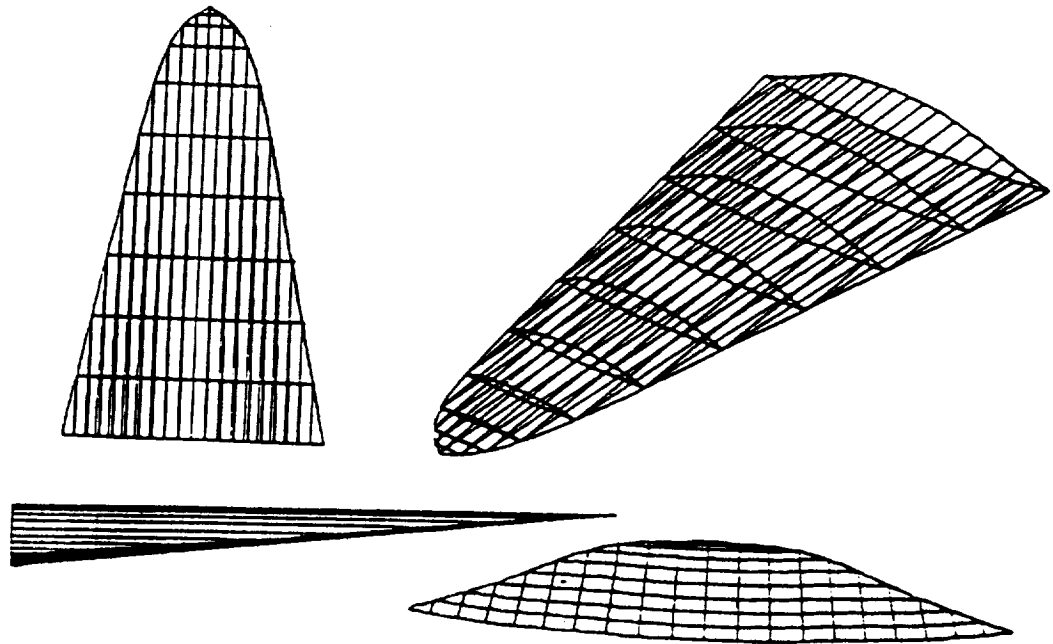
Figure C.43: Without viscous interaction waverider H=60km M=25 $\theta = 6.5$
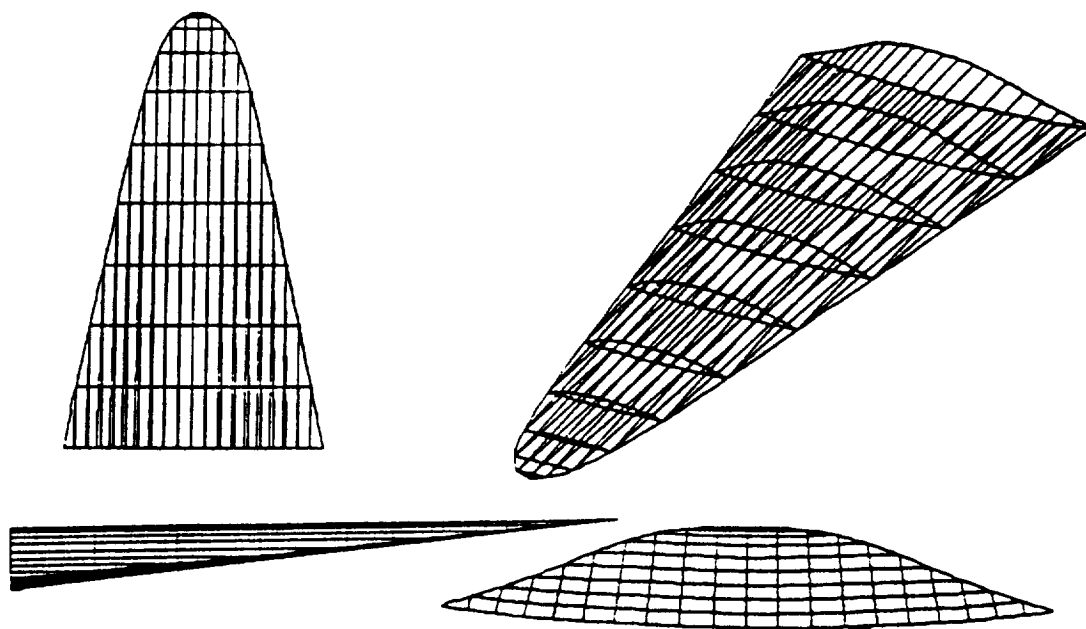
Figure C.44: Nonoptimized viscous interaction waverider H=60km M=25 $\theta = 6.5$

Figure C.45: Lift/Drag distribution on waverider at H=60km

Cl vs Mach No. at Alt=60 Km

Tw/Tad=0.33
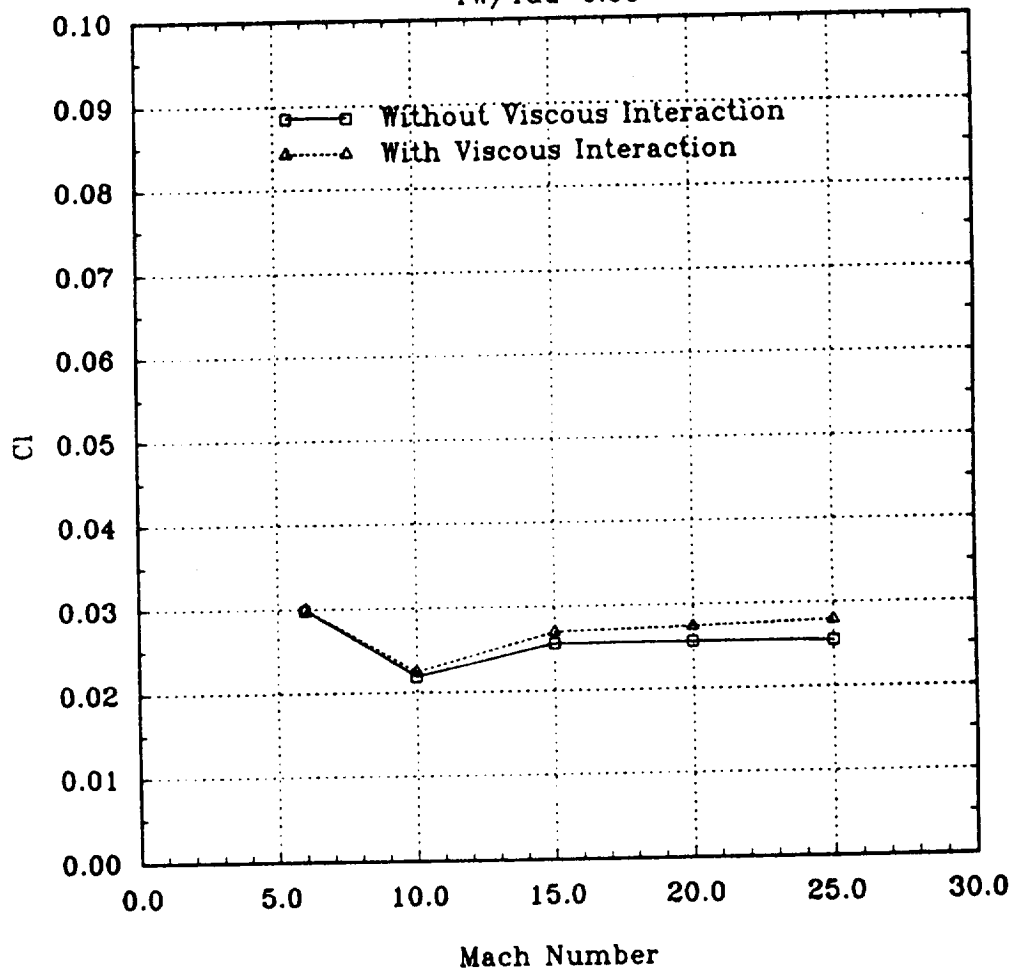
Figure C.46: Lift coefficient distribution on waverider at H=60km
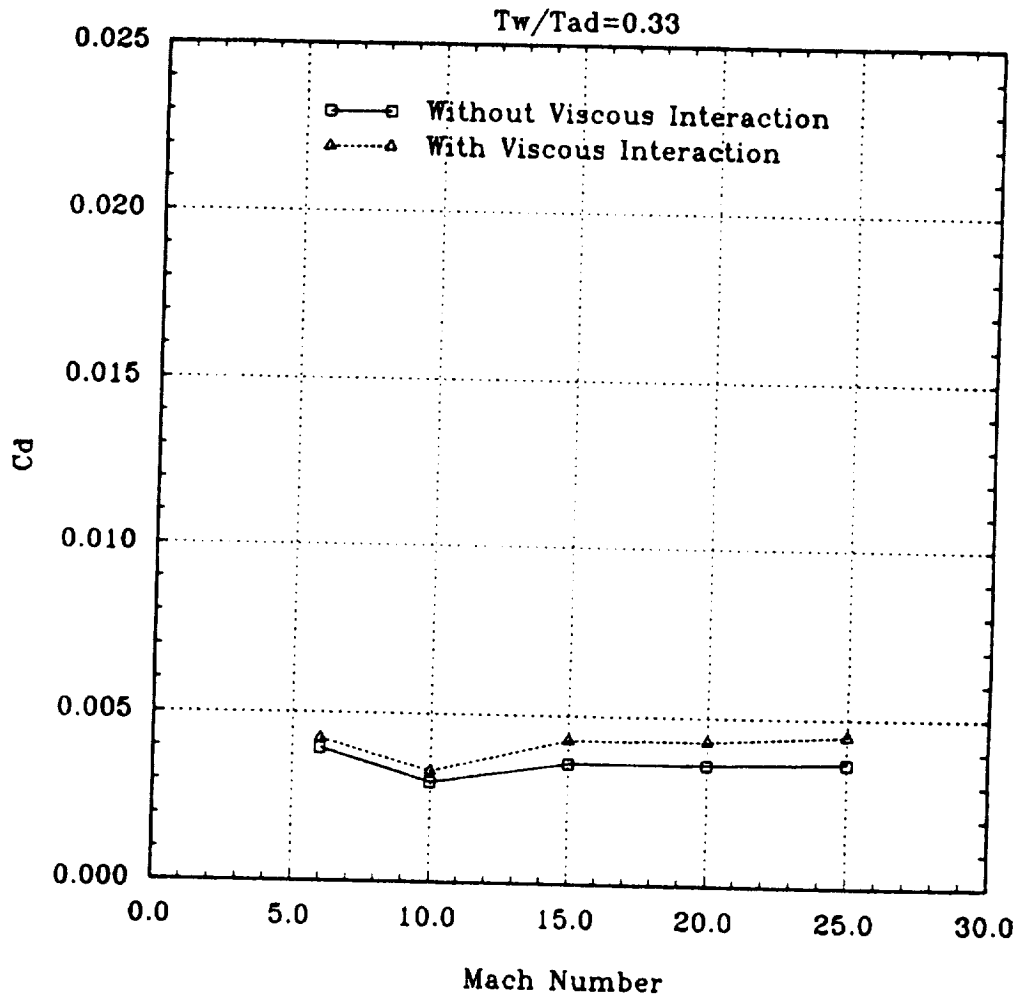
Figure C.47: Drag coefficient distribution on waverider at H=60km
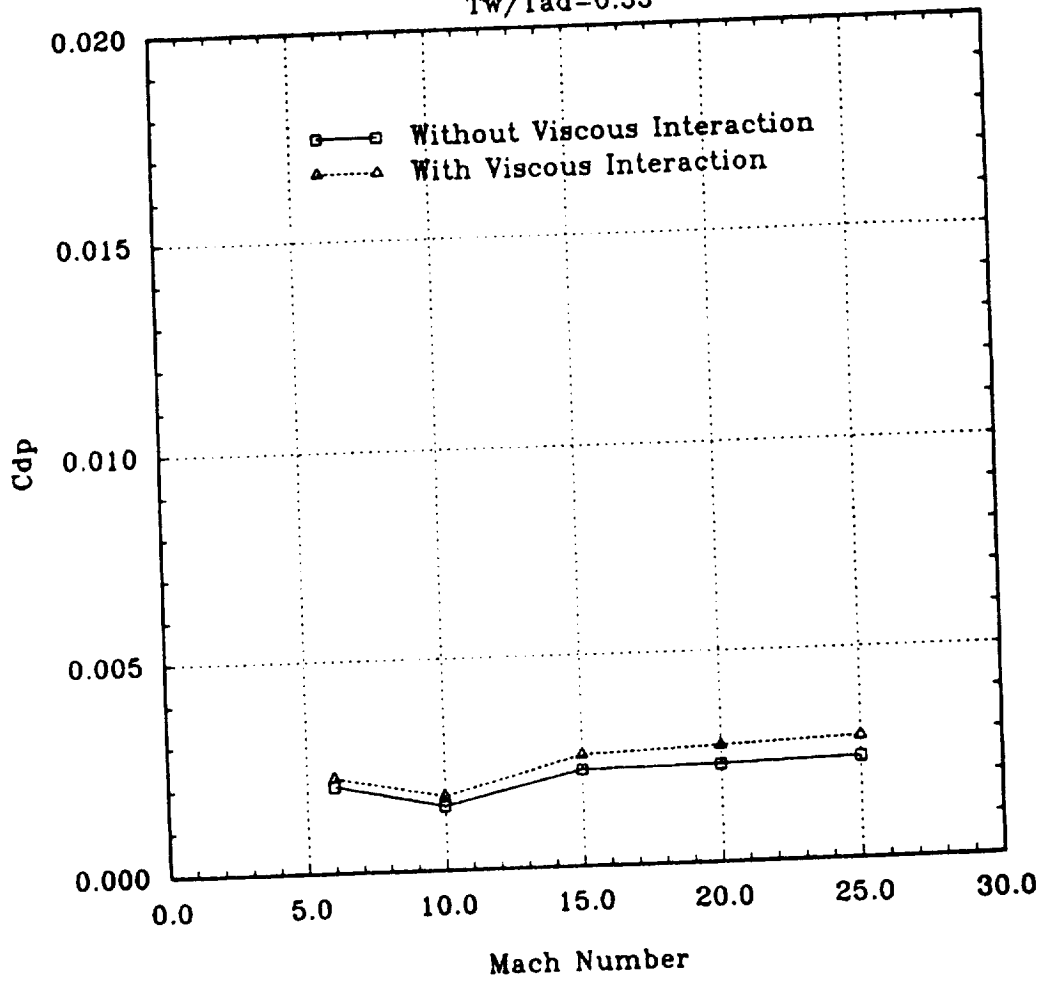
Figure C.48: C_{Dp} distribution on waverider at H=60km
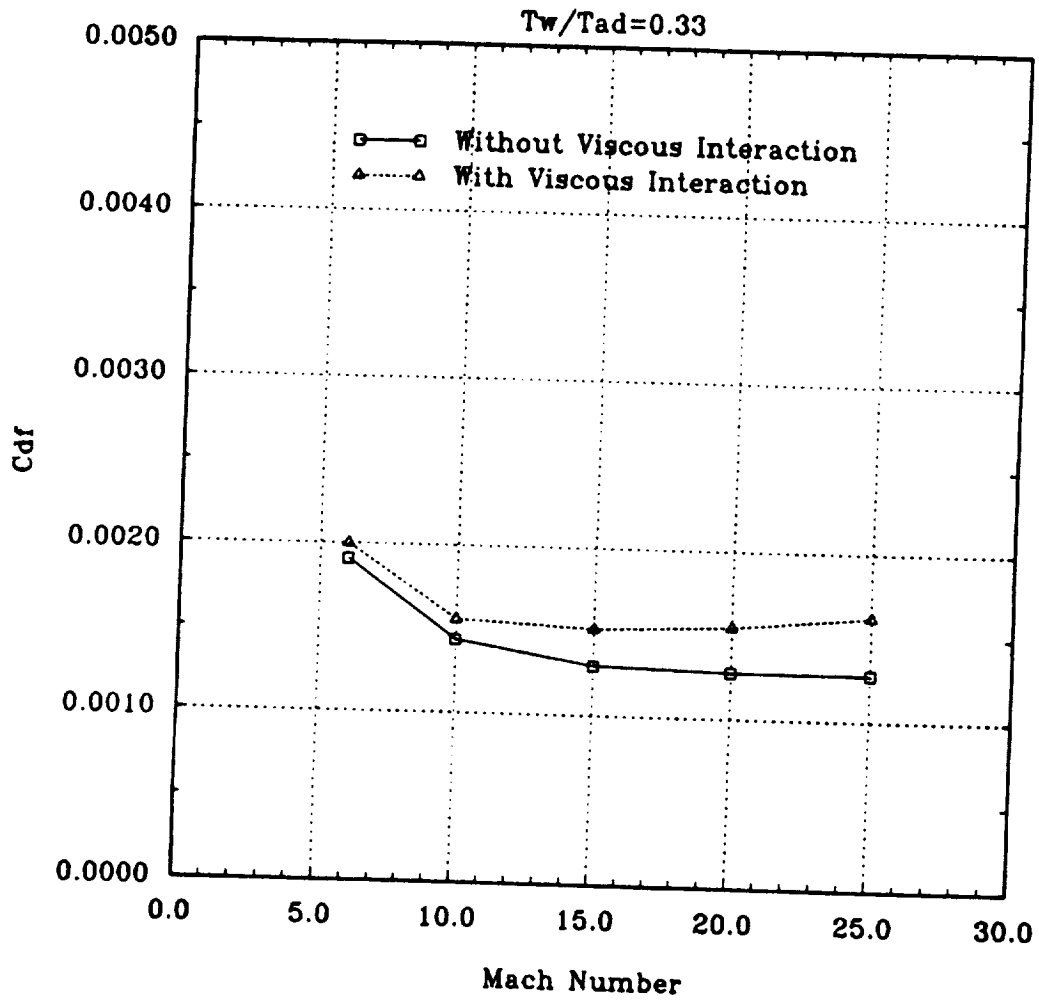
Figure C.49: C_{Df} distribution on waverider at H=60km
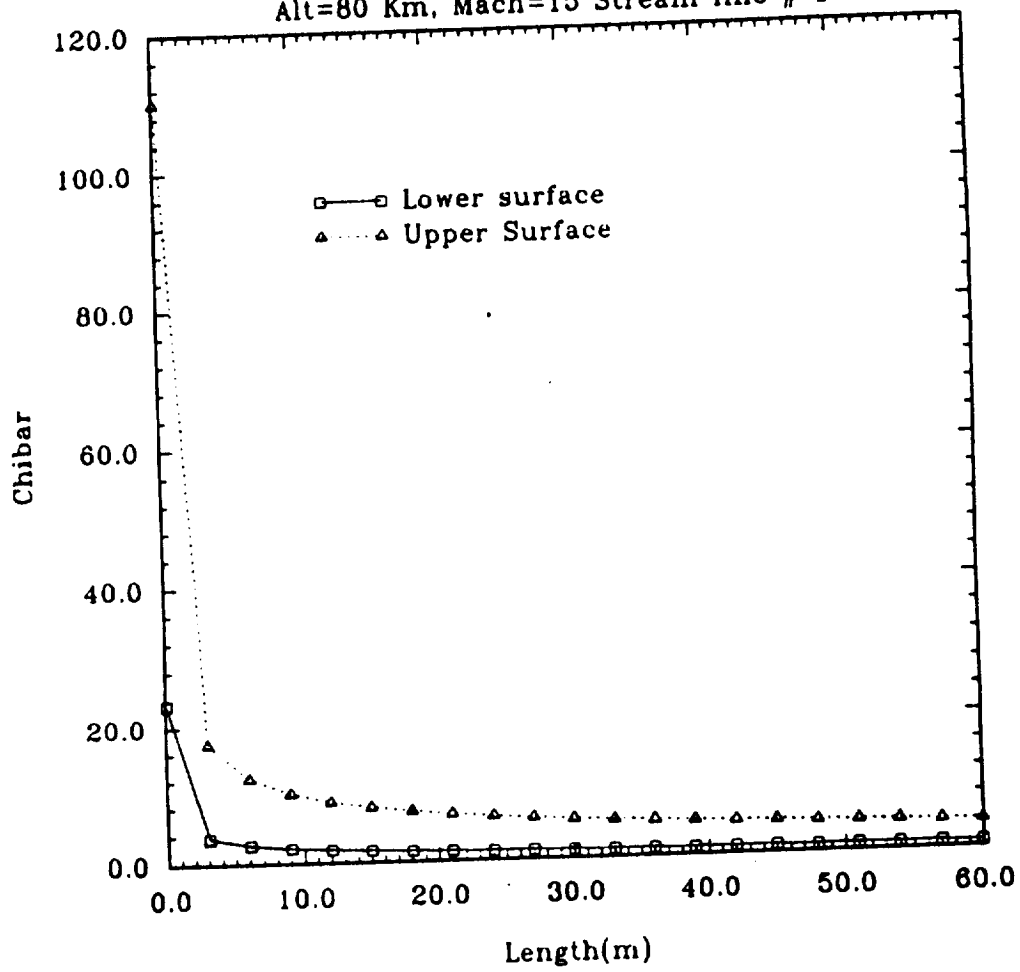
Figure C.50: $\overline{\chi}$ distribution on waverider H=80km, M=15

Figure C.51: $\overline{\chi}$ distribution on waverider H=80km, M=25

146
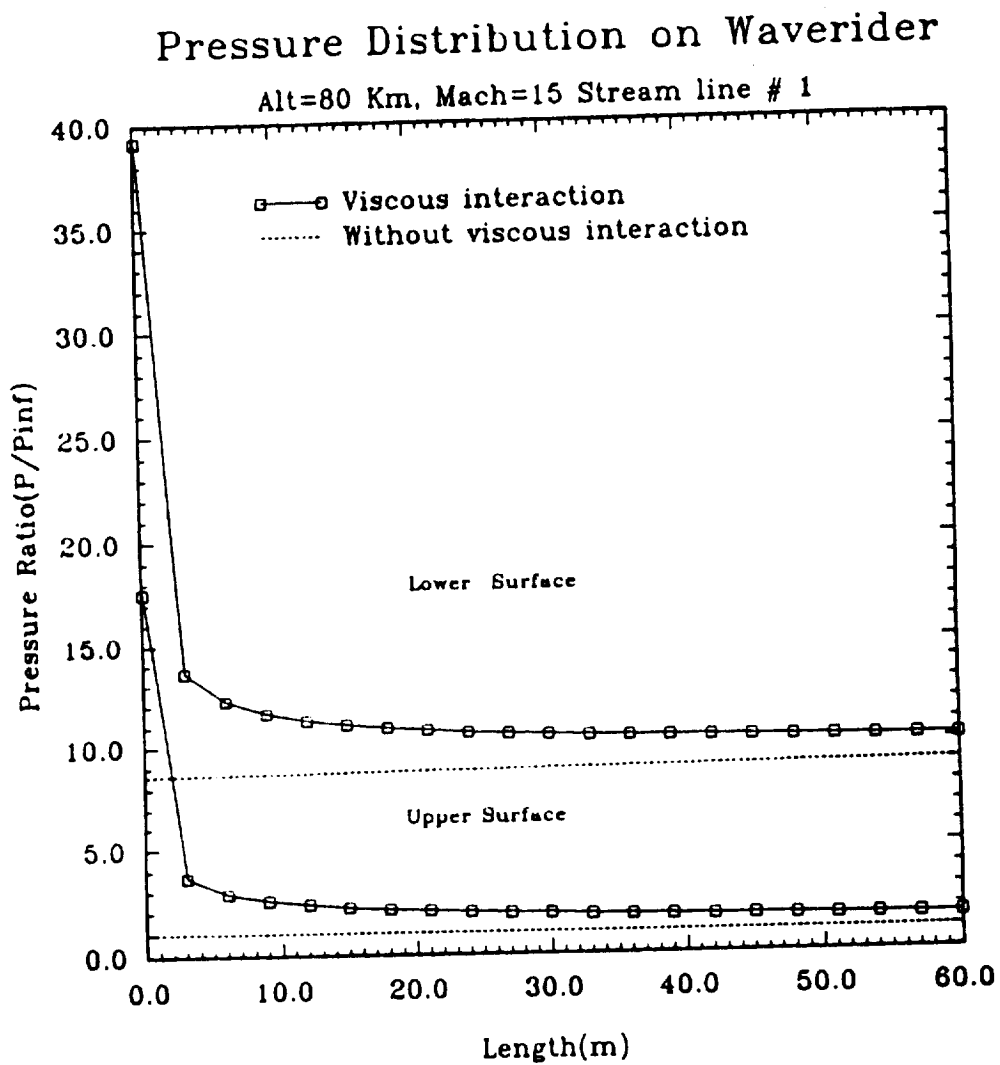
Figure C.52: Pressure ratio distribution on waverider H=80km, M=15
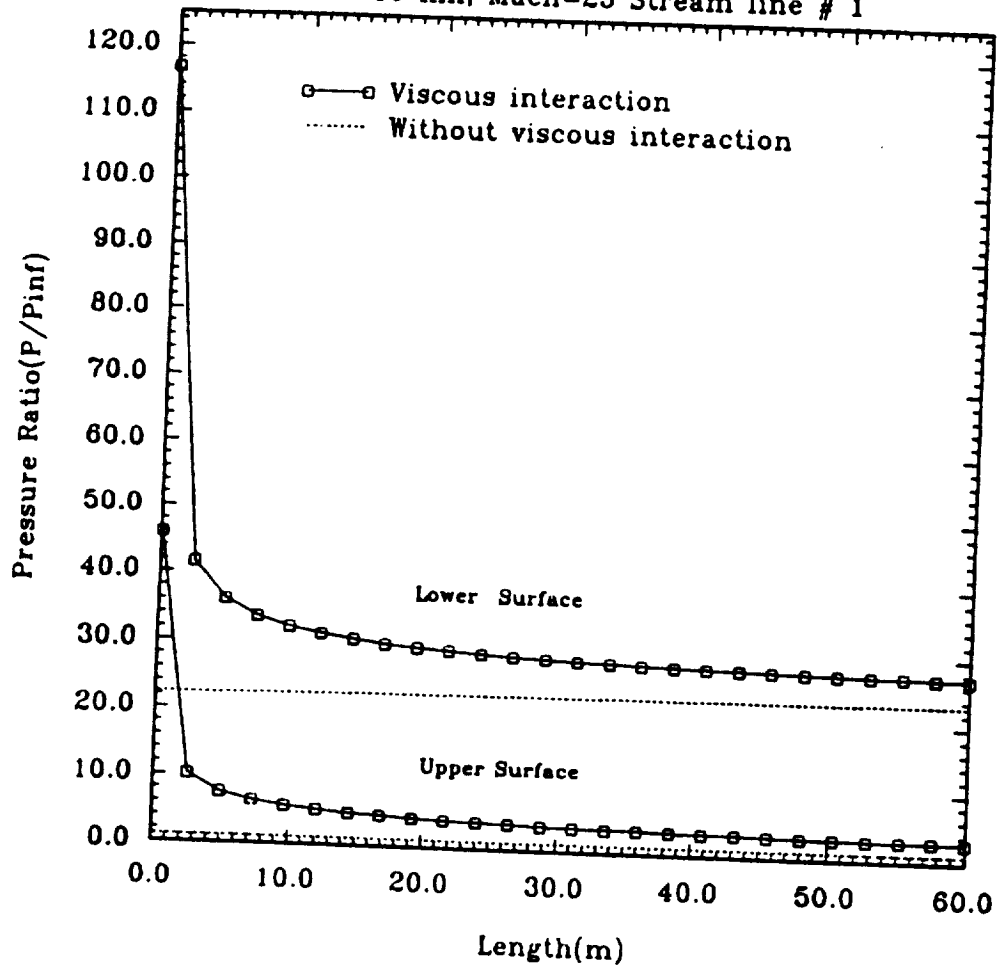
Figure C.53: Pressure ratio distribution on waverider H=80km, M=25
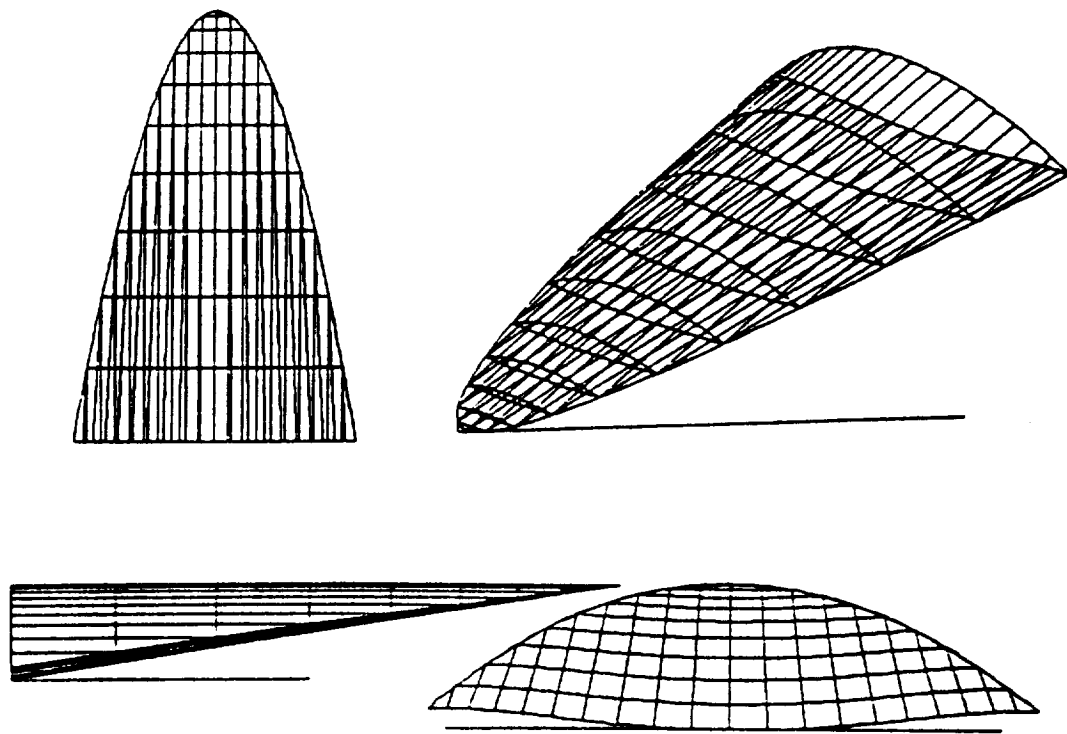
Figure C.54: Without viscous interaction waverider H=80km M=15 $\theta = 9$
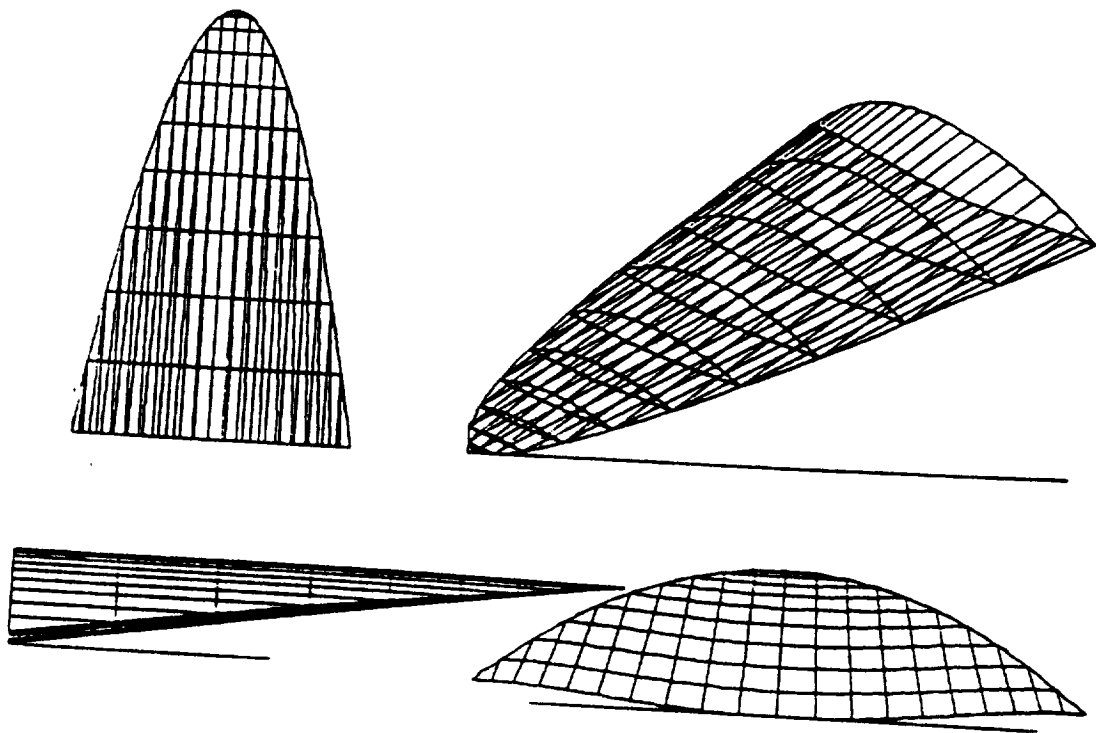
Figure C.55: Nonoptimized viscous interaction waverider H=80km M=15 $\theta = 9$
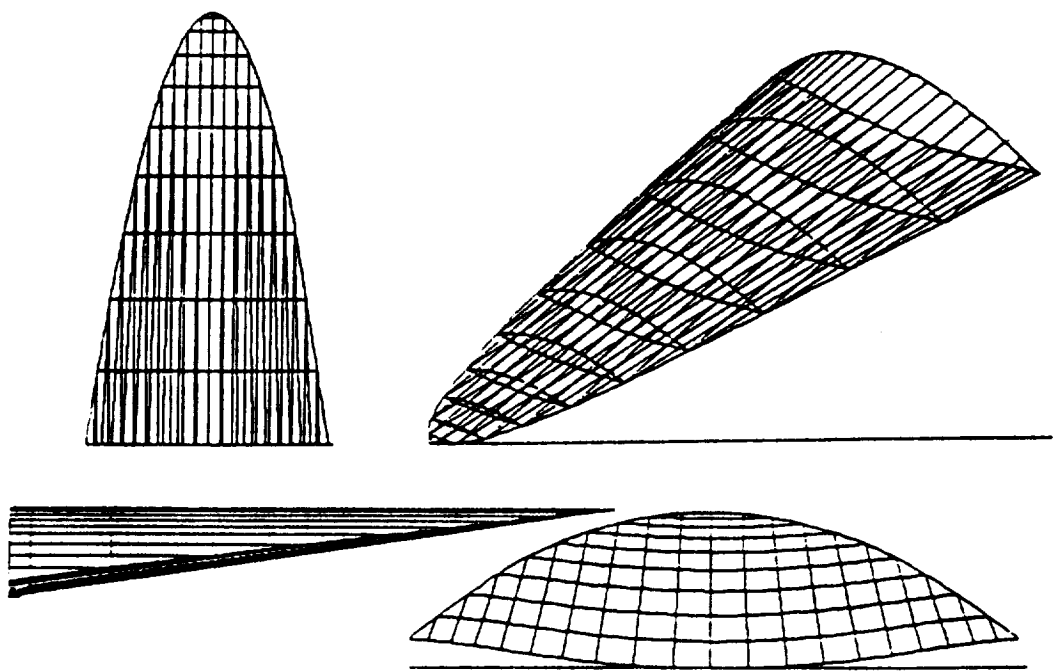
Figure C.56: Without viscous interaction waverider H=80km M=25 $\theta = 9$
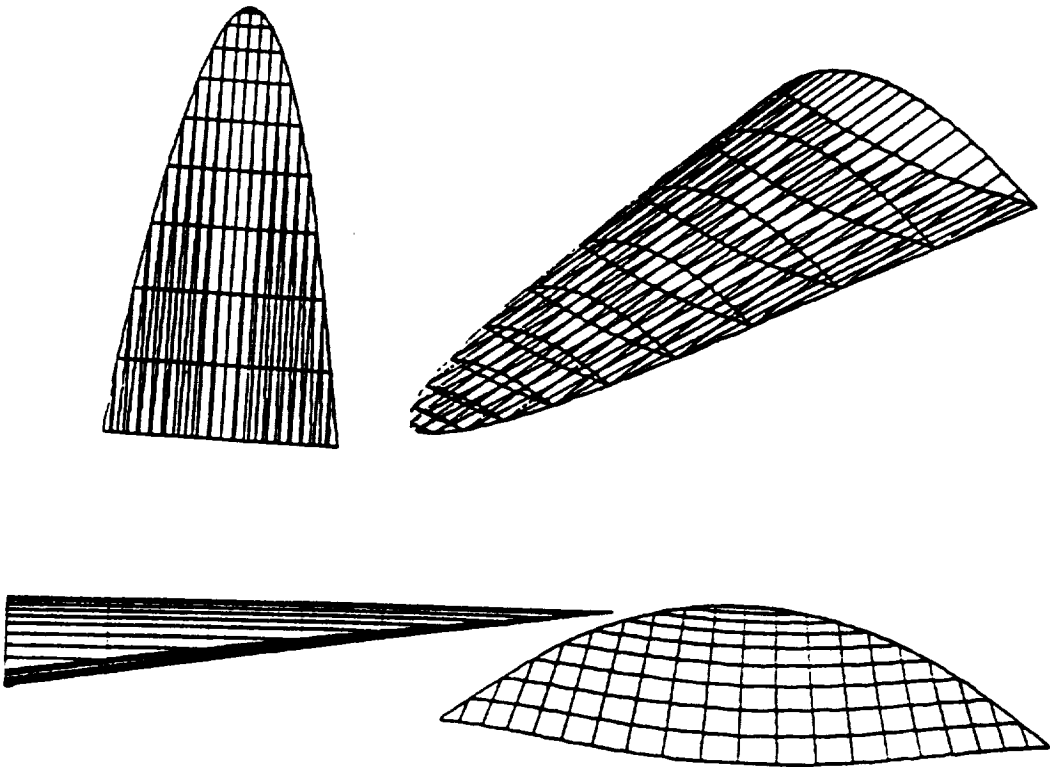
Figure C.57: Nonoptimized viscous interaction waverider H=80km, M=25 $\theta = 9$
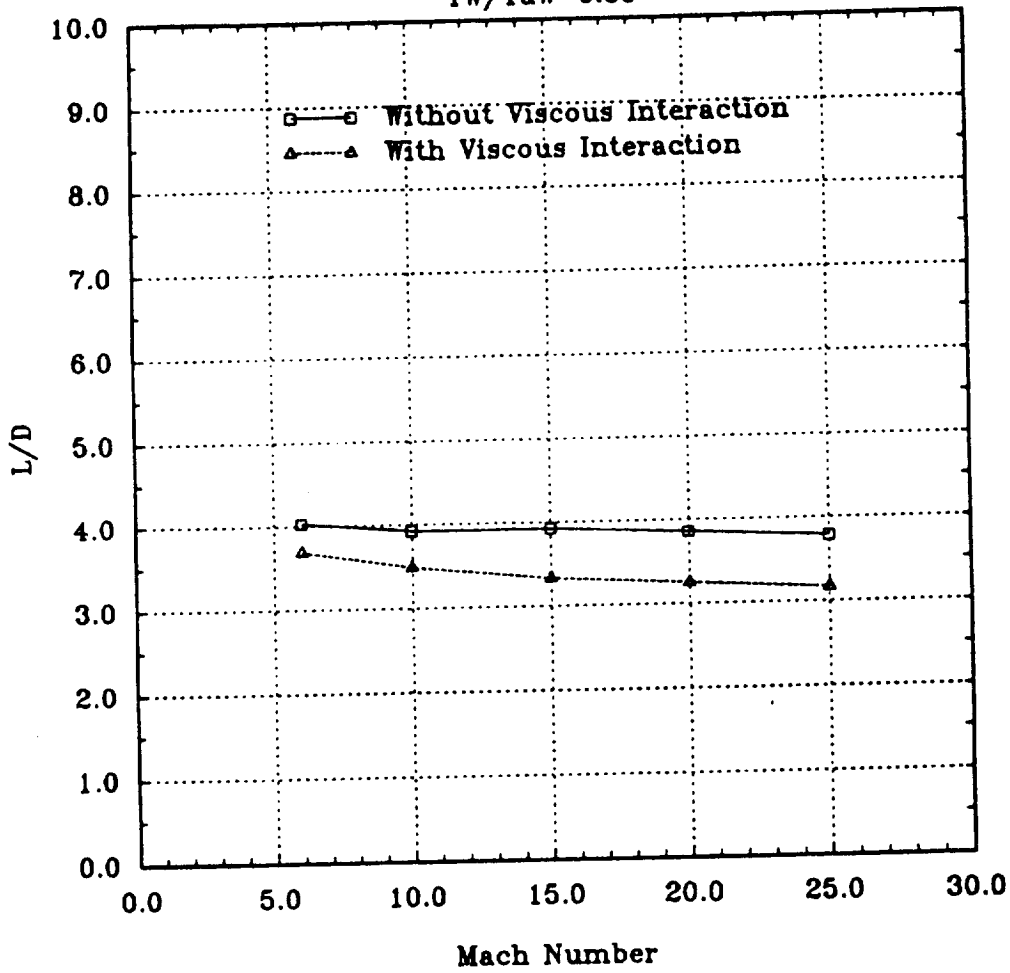
Figure C.58: Lift/Drag distribution on waverider at H=80km
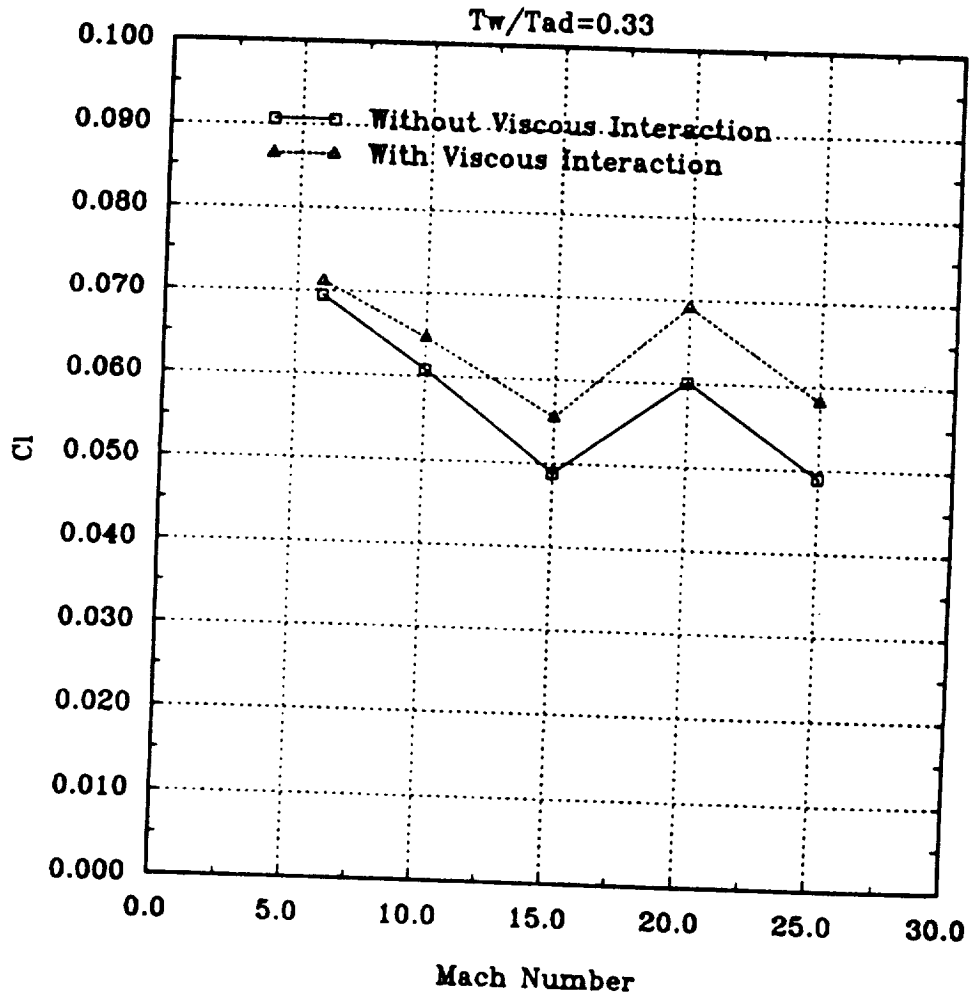
Figure C.59: Lift coefficient distribution on waverider at H=80km

154
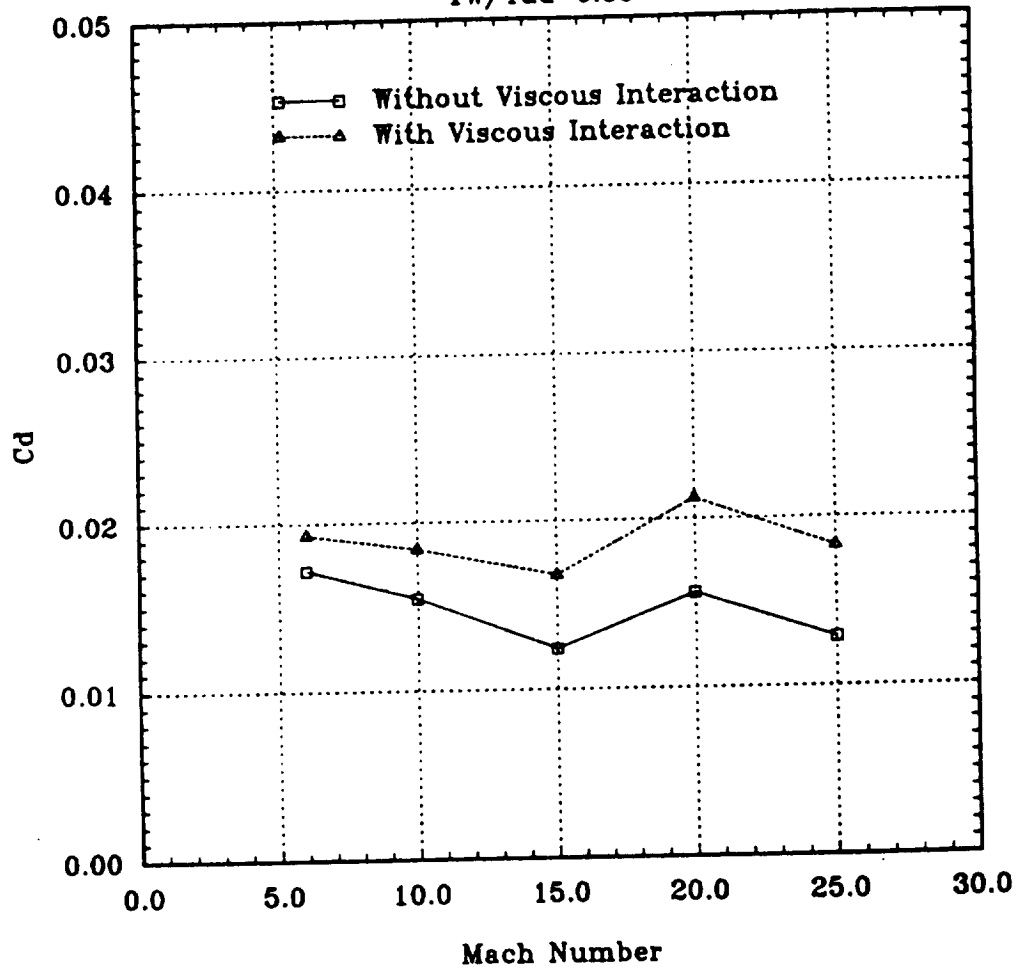
Figure C.60: Drag coefficient distribution on waverider at H=80km
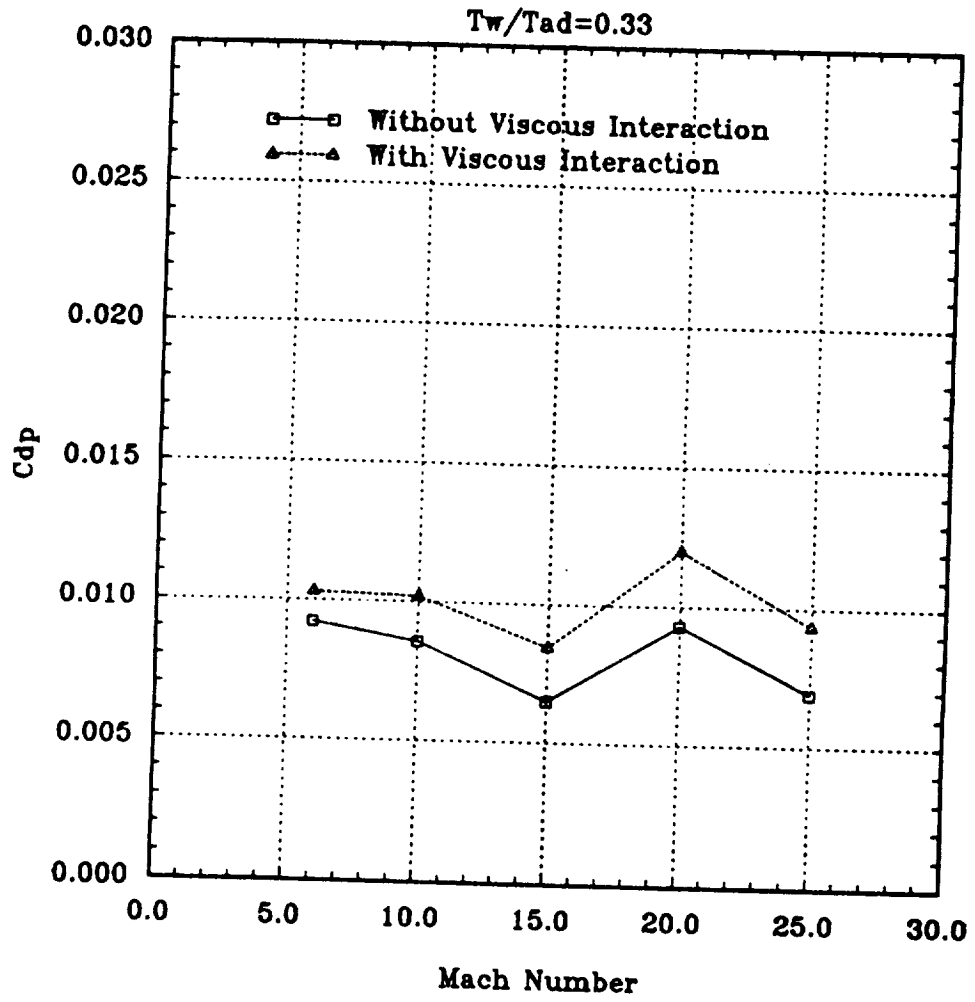
Figure C.61: C_{Dp} distribution on waverider at H=80km
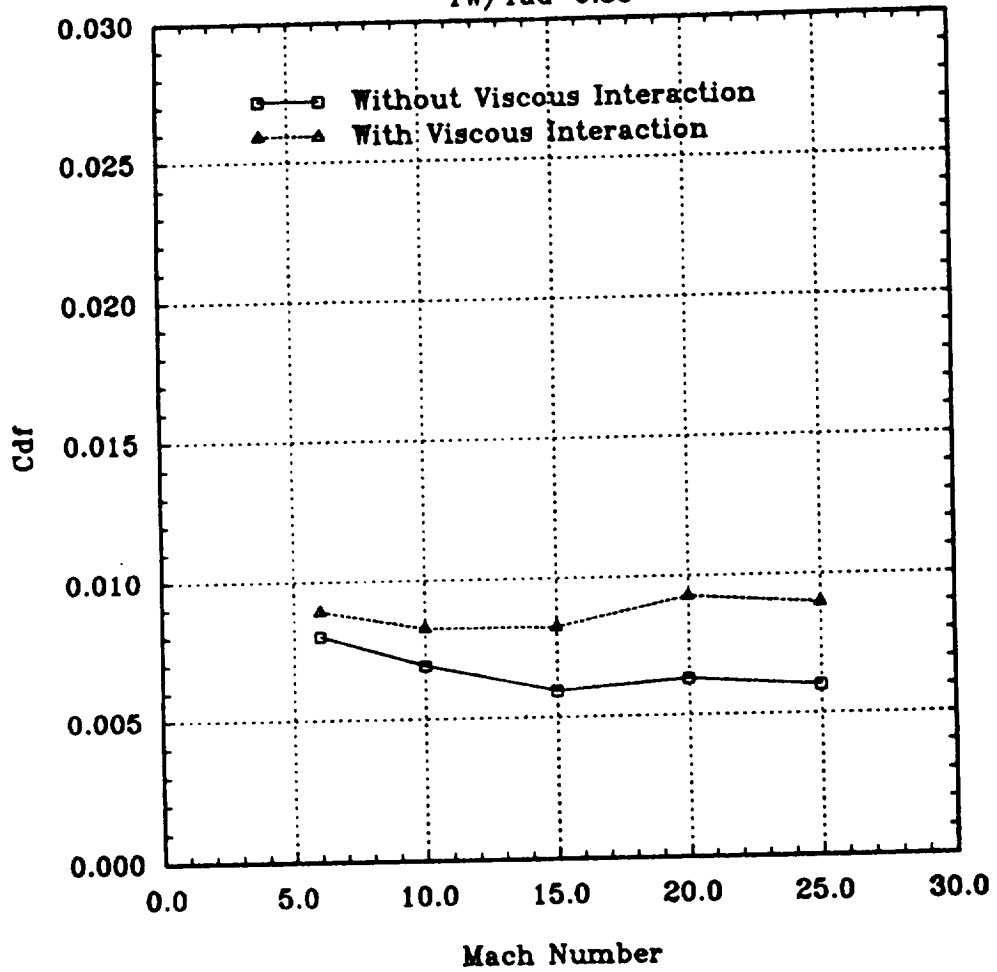
Figure C.62: C_{Df} distribution on waverider at H=80km
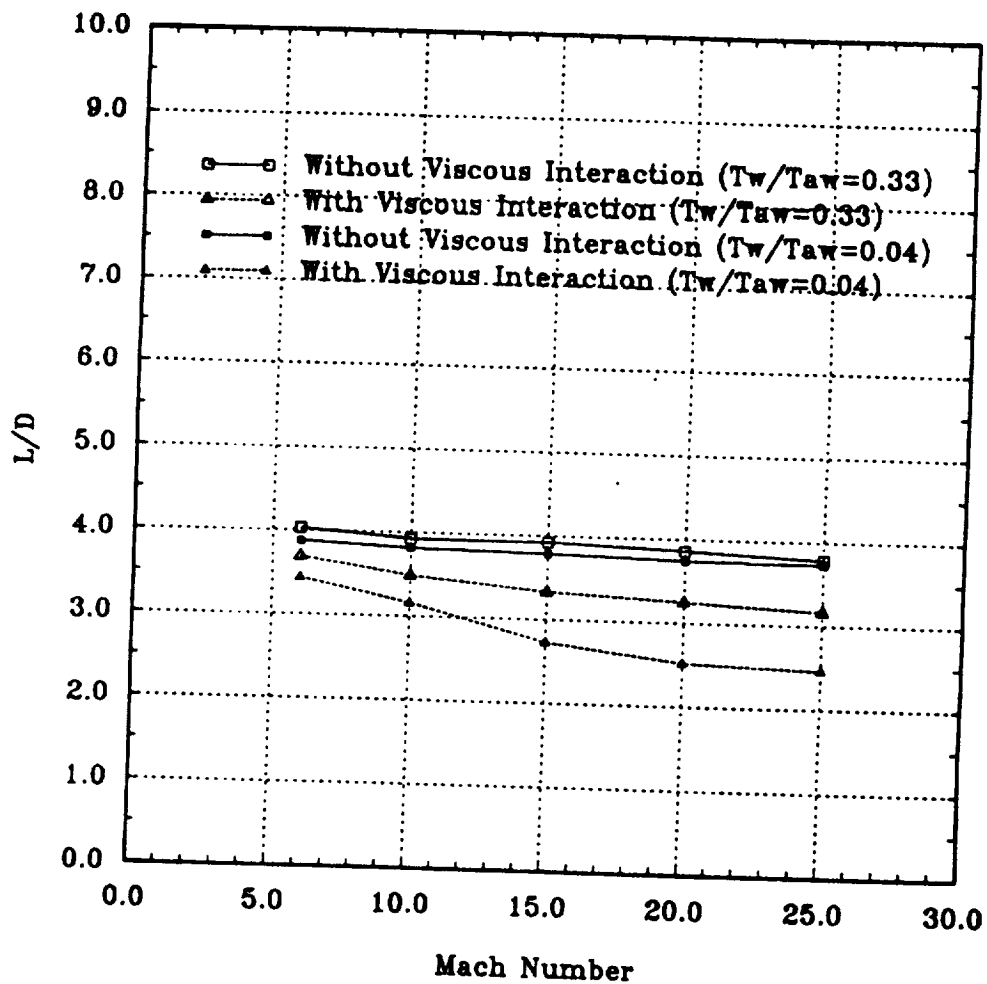
Figure C.63: Comparison of L/D between Tw/Taw=0.04, 0.33 H=80km
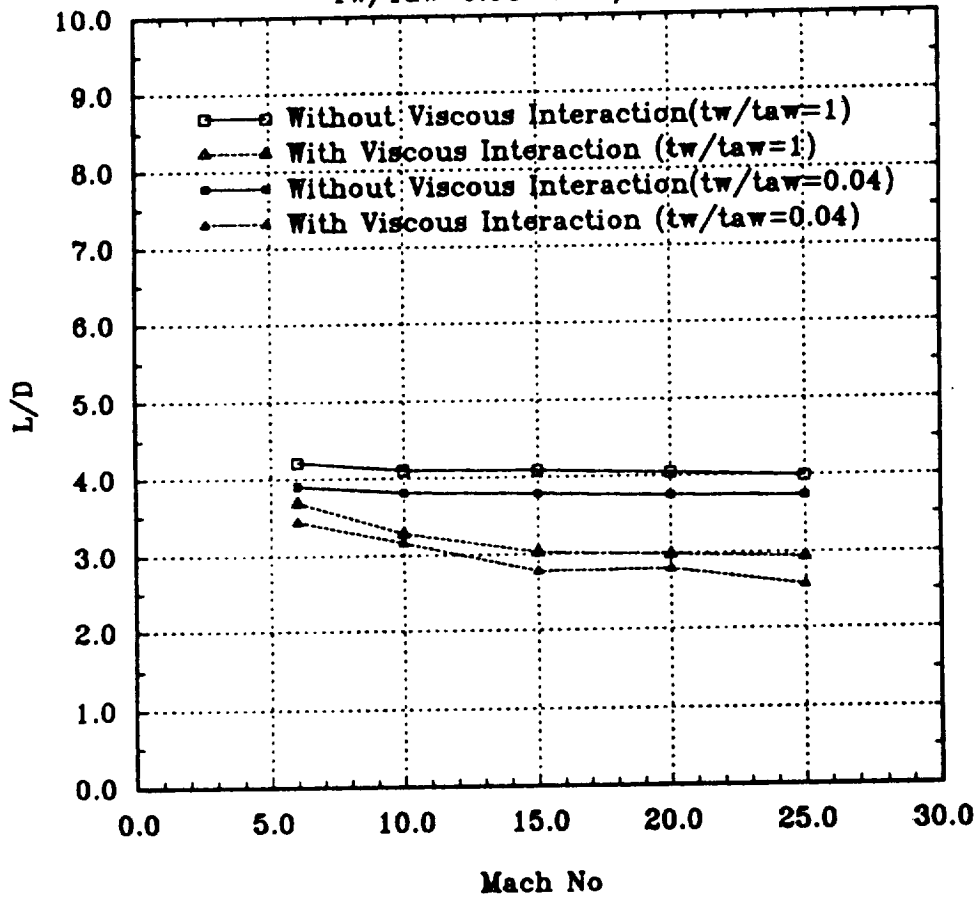
Figure C.64: Comparison of L/D between Tw/Taw=0.04, 1.0 H=80km

159
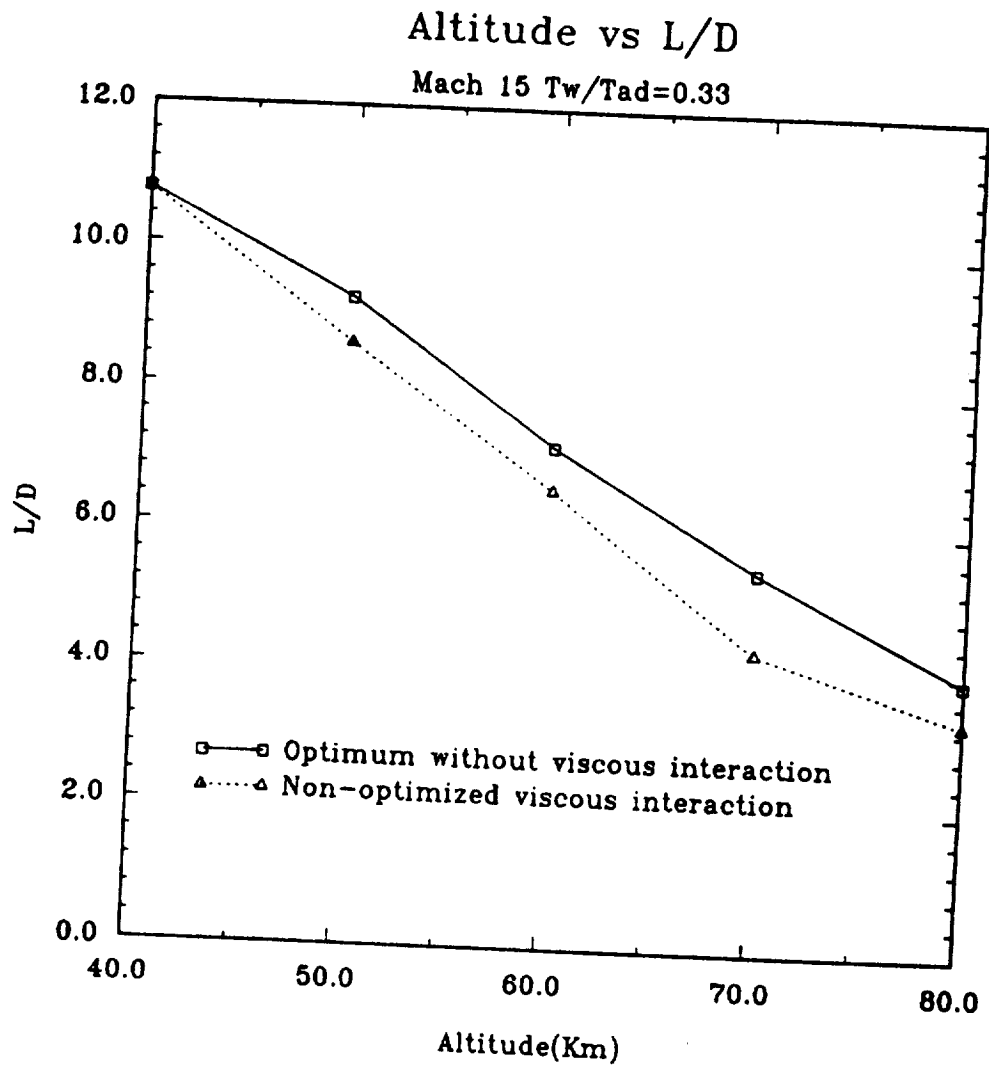
Figure C.65: L/D distribution versus altitude on M=15

160
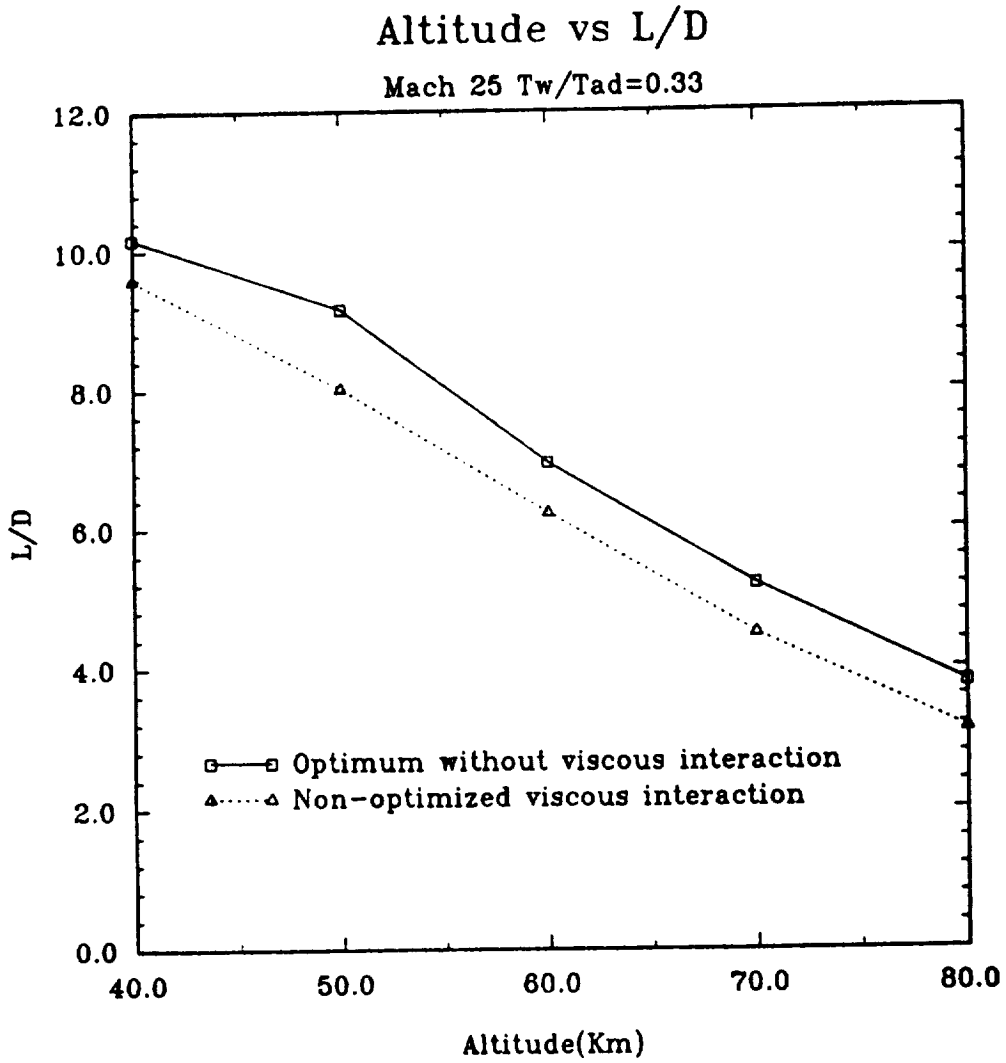
Figure C.66: L/D distribution versus altitude on M=25
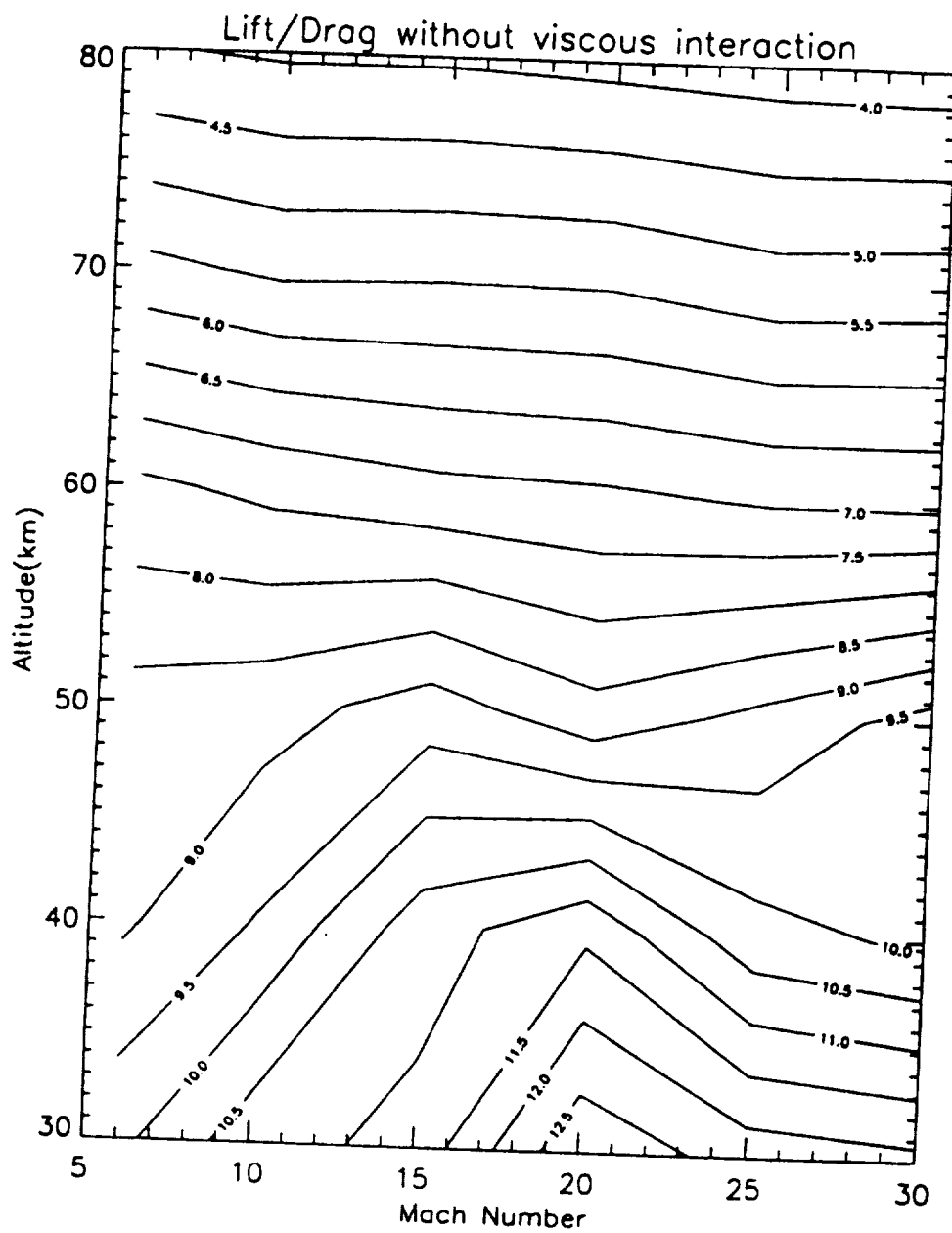
Figure C.67: L/D contour without viscous interaction
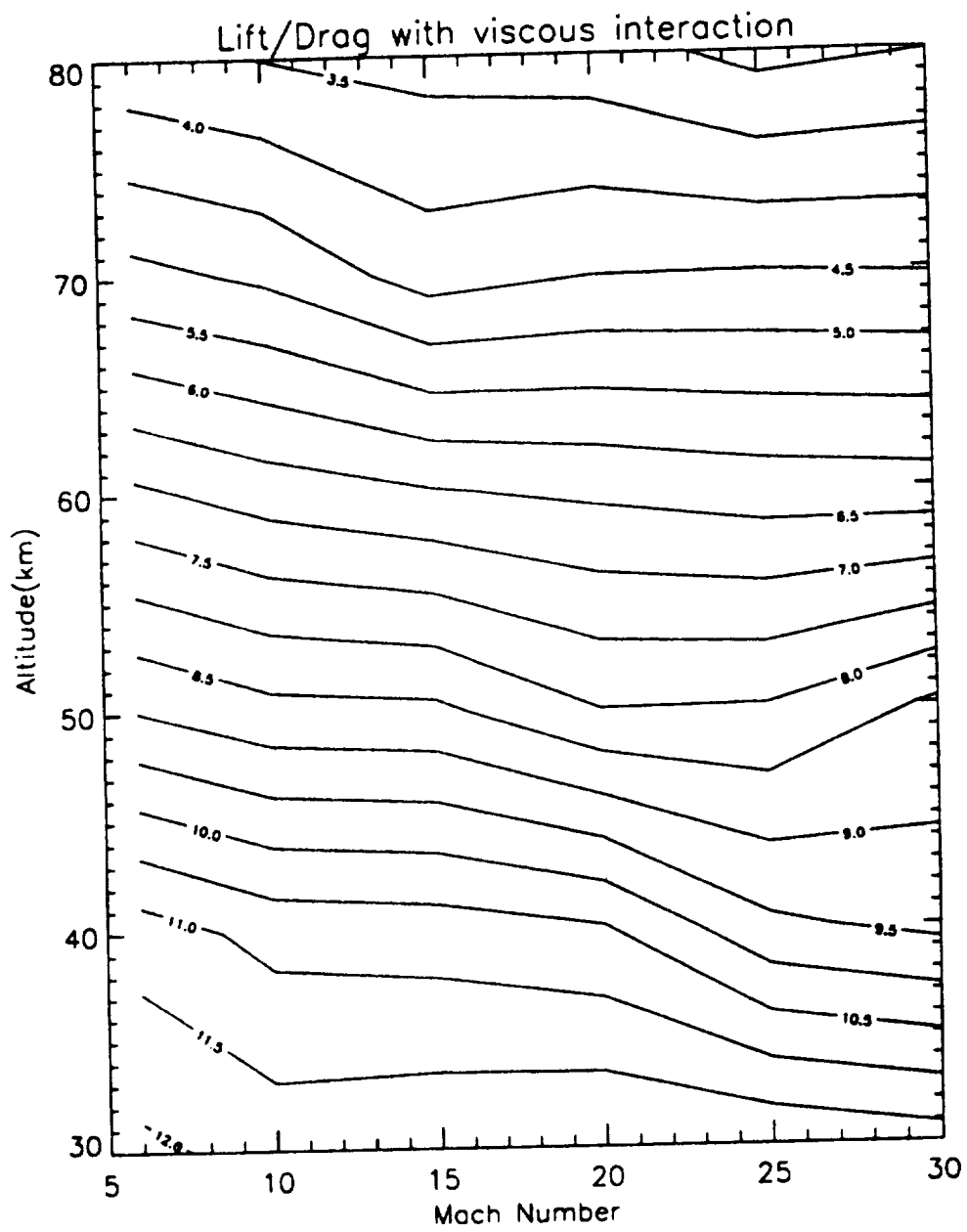
Figure C.68: L/D contour with viscous interaction
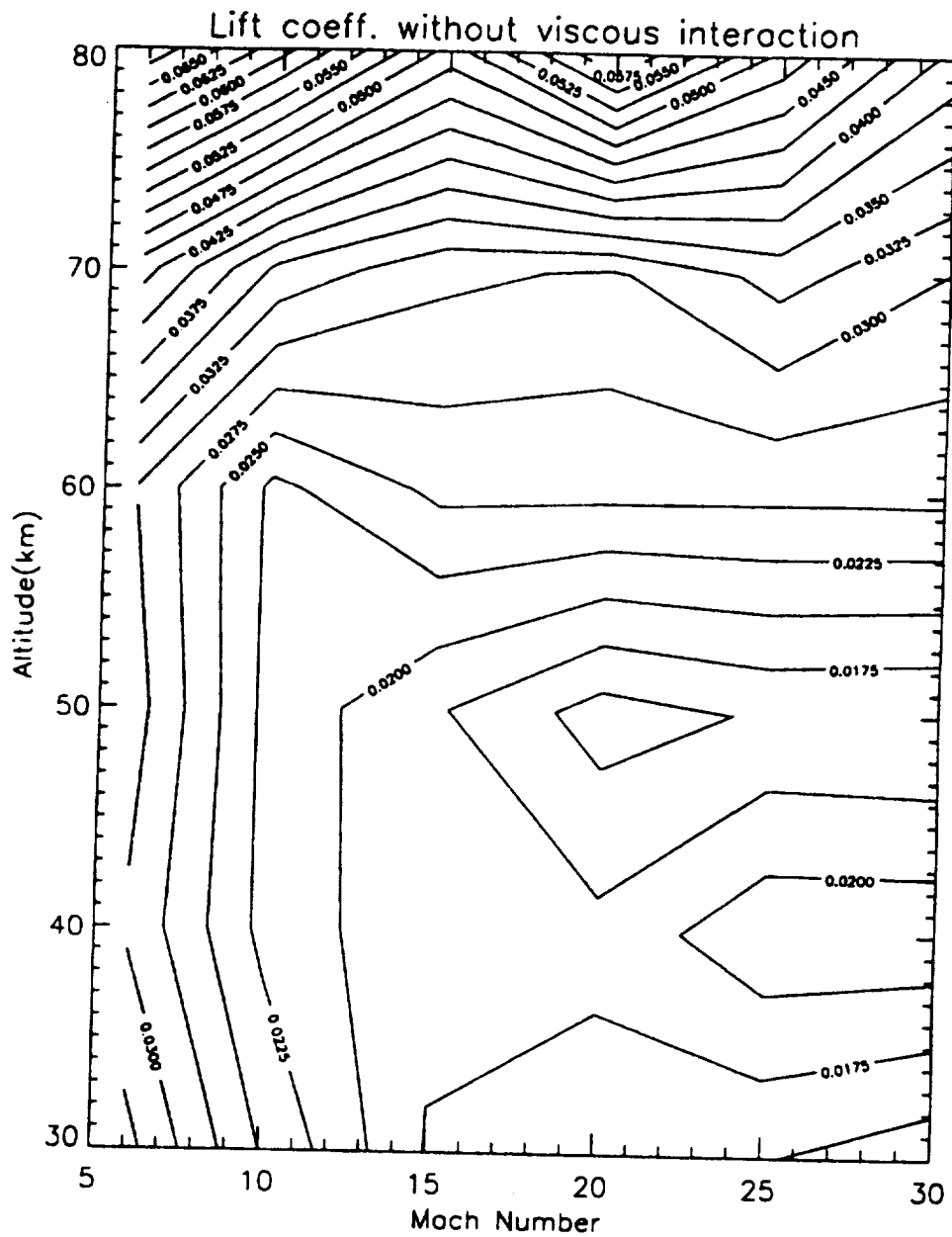
Figure C.69: Lift coefficient contour without viscous interaction
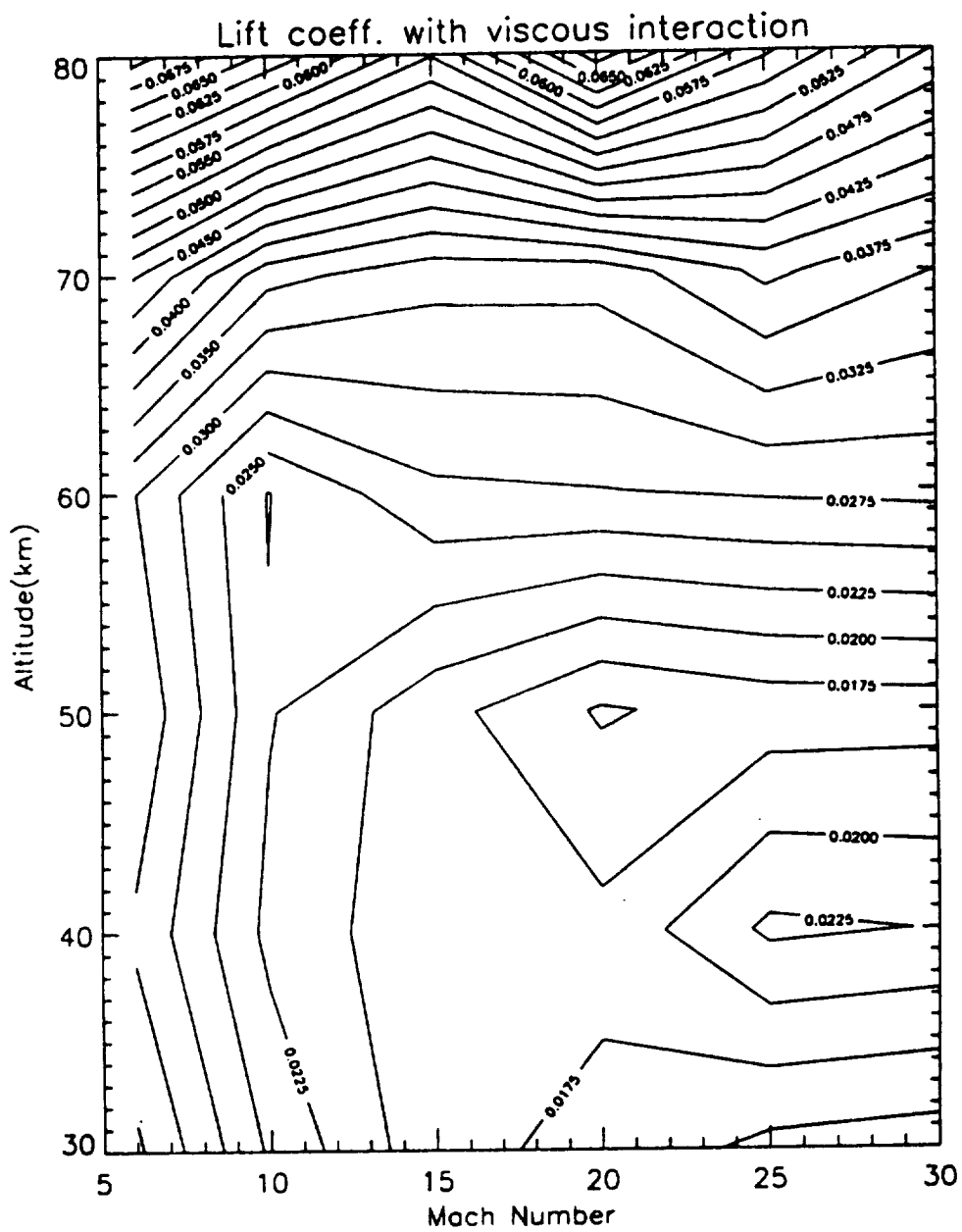
Figure C.70: Lift coefficient contour with viscous interaction
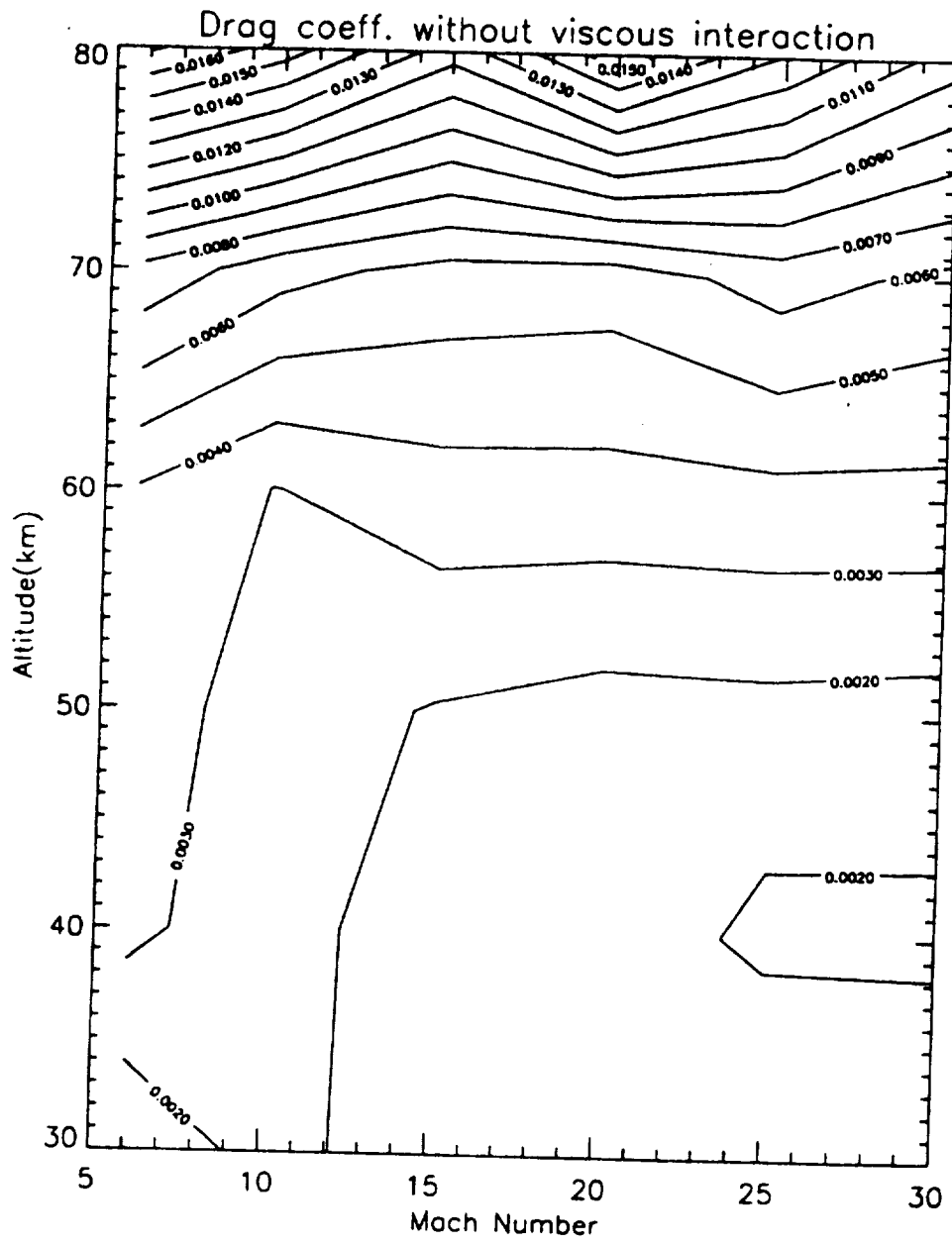
Figure C.71: Drag coefficient contour without viscous interaction
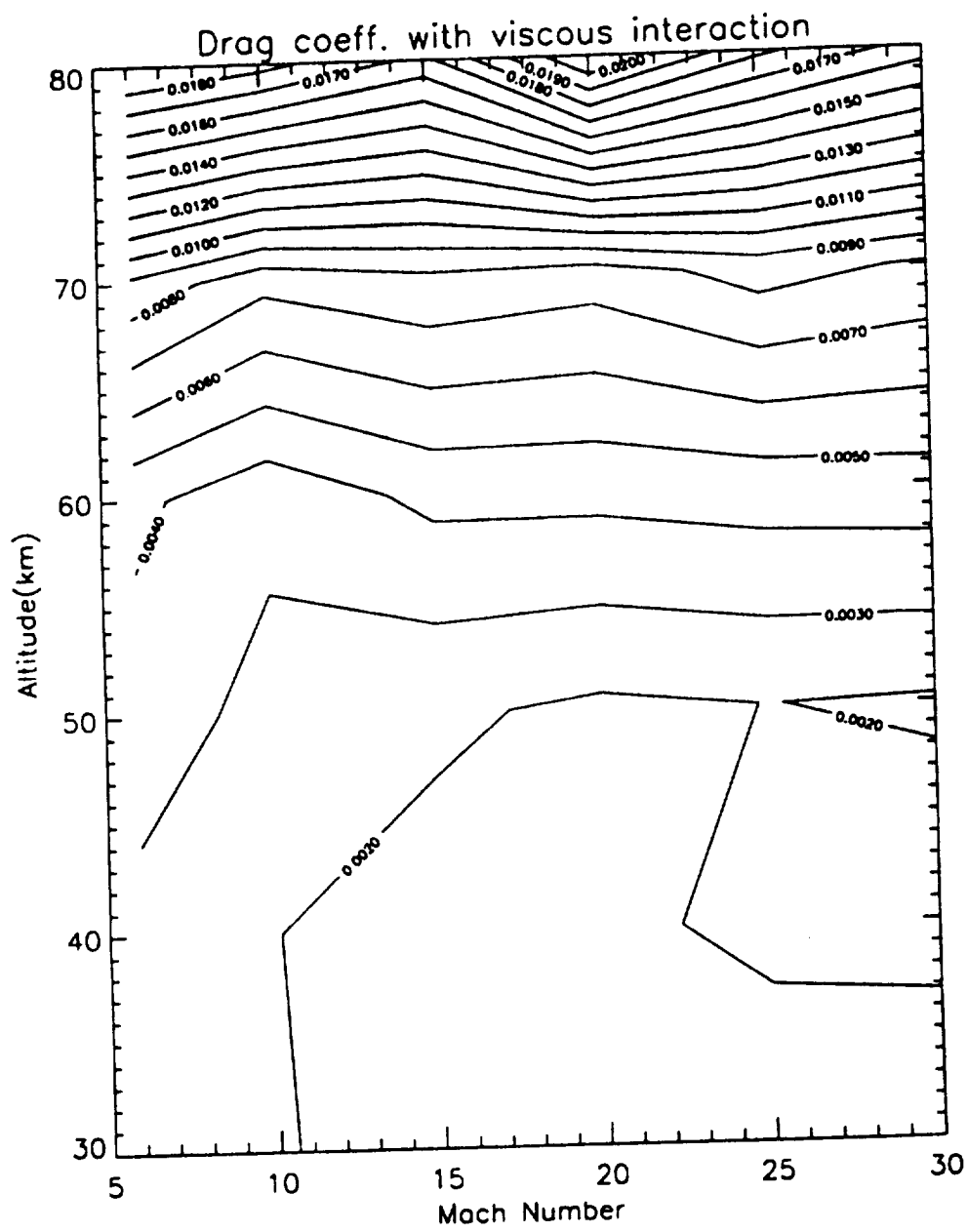
Figure C.72: Drag coefficient contour with viscous interaction
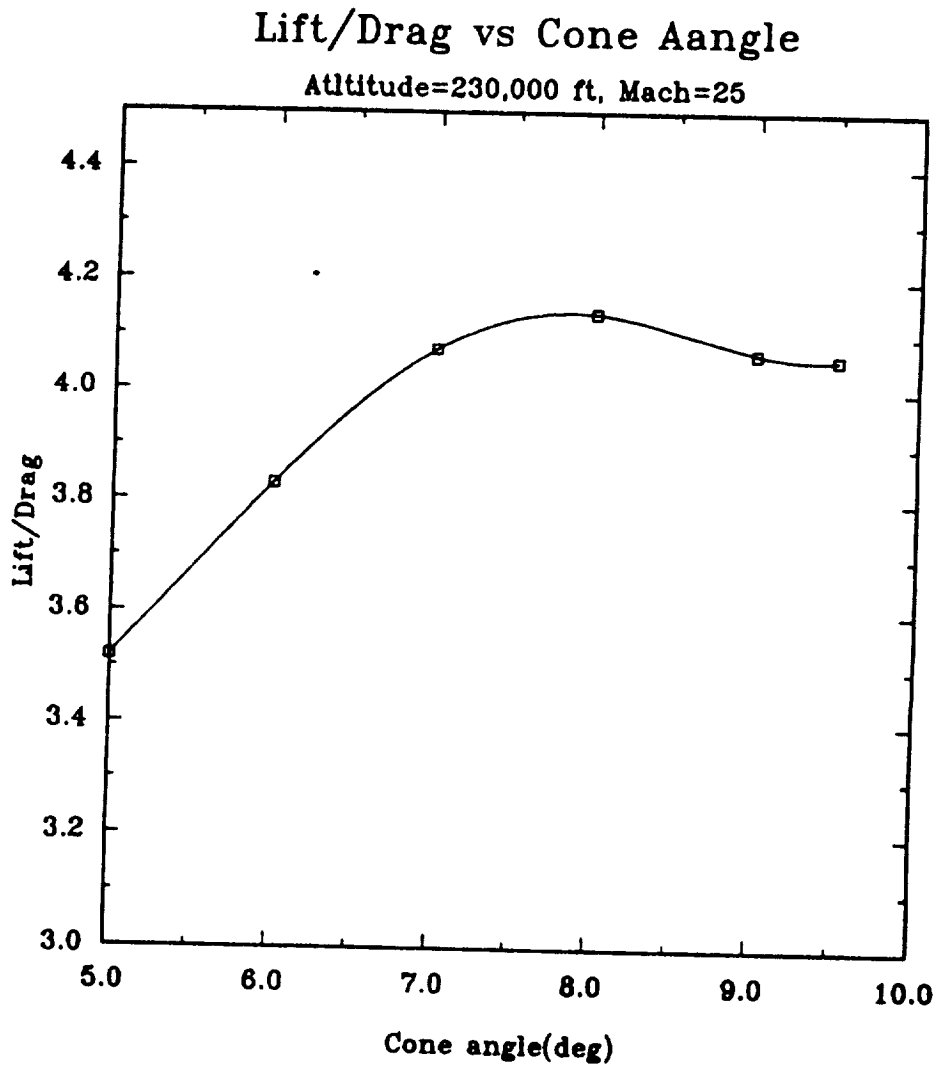
Figure C.73: L/D versus cone angle for best optimum waverider

Displacement Thickness Distrbution

M=25 Alt=230,000 ft Streamline #1
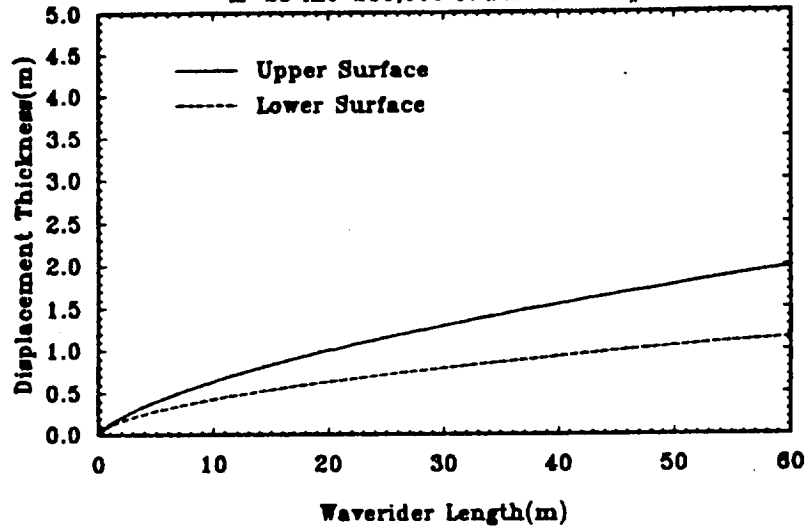
(a)
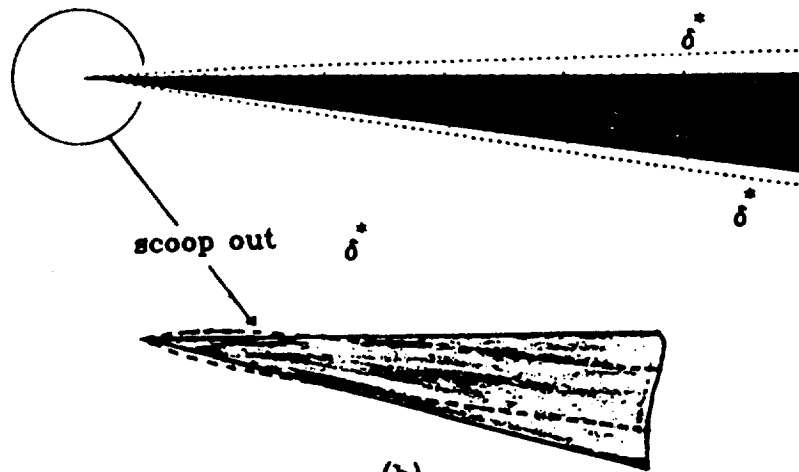
(b)

Figure C.74: Displacement thickness of waverider

Planform view   Side view   Front view
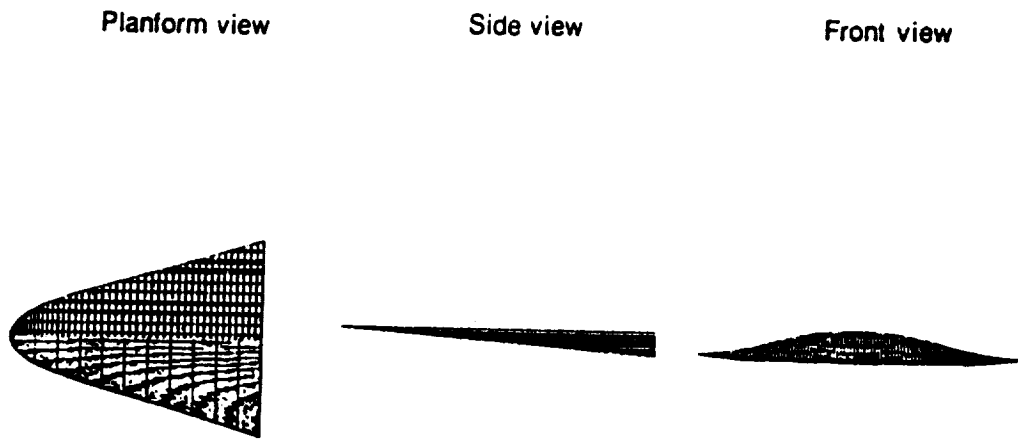
Viscous Interaction Optimum Waverider

Mach=14.0, Altitude=140,000 Ft

Cone angle(deg)=5.7 Length=60m
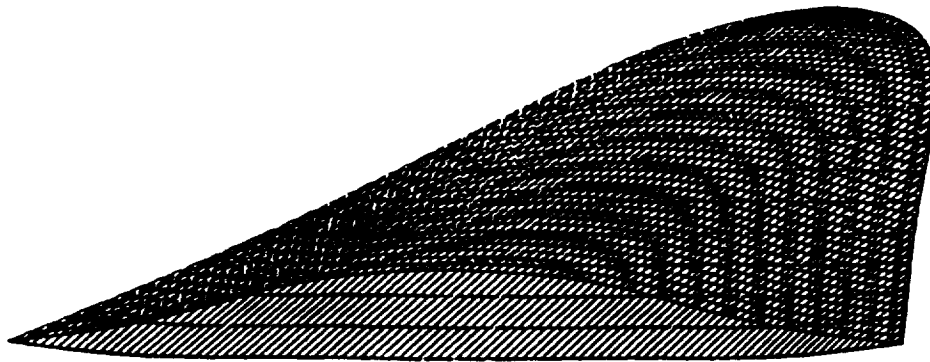
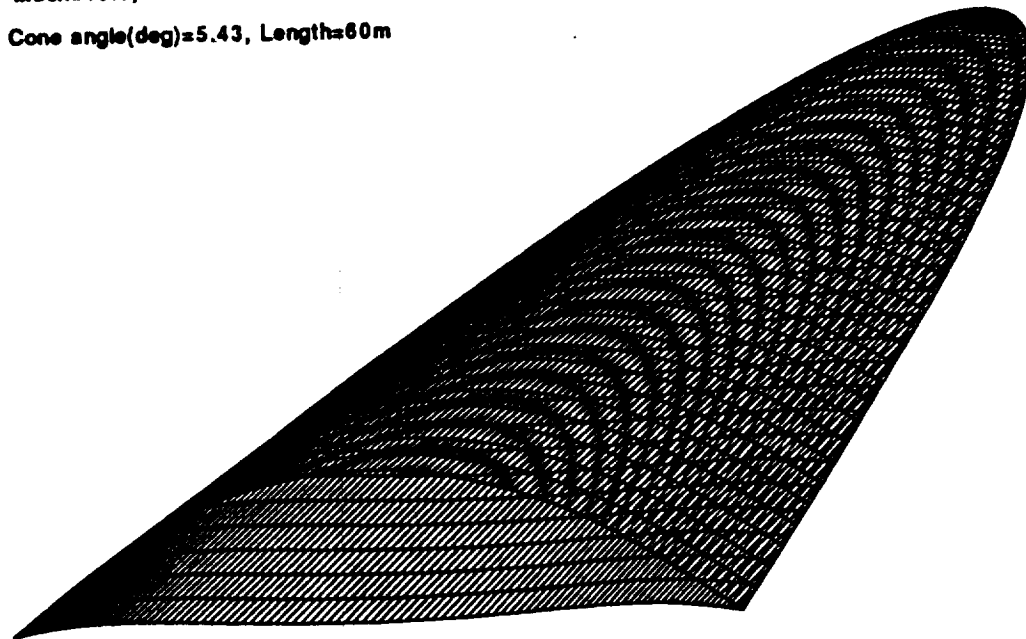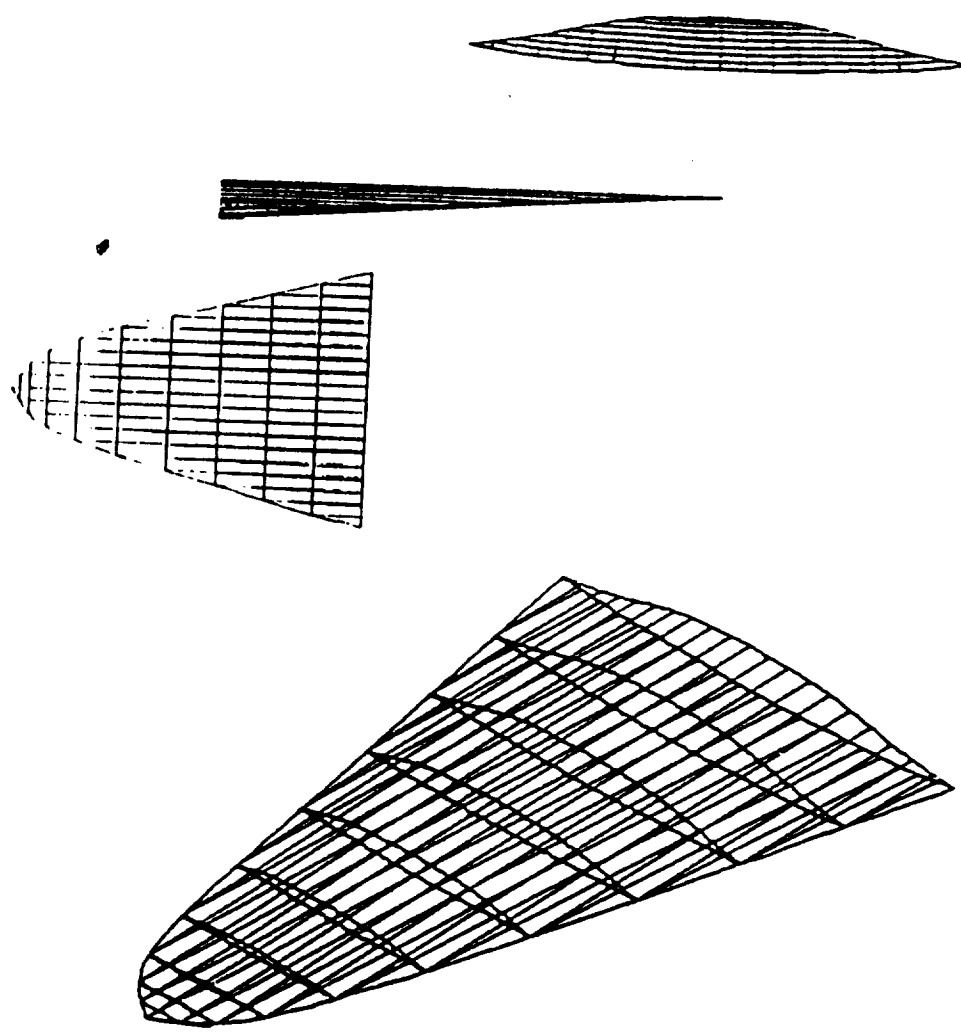Figure C.75: Viscous interaction optimum waverider H=140,000ft M=14
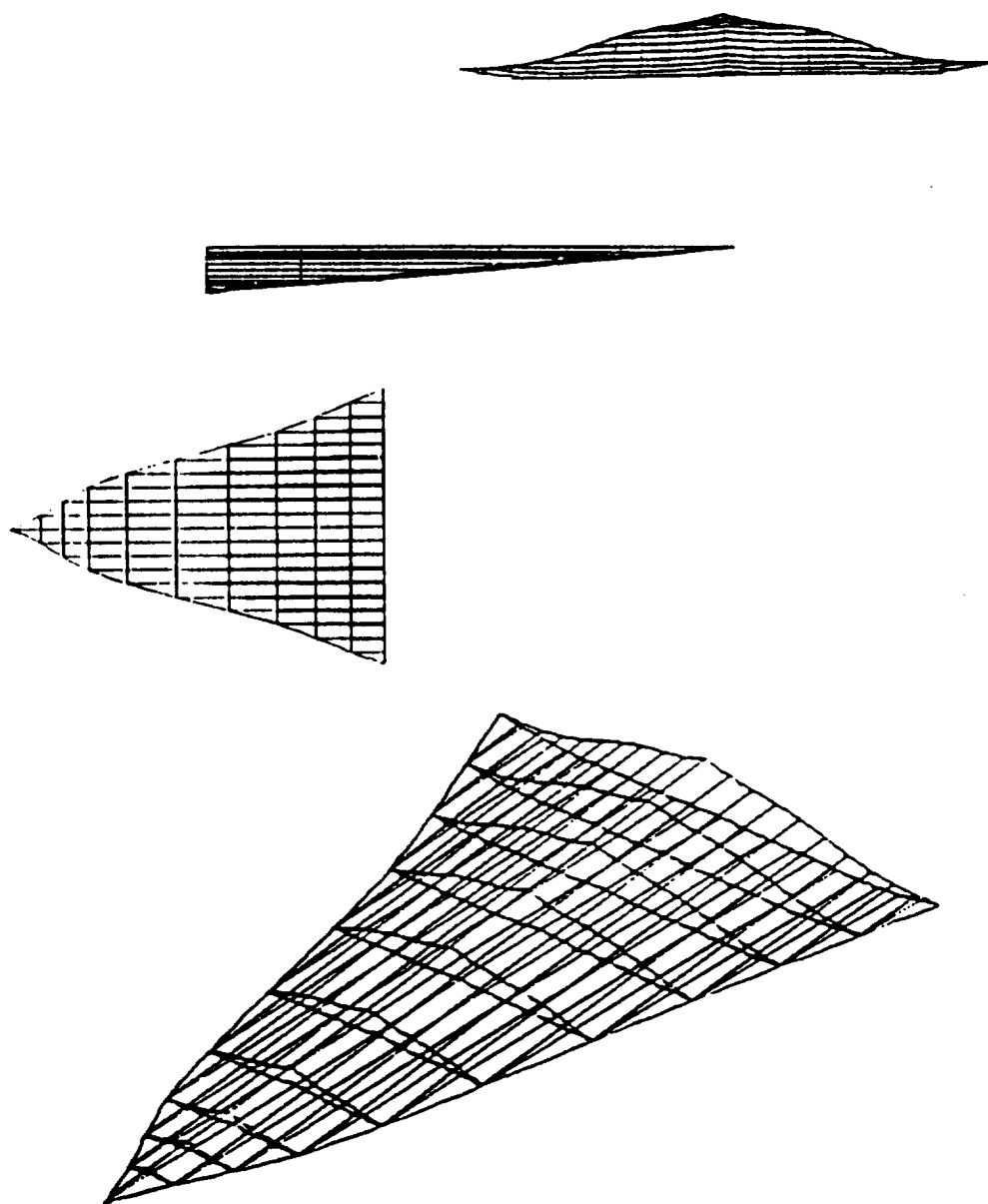
Figure C.76: Without Viscous interaction waverider H=140,000ft M=14

Planform view   Side view   Front view

Non-Optimized Viscous Interaction Waverider

Mach=14.0, Altitude=140,000 Ft
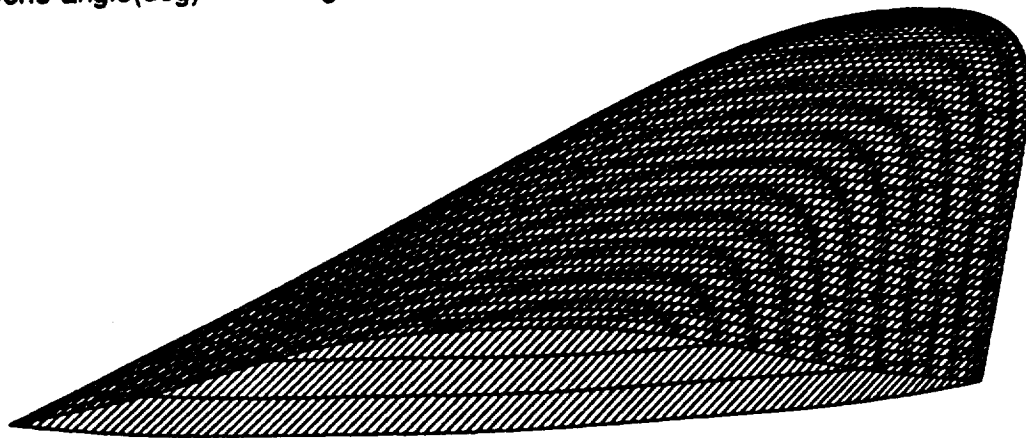
Cone angle(deg)=6.0, Length=60m
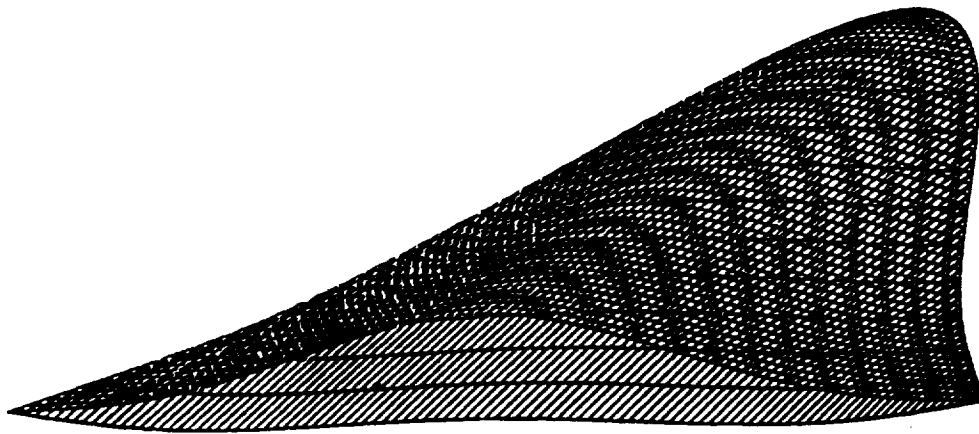
Figure C.77: Nonoptimized viscous interaction waverider H=140,000ft M=14

Chibar Distribution on Waverider

Alt=140,000 Ft, Mach=14 Stream line # 1
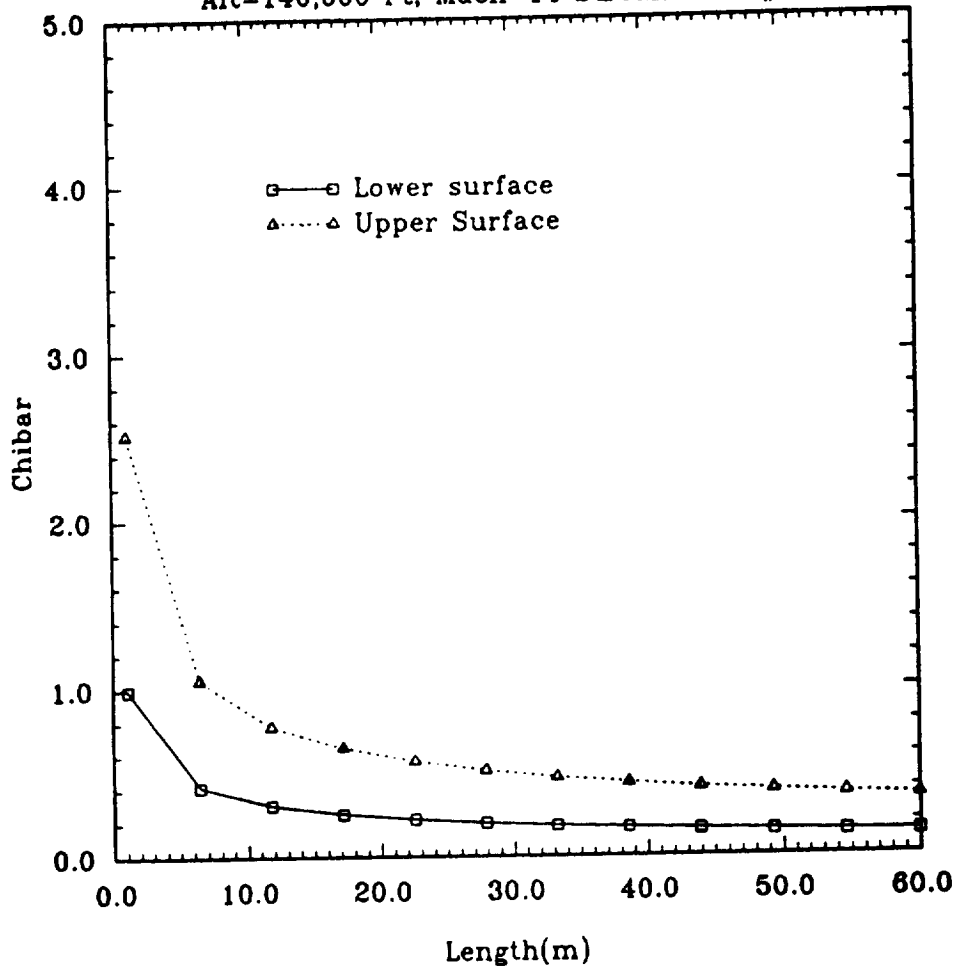
Figure C.78: $\overline{\chi}$ distribution on waverider H=140,000ft M=14
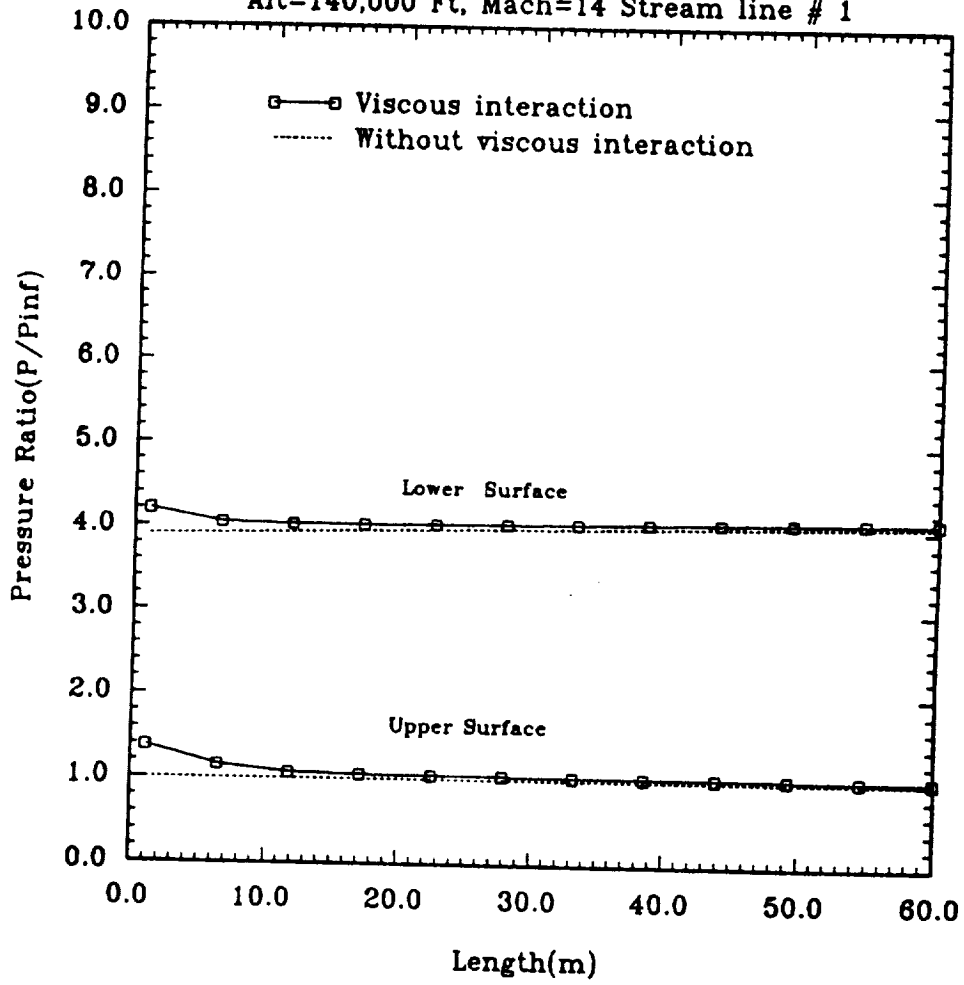
Figure C.79: Pressure ratio distribution on waverider H=140,000ft M=14

Planform view **Side view** **Front view**

Viscous Interaction Optimum Waverider

Mach=16.0, Altitude=140,000 Ft

Cone angle(deg)=5.43, Length=60m

Figure C.80: Viscous interaction optimum waverider H=140,000ft M=16

Figure C.81: Without Viscous interaction waverider H=140,000ft M=16

Planform view **Side view** **Front view**

No Optimized Viscous Interaction Waverider

Mach=16, Altitude=140,000 Ft
Cone angle(deg)=5.5 Length=60m

Figure C.82: Nonoptimized viscous interaction waverider H=140,000ft M=16

Chibar Distribution on Waverider
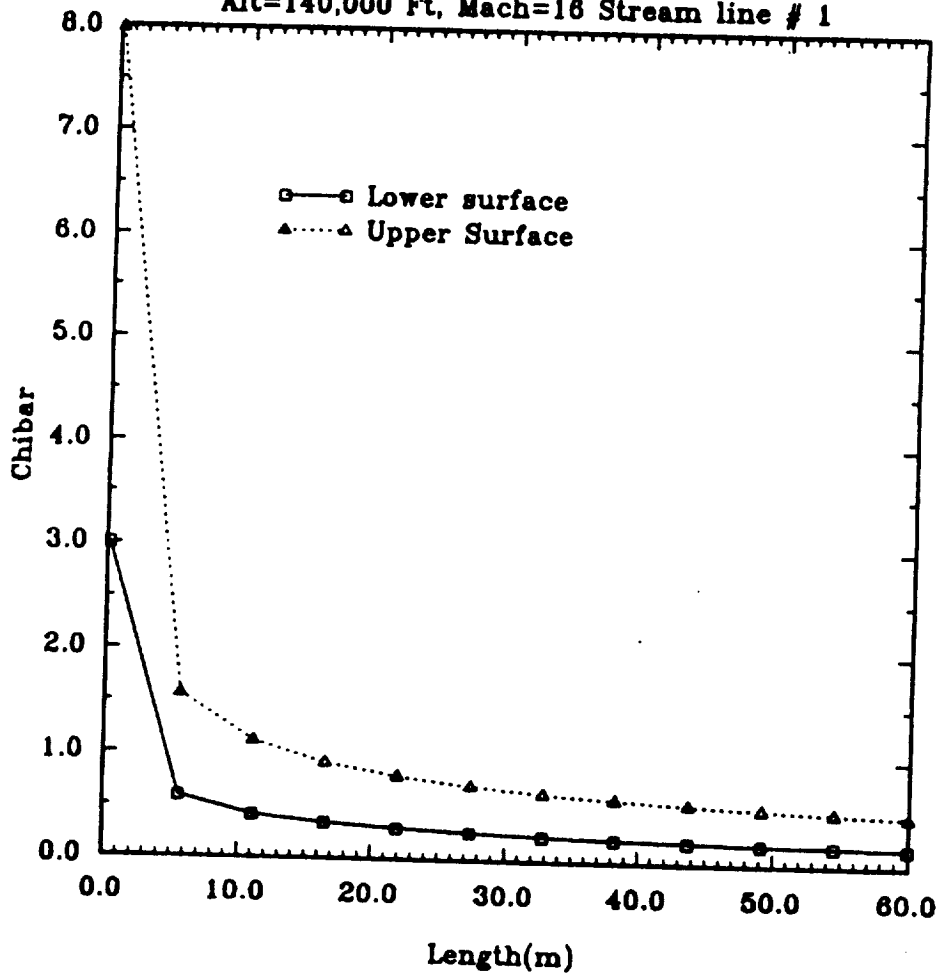
Alt=140,000 Ft, Mach=16 Stream line # 1

Figure C.83: $\overline{\chi}$ distribution on waverider H=140,000ft M=16

Pressure Distribution on Waverider

Alt=140,000 Ft, Mach=16 Stream line # 1

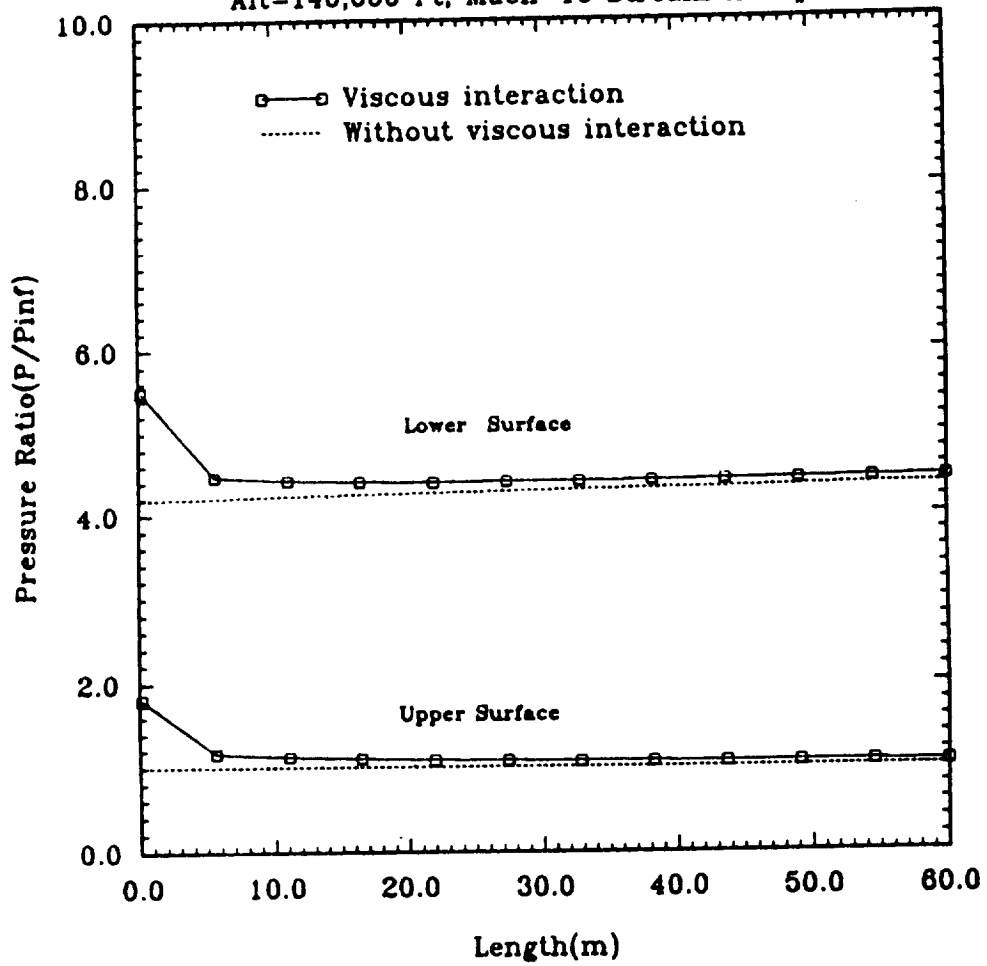
Figure C.84: Pressure ratio distribution on waverider H=140,000ft M=16

Planform view   Side view   Front view

Optimum Viscous Interaction Waverider

Mach=20.0, Altitude=175,000 Ft
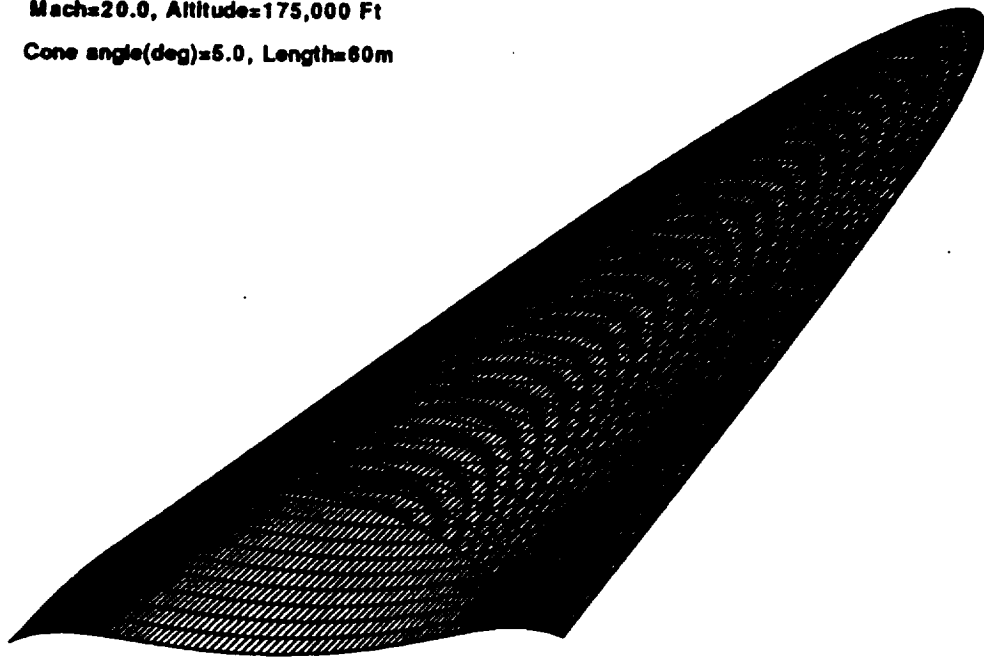
Cone angle(deg)=5.0, Length=60m

Figure C.85: Viscous interaction optimum waverider H=175,000ft M=20
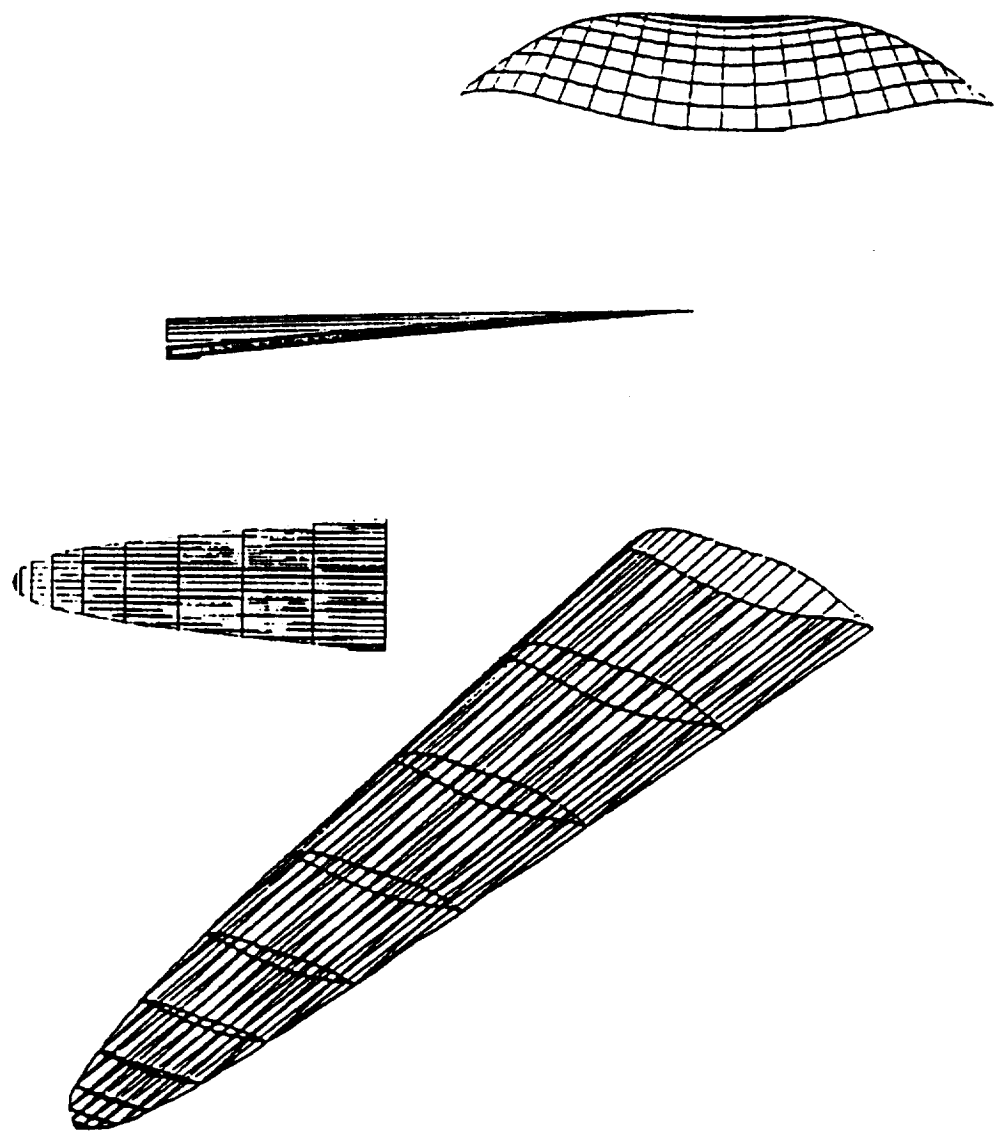
Figure C.86: Without viscous interaction waverider H=175,000ft M=20

Planform view   Side view

Front view

Non-Optimized Viscous Interaction Waverider

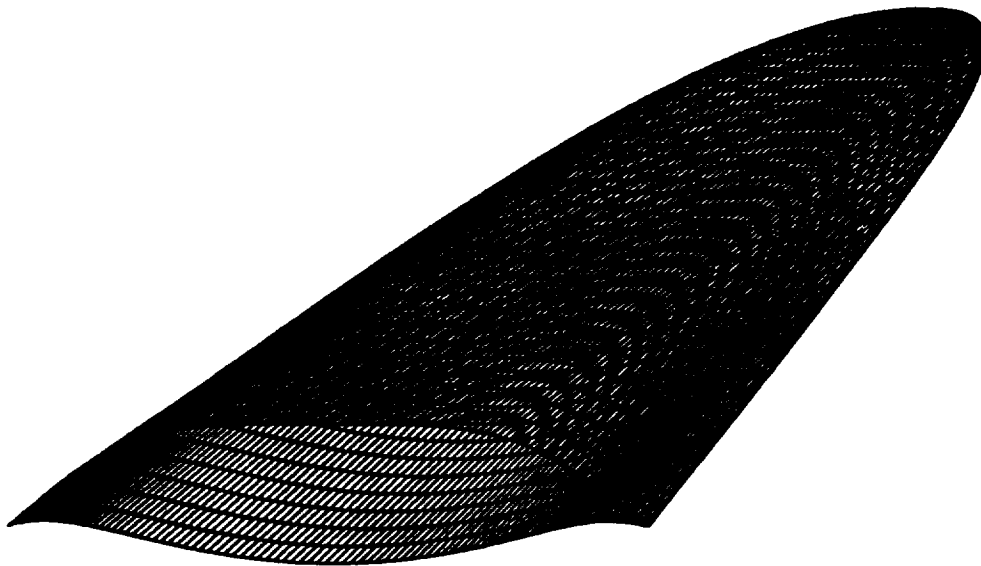**Mach=20.0, Altitude=175,000 Ft**

Cone angle(deg)=5. Length=60m

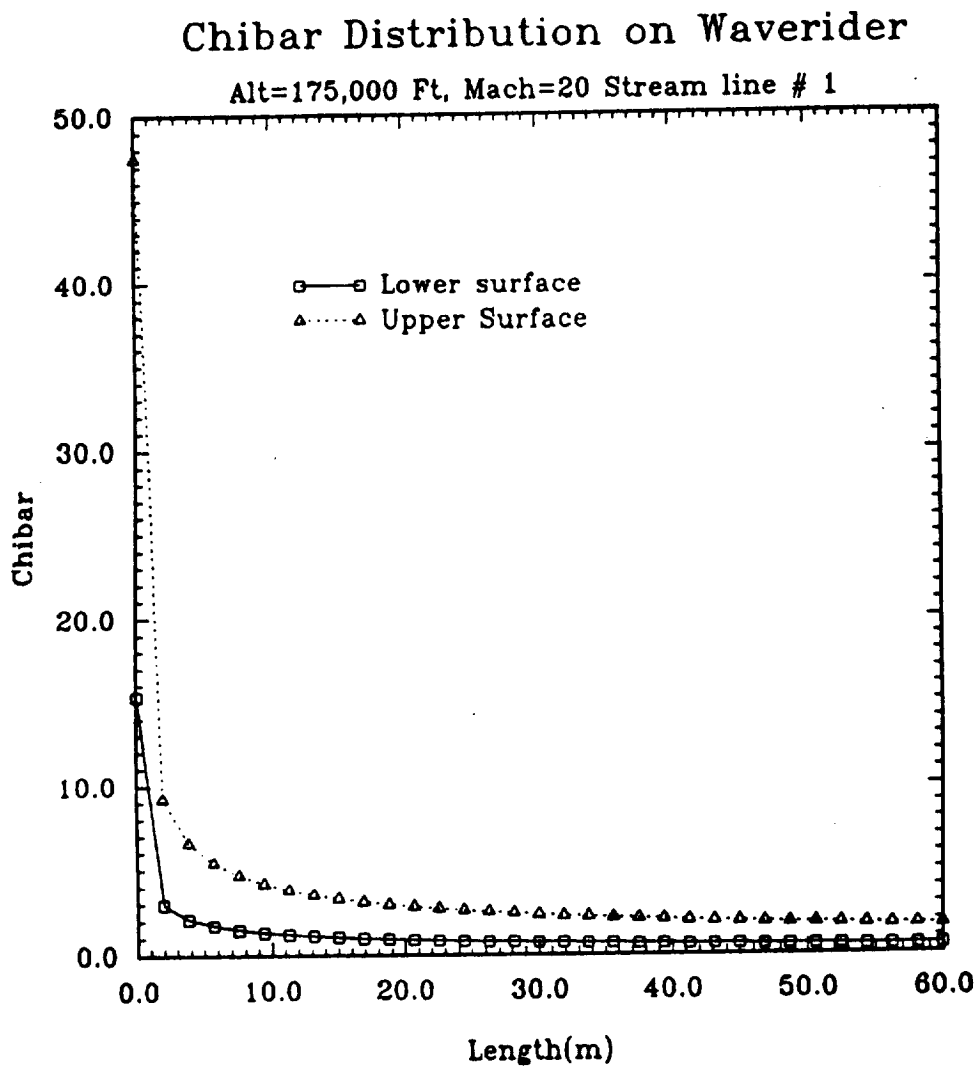Figure C.87: Nonoptimized viscous interaction waverider H=175,000ft M=20

Figure C.88: $\bar{\chi}$ distribution on waverider H=175,000ft M=20

Pressure Distribution on Waverider
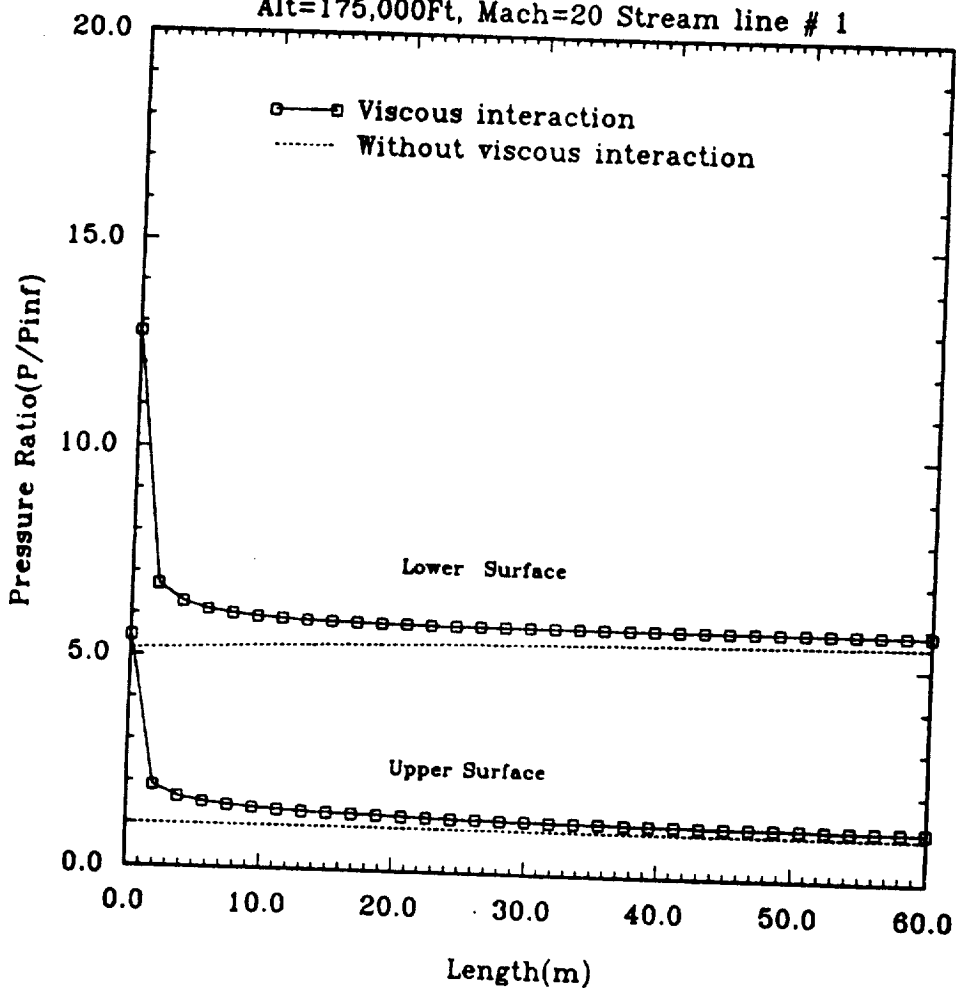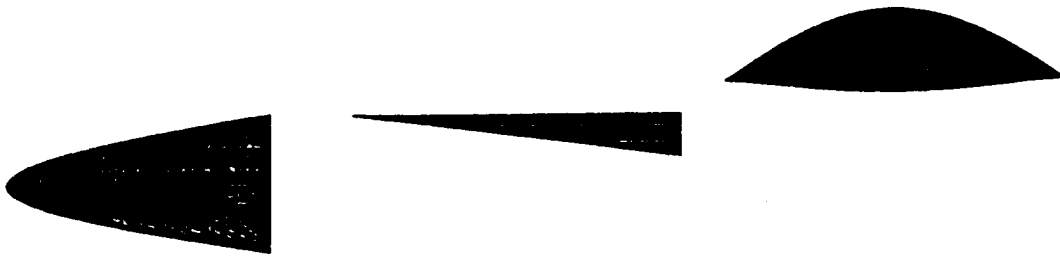
Alt=175,000Ft, Mach=20 Stream line # 1

o—o Viscous interaction
.... Without viscous interaction

Lower Surface

Upper Surface

Pressure Ratio(P/Pinf)

Length(m)

Figure C.89: Pressure ratio distribution on waverider H=175,000ft M=20

184

Planform view   Side view   Front view

Viscous Interaction Optimum Waverider

Mach=25.0, Altitude=230,000 Ft

Cone angle(deg)=8.0 Length=60m
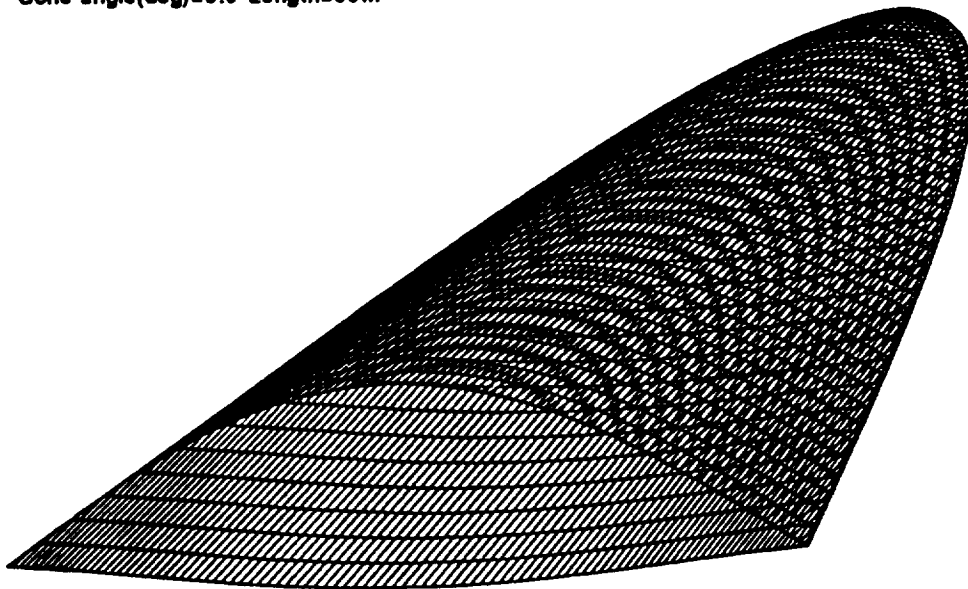
Figure C.90: Viscous interaction optimum waverider H=230,000ft M=25
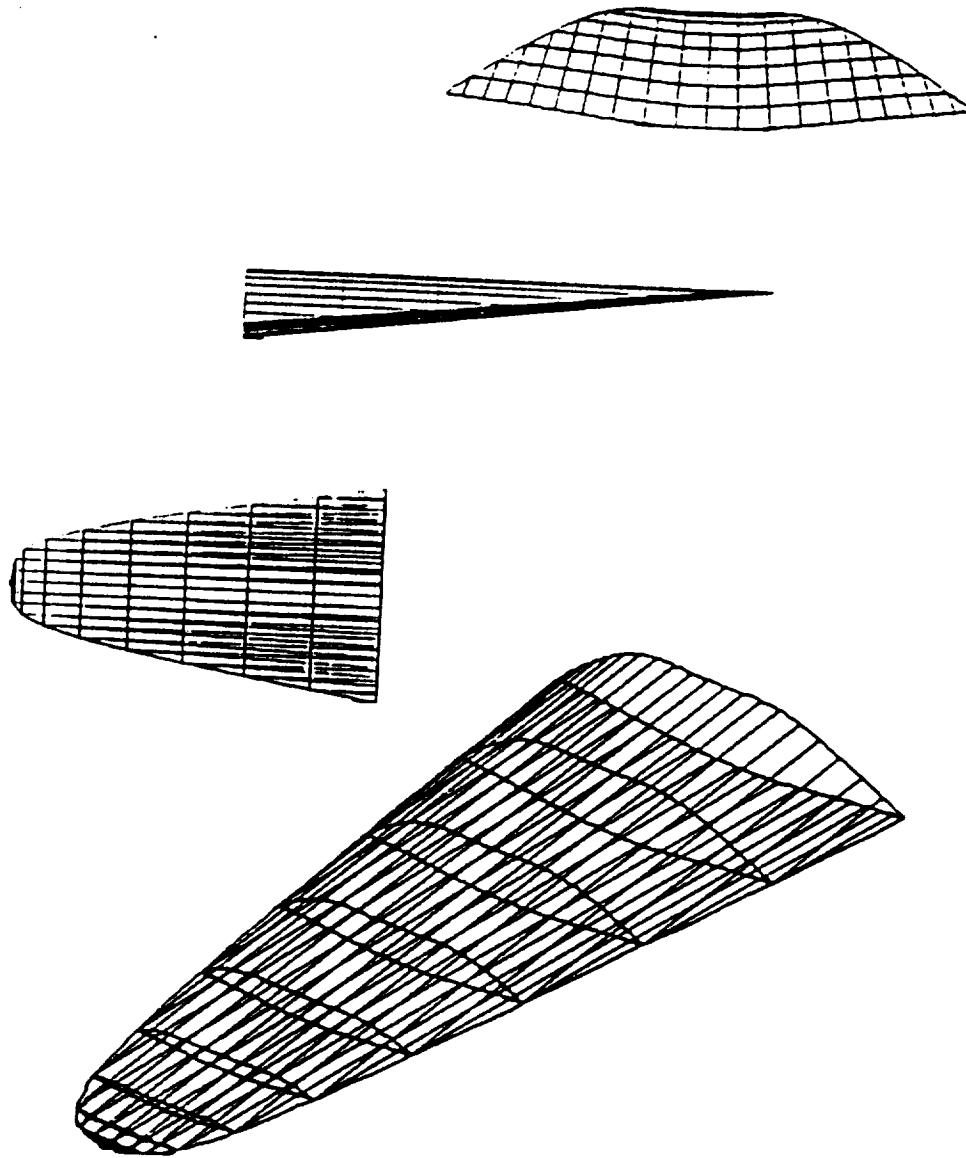
Figure C.91: Without Viscous interaction waverider H=230,000ft M=25

Planform view   Side view   Front view
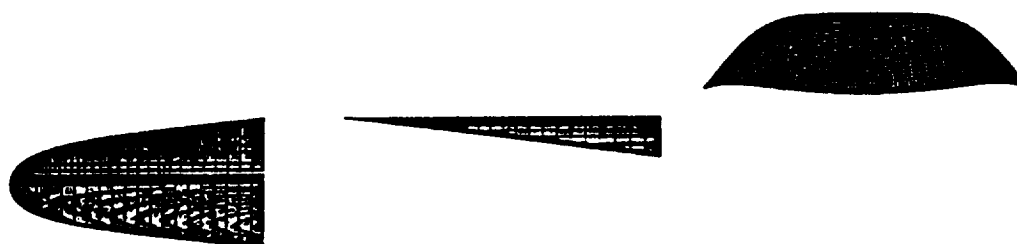
Non-Optimized Viscous Interaction Waverider

Mach=25.0, Altitude=230,000Ft

Cone angle(deg)=8.0, Length=60m

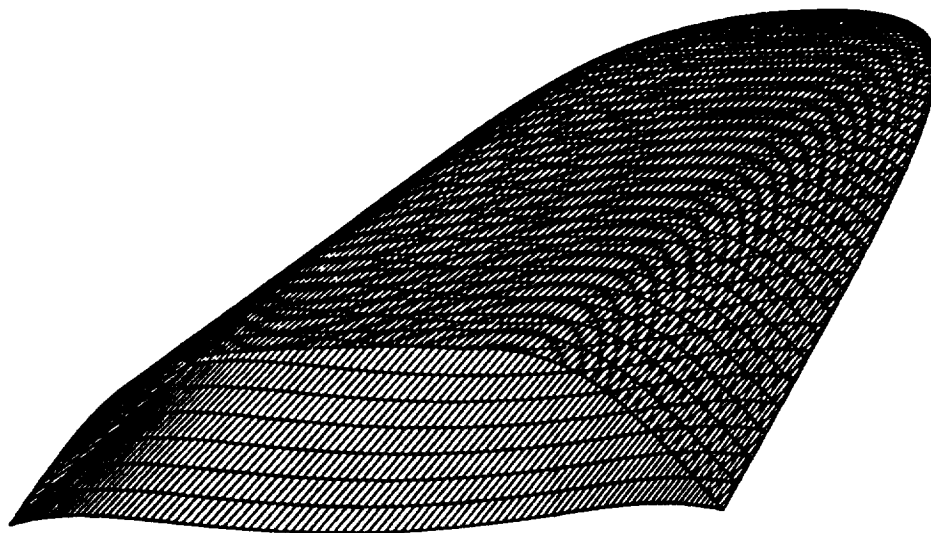Figure C.92: Nonoptimized viscous interaction waverider H=230,000ft M=25
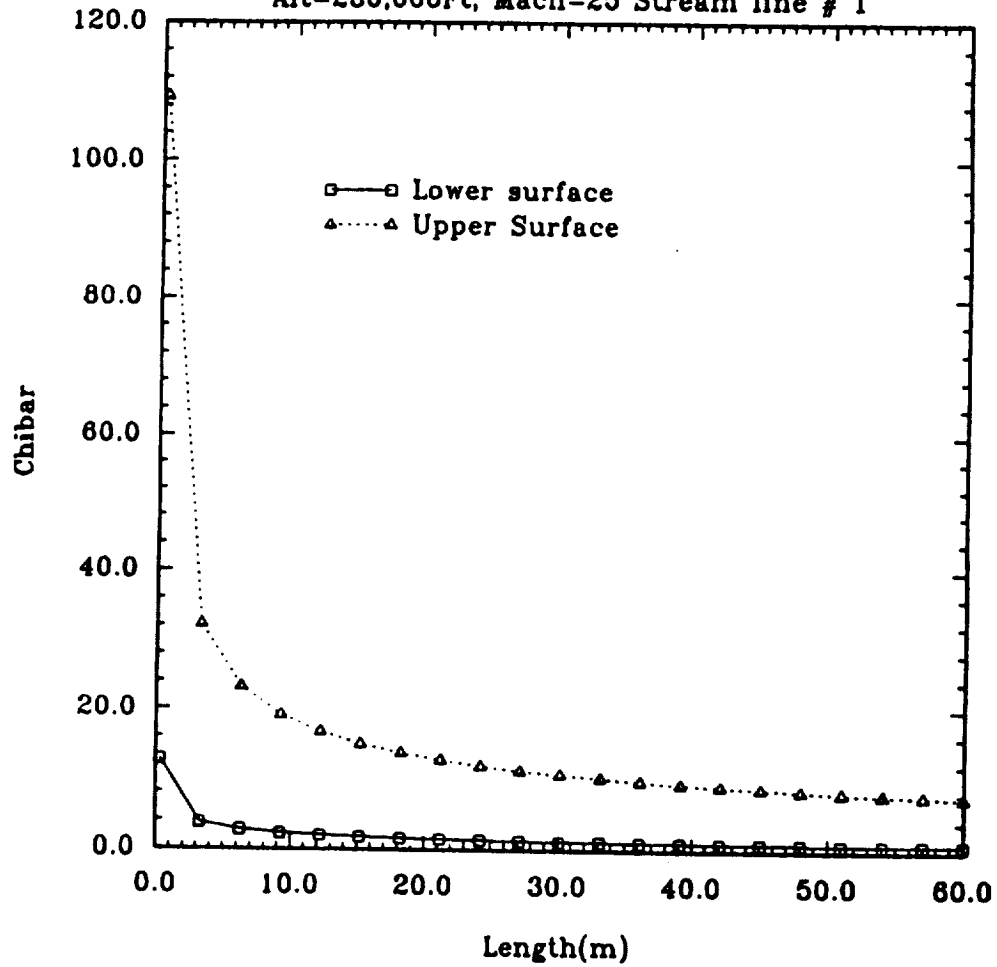
Figure C.93: $\overline{\chi}$ distribution on waverider H=230,000ft M=25
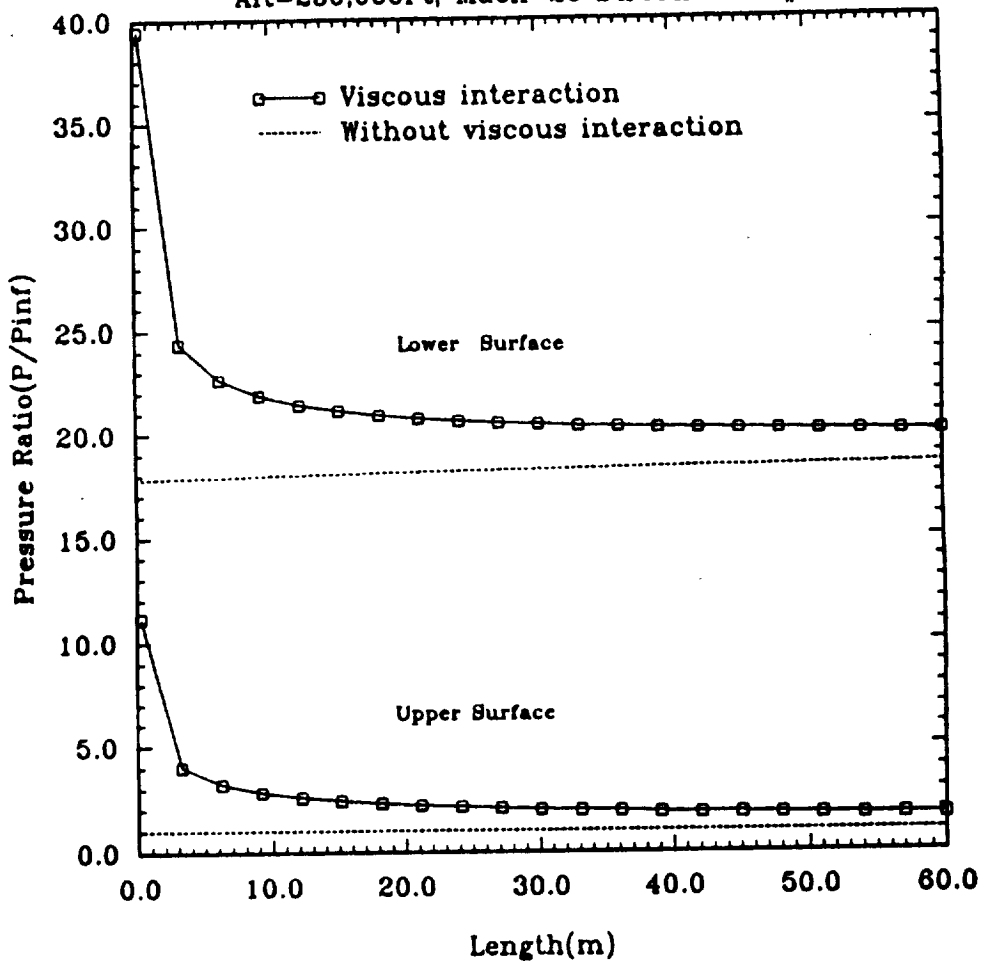
Figure C.94: Pressure ratio distribution on waverider H=230,000ft M=25

Bibliography

[1] Long, N. Lyle.,"The Off -Design Performace of Hypersonic Waveriders," AGARD Lecture Bristol, England, April 1987.

[2] Stollery, J.L., "Viscous Interaction Effect on Re-Entry Aerothermodynamics: Theory and Experimental Results," in Aerodynamic Problems of Hypersonic Vehicles, (ed. by Enkenhus, K., Wendt, J.F., and Pankurst, R.C.) AGARD Lecture Series No. 42, Vol I, July 1972, pp. 10-1 through 10-28.

[3] Cox, R.N. and Crabtree, L.F., "Elements of Hypersonic Aerodynamics," Academic Press, New York, 1965.

[4] Anderson, J. D., Jr., *Hypersonic and High Temperature Gas Dynamics*, McGraw-Hill Book Co., New York, 1989.

[5] Hayes, W.D., and Probstein, R.F., *Hypersonic Flow Theory*, Academic Press, New York, 1959.

[6] Talbot, L., Koga, T., and Sherman, P.M.,"Hypersonic Viscous Flow Over Slender Cones," NACA TN 4327, Sept. 1958.

[7] Lees, L., "Influence of the Leading-Edge Shock Wave on the Laminar Boundary Layer at Hypersonic Speeds," *Journal of the Aeronautical Science*, Vol. 21, No. 6, June 1956, PP. 594-600, 612.

[8] Becker, J. V.,"Results in Recent Hypersonic and Unsteady Flow Research at the Langley Aeronautical Library, *Journal of Applied Physics*, Vol. 21, no. 7, July 1950., pp. 622-624.

[9] Truitt, R. W.,*Hypersonic Aerodynamics*, The Ronald Press Company, 1959.

[10] Bertram, M. H., "Boundary Layer Displacement Effects in Air at Mach Numbers 6.8and 9.6," NACA TN 4133, Feb. 1958.

[11] Anderson, J.D. Jr., *Modern Compressible Flow with Historical Perspective*, 2nd ed., McGraw-Hill Book Co., New York, 1990.

[12] Stewartson, K., "On the Motion of a Flat Plate at High Speed in a Viscous Compressible Fluid - II, Steady Motion," *Journal of the Aeronautical Sciences*, Vol. 22, No. 5, May 1955, pp. 303-309.

[13] Nonweiler, T.R.F.,"Aerodynamic Problems of Manned Space Vehicles," *Journal of the Royal Aeronautical Society*, Vol. 63, 1959, pp. 521-528.

[14] Townend, L. H.,"Research and Design for Lifting Reentry," *Progress in Aerospace Science*, Vol. 18, 1979, pp. 1-80.

[15] Roe, P. L., "Theory of Waveriders," in Aerodynamic Problems of Hypersonic Vehicles, edited by K. Enkenhus, J. F. Wendt, and R. C. Pankhurst, AGARD LS-42, 1972.

[16] Townend, L. H., "On Lifting Bodies which Contain Two-Dimensional Supersonic Flows," Aeronautical Research Council R. & M. No. 3383, 1964.

[17] Becker, J. V.,"Studies of High Lift/Drag Ratio Hypersonic Configurations," the 4th Congress of the International Council of the Aeronautical Sciences, August 24-28, 1964.

[18] Nonweiler, T.,"Delta Wings of Shapes Amenable to Exact Shock-Waves Theory," *Journal of the Royal Aeronautical Society*, Vol. 67, January 1963, pp. 39-40.

[19] Flower, J. W., "Configurations for High Supersonic Speeds Derived from Simple Shock-Waves and Expansions," *Journal of the Royal Aeronautical Society*, Vol. 67. May 1963, pp. 287-290.

[20] Woods, B. A., "Hypersonic Flow with Attached Shock Waves over Delta Wings," *The Aeronautical Quarterly*, Royal Aeronautical Society, Vol. XXI, November 1970, pp. 379-399.

[21] Jones, J. G., "A Method for Designing Lifting Configurations for High Supersonic Speeds Using the Flow Fields of Non-Lifting Cones," Royal Aircraft Establishment, Report No. Aero. 2674, March 1963.

[22] Cole, J. D. and Zien, T. F., "A Class of Three-Dimensional, Optimum Hypersonic Wings," AIAA Journal, Vol. 7. No. 2, Feb. 1969, pp. 264-271.

[23] Pike, J., "Experimental Results From Three Cone-flow Waveriders," Hypersonic Boundary Layers and Flow Fields, AGARD CP No. 30, May 1968, pp. 12-1 to 12-11.

[24] Rasmusen, M. L., "Lifting-Body Configurations Derived from Supersonic Flows Past Inclined Circular and Elliptic Cones," American Institute of Aeronautics and Astronautics, AIAA-79-1665, August 6-8, 1979.

[25] Rasmussen, M. L., "Waverider Configurations Derived from Inclined Circular and Elliptic Cones," *Journal of Spacecraft and Rockets*, Vol. 17, No. 6, Nov.-Dec. 1980, pp. 537-545.

[26] Kim, B. S., Rasmussen, M.L., and Jischke, M.C., "Optimization of swaverider Configurations Generated from Axisymmetric Conical Flows," AIAA-82-1299, 1982.

[27] Kim, B. S., "Optimization of Waverider Configurations Generated from Non-Axisymmetric Flows Past a Nearly Circular Cone," Ph. D. Dissertation, School of Aerospace, mechanical, and Nuclear Engineering, University of Oklahoma, 1983.

[28] Bowcutt, Kevin G., "Optimization of Hypersonic Waveriders Derived from Cone Flows-Including Viscous Effects," Ph.D. Dissertation, Department

of Aerospace Engineering, University of Maryland, College Park, Maryland,1986.

[29] Bowcutt, K. F.,Anderson,J. D.,Jr. and Capriotti, D. P.,"Viscous Optimized Hypersonic Waveriders," AIAA Paper 87-0272,the AIAA 25th Aerospace Sciences Meeting, January 12-15, 1987.

[30] Corda, S.,"Viscous Optimized Hypersonic Waveriders Designed from Flows Over Cones and Minimum Drag Bodies," Ph.D. Dissertation, Department of Aerospace Engineering, University of Maryland, 1988.

[31] McLaughlin, T. A.,"Viscous Optimized Hypersonic Waveriders for Chemical Equilibrium Flow," Master of Science Thesis, Department of Aerospace Engineering, University of Maryland, College Park, Maryland, 1990.

[32] Sobieczky,H.,Dougherty, F. C.and Jones, K.,"Hypersonic Waverider Design from Given Shock Waves," First International Hypersonic Waverider Symposium, Oct. 17-19, 1990.

[33] Jones, K. D., Bauer, S. X. and Doughert, F. C., "Hypersonic Waverider Analysis: A Comparison of Numerical and Experimental Results," AIAA Paper 91-1696, the AIAA 22nd Fluid Dynamics & Lasers Conference, June 24-26, 1991.

[34] McCroskey, W. T., Bogdowff, S. M., and McDougall, J. G.," An Experimental Model for the Sharp Flat Plate in Rarefied Hypersonic Flow," AIAA Journal, Vol. 4, no. 9, Sept. 1966, pp. 1580-7.

[35] Schlichting, H., *Boundary Layer Theory*, McGraw-Hill Book Co., New York, 1987.

[36] Li, T. Y. and Nagamatsu, H. T., "Shock Wave Effects on the Laminar Skin Friction of an Insulated Flat Plate at Hypersonic Speeds," Journal of the Aeronautical Sciences, Vol. 20, no. 5, May 1953, pp. 345-355.

[37] White, F. M., *Viscous Fluid Flow*, McGraw-Hill Book Co., New York, 1974.

[38] Dorrance, W. H., *Viscous Hypersonic Flows*, McGraw-Hill Book Co., New York, 1962.

[39] Lees, Lester, and Probstein, R. F., "Hypersonic Viscous Flow Over a Flat Plate," Rep. no 195 Contract AF 33(0981 - 250), Aeronaut. ENG. Lab. Princeton Univ. April 1952.

[40] Chapman, D. R., and Rubesin, M. W., "Temperature and Velosity Profiles in the Compressible Laminar Boundary Layer with Arbitrary Distribution of Surface Temperature," *Journal of the Aeronautical Science*, Vol. 16., no 9, pp. 547-565, Sept. 1949.

[41] Bertram, M. H. and Blackstock, T. A., "Some Simple Solutions to the Problem of Predicting Boundary-Layer Self-Induced Pressure," Technical Report TN D-798, *NASA*, 1961.

[42] White, F. M., "Hypersonic Laminar Viscous Interactions on Inclined Flat Plates," *ARS Journal*, 32:780-781, 1962.

[43] Lewis, M. J., "The Prediction of Inlet Flow Stratification and Its Influence on the Performance of Air-Breathing Hypersonic Propulsion Systems," Ph. D. Dissertation, M.I.T., June 1988.

[44] Shapiro, A. H., "Dynamics and Thermodynamics of Compressible Fluid Flow," Vol. 2, Ronald Press, New York, 1954. Art. 19.3.

[45] Burden, R. L., Faires, J. D., and Alvert, A. C., "Numerical Analysis," Prindle, Weber, and Schmidt, Boston, 1981.

[46] Nelder, J. A., Mead, R., "A Simplex Method for Function Minimization," *Computer Journal*, Vol. 7, Jan. 1965, pp. 308-313.

[47] Van Wie, D. M., "An Application of Computational Fluid Dynamics to the Design of Optimum Ramjet and Powered Missile Components," Ph. D. Dissertation, Dept. of Aerospace Engineering, University of Maryland, College Park, May 1985.

[48] Wiliams, R. M., "National Aero–Space Plane: Technology for America's Future," *Aerospace America*, November 1986, pp. 18-22.

[49] Bussing, T. and Eberhardt, S., "Chemistry Associated with Hypersonic Vehicles," AIAA Paper No. 87-1292.

REPORT DOCUMENTATION PAGE

Form Approved
OMB No. 0704-0188

1. AGENCY USE ONLY *(Leave blank)*	2. REPORT DATE March 1992	3. REPORT TYPE AND DATES COVERED Contractor Report

4. TITLE AND SUBTITLE

A Study of Viscous Interaction Effects on Hypersonic Waveriders

6. AUTHOR(S)

Jinhwa Chang

5. FUNDING NUMBERS

G NAG1-1192

WU 505-59-40-10

7. PERFORMING ORGANIZATION NAME(S) AND ADDRESS(ES)

University of Maryland
Department of Aerospace Engineering
College Park, MD 20742

8. PERFORMING ORGANIZATION REPORT NUMBER

UM-AERO 91-44

9. SPONSORING/MONITORING AGENCY NAME(S) AND ADDRESS(ES)

National Aeronautics and Space Administration
Langley Research Center
Hampton, VA 23665-5225

10. SPONSORING/MONITORING AGENCY REPORT NUMBER

NASA CR-189587

11. SUPPLEMENTARY NOTES The information presented in this report was offered as a thesis in partial fulfillment of the requirements for the Degree of Doctor of Philosophy, University of Maryland, College Park, Maryland, December 1991.
Langley Technical Monitor: Lawrence D. Huebner

12a. DISTRIBUTION/AVAILABILITY STATEMENT

Unclassified - Unlimited

Subject Category 02

12b. DISTRIBUTION CODE

13. ABSTRACT *(Maximum 200 words)*

The effects of viscous interaction in the analysis and design of improved classes of viscous optimized hypersonic waveriders is examined. The Corda computer program is used to generate viscous optimized hypersonic waveriders from conical flow fields without viscous interaction. Each waverider is optimized for maximum L/D, and comparison studies are made between cases with and without viscous interaction. The results show that aerodynamic performance of the viscous interaction waveriders are reduced due mainly to a large increase in skin-friction drag associated with the viscous interaction phenomena that grows with increasing Mach number and altitude, but some of this performance loss can be recouped by including viscous interactions within the optimization procedure. When the waverider is optimized for viscous interaction, the shape can change dramatically. A significant result of the present work delineates on a velocity-altitude map the region where viscous interaction effects are significant for modern hypersonic waveriders by performing parametric runs to produce L/D, C_L, and C_D contour plots for Mach numbers from 6 to 30 at altitudes from 30 to 80km.

14. SUBJECT TERMS

hypersonic waveriders
analysis and design
viscous interaction
optimization
aerodynamic performance

15. NUMBER OF PAGES
215

16. PRICE CODE
A10

17. SECURITY CLASSIFICATION OF REPORT Unclassified	18. SECURITY CLASSIFICATION OF THIS PAGE Unclassified	19. SECURITY CLASSIFICATION OF ABSTRACT	20. LIMITATION OF ABSTRACT